ISSN 0110 - 3326

Civil Engineering Research Report

Two-Dimensional Site Effects in Wellington and the Hutt Valley – Similarities to Kobe

B. Adams, R. Davis, J. Berrill, J. Taber

February 1999 99-3

Department of Civil Engineering
University of Canterbury
Christchurch, New Zealand

A Report to EQC on

TWO-DIMENSIONAL SITE EFFECTS IN WELLINGTON AND THE HUTT VALLEY – SIMILARITIES TO KOBE

Brian Adams
Rob Davis
John Berrill
Department of Civil Engineering
University of Canterbury

John Taber
Research School of Earth Sciences
Victoria University of Wellington

February 1999

ABSTRACT

Central Wellington and Lower Hutt City are both situated on soft alluvial basins bounded by stiff bedrock. The basins tend to trap seismic energy, creating an amplified and longer duration response. The potentially active Wellington Fault, which forms the western edge of the Hutt Valley and Wellington Harbour, represents a major seismic hazard to the area with a characteristic earthquake of magnitude 7.1-7.8 expected within the next few hundred years. Here we use a 2-D elastic finite-element method (FEM) to simulate the propagation of seismic SH waves through typical geological cross-sections of the Lower Hutt Valley and Te Aro Basin in Wellington. The results allow us to estimate the intensity and spatial distribution of ground motions during a major rupture of the Wellington Fault. Strong low-frequency shaking, characterised by surface wave propagation and 2-D modes of resonance, is expected over the entire width of both the Lower Hutt Valley and the Te Aro Basin. Amplification is both frequency- and position-dependant, with peak values of Fourier spectral ratio (FSR) reaching a value of 12 in Lower Hutt, and 19 in Wellington. Peak ground accelerations (PGA) vary between 0.8-1.3g in Lower Hutt, and 0.7-1.2g in Wellington. Vertical resonance of shallow soft layers near the sides may yield FSR up to 14, and PGA up to 0.7g. The aptly named basin-edge effect, speculated to be the cause of a belt of severe shaking during the 1995 Kobe earthquake, is observed in Lower Hutt simulations. It produces strong pulses of energy on the seismogram trace as vertically incident body waves construct with horizontally propagating edge waves. A maximum acceleration of 1.4g is predicted along a strip of land 70-200m away-from and parallel-to the Wellington Fault. Planners and Engineers need to be aware of the risk of extra-strong shaking associated with particular resonant frequencies and locations within Wellington and the Lower Hutt Valley.

CONTENTS

Chapter 1: INTRODUCTION

Wellington, the capital of New Zealand, lies adjacent to the potentially active Wellington fault and spreads across several sediment filled basins. The city is well known for its earthquake hazard, being located above a converging tectonic plate boundary. This report attempts to characterise the strong motion behaviour of both the Lower Hutt Valley and the Wellington (Te Aro) Basin with two-dimensional finite-element computer modelling techniques. It is intended to determine the distribution spatial of shaking intensity in both the time and frequency domains.

The Wellington fault represents a major seismic hazard to the Wellington region, with a characteristic earthquake of moment magnitude 7.6±0.3 expected within the next few hundred years (Van Dissen and Berryman, 1996). The rupture mechanism is predominantly right lateral strike slip, similar to that of the Hyogo-ken Nambu earthquake of 17 January 1995 that devastated Kobe and surrounding cities. Recent experience with large earthquakes such as Kobe 1995, Northridge 1995, Mexico 1985 and others has highlighted the importance of accounting for multi-dimensional effects when estimating strong ground motions within sedimentary basins.

We first review the current understanding on the seismic behaviour of sedimentary basins. Since the 1970's, researchers have been interested in determining the natural resonant frequencies and associated amplification of ground motions within soft basins by various numerical and analytical methods. Recently, the presence and importance of strong amplification near the sides of basins called edge effects has been recognised. The most notable recent example of a basin-edge effect was a belt of intense damage running parallel to the fault-bounded edge of the Osaka basin, Japan, during the Hyogo-ken Nambu earthquake. Similarities between Osaka Bay and the Lower Hutt Valley lead us to acknowledge the possibility of a similar occurrence during an event on the Wellington fault.

Computer modelling of the earthquake signal within a two-dimensional heterogeneous elastic half-space is achieved with the use of a finite element method (FEM) to

numerically simulate the propagation of seismic waves from their source to the ground surface. Two geological cross-sections through the Lower Hutt Valley and one through the smaller Te Aro Basin are constructed from existing geological data. Their geometry and material properties are used as input to create a finite element mesh of the section. The tool chain Archimedes (Bao et. al., 1996), developed at Carnegie Mellon University is used to simulate shaking in each cross-section.

Time-dependant displacement and acceleration data are captured at regular spacing across the surface of each cross-section. Seismogram plots show the propagation of surface waves across the valley as well as clear basin-edge type amplifications. Fourier spectral ratios (FSR) are computed to show two-dimensional resonance occurring within the valley. Realistic earthquake traces are computed from a seismogram recorded during the 1995 Hyogo-ken Nambu earthquake. Structural response spectra are also calculated at various positions to indicate likely levels of shaking within the two basins.

In this report, we present the results of our two-dimensional linear finite-element computer modelling as a substantial first step toward understanding site effects in the Lower Hutt Valley and Te Aro Basin during a major rupture on the Wellington fault. We also predict the possible occurrence of a Kobe-like basin-edge effect occurring in the Lower Hutt and Thorndon, adjacent to the Wellington fault.

Chapter 2: LITERATURE REVIEW

Over the last 25 years with the rapid advances in computing technology, numerical methods for modelling the seismic behaviour of underground geology have become increasingly more refined and easy to use. A result has been much modelling of two- and three-dimensional sedimentary basins in an effort to understand their seismic behaviour. Summaries are herein made of the many different computational modelling techniques available, prior research findings from modelled and observed sedimentary basin behaviour and seismic studies in the Wellington and Hutt Valley regions.

2.1 TECHNIQUES FOR MODELLING SEISMIC WAVE PROPAGATION

Solutions to the modelling of seismic waves in inhomogeneous material have generally been found through numerical techniques such as the finite-element method (e.g. Constantino et. al., 1967; Douglas, 1970; Drake, 1972a,b; Lysmer and Drake, 1972a,b; Smith, 1975) and finite-difference method (e.g. Boore, 1970, 1972; Helmberger and Vidale, 1988), that have the ability to analyse irregular, realistic geometries. Other common techniques include the ray-theory method (e.g. Jackson, 1971, Sanchez-Sesma et. al., 1988a), boundary-integral equation method (e.g. Dravinski and Mossissian, 1987), boundary-element method (e.g. Shibuya, 1992; Sanchez-Sesma and Luzon, 1995), discrete wavenumber method (e.g. Aki and Larner, 1970; Bouchon and Aki, 1977) discrete wavenumber boundary-element method (Kawase, 1988; Kawase and Aki, 1990; Bouchon, 1996), and other hybrid combinations thereof (e.g. Touhei and Yoshida, 1988; Zhang and Papageorgiou, 1995). Sanchez-Sesma (1987), Aki (1988), Helmberger and Vidale (1988) and Fah (1996) give good summaries of these techniques. Several other more obscure techniques include the Gaussian beam method, dynamic ray tracing, the Maslov method, the phase front method and the Kirchoff integral method (Kato et. al., 1993).

Exact analytical solutions for ground motions due to incident plane waves have been formulated for perfectly elastic and homogeneous two-dimensional soft valleys (eg.

Trifunac, 1971; Wong and Trifunac, 1974). Among the first to study seismic wave amplification within irregular soft basins were Aki and Larner (1970), who developed their part-numerical, part-analytical discrete wavenumber technique for the case of incident plane SH waves. Boore et. al. (1971) used both the Aki-Larner and finite-difference methods and incident SH waves to investigate the amplification effects of irregular underground geology.

Two-dimensional finite-element methods have been used in recent years for modelling idealised valleys (Touhei and Yoshida, 1988), 2-D basin response under SV-wave excitation (Ohtsuki and Harumi, 1983; Loukakis and Bielak, 1995) and site-specific response studies (Bardet et. al., 1992; Zhang and Papageorgiou, 1995; Bielak et. al., 1997). Kawase (1996a,b) used a 2-D FEM to investigate the basin-edge effect in Kobe during the 1995 earthquake. Finite-element methods have also been used in 2-D to model source processes (Loo and Jin, 1984). Three-dimensional finite-element techniques have been used to model 3-D basin resonance (Rial et. al., 1992), basin-edge induced love-wave propagation (Toshinawa and Ohmachi, 1992) and general basin response (Bao et. al., 1997).

Loukakis and Bielak (1995) discuss two issues concerning the use of finite-element methods for modelling seismic motions in unbounded domains. The first is the need to limit the domain with an artificial boundary. Viscous boundaries using a spring dashpot model (Lysmer and Kuhlemeyer, 1969), transmitting boundaries (Lysmer and Waas, 1972), non-reflecting boundaries by averaging fixed (Dirichlet) and free (Neumann) boundary conditions (Smith, 1974) and Kosloff's Method (Kosloff and Kosloff, 1986; Seki and Nishikawa, 1988) have all been used to successfully counter the problem of reflections. The second issue is how to incorporate excitation into the finite-element mesh, a problem that has been solved by an effective force method and domain decomposition technique (Bielak and Christiano, 1984; Cremonini et. al., 1988). Other solutions involve the use of an internal source (eg. Hisada et. al., 1998).

2.2 Seismic Response of Sediment-Filled Basins

When soft surface layers are laterally confined by a more rigid basement rock as in a sedimentary basin or valley, in addition to one-dimensional amplification, various

two- and three-dimensional effects begin to contribute to the amplification of seismic motions in the long-period/low-frequency range below about 4 Hz (Field, 1996). Multi-dimensional effects occur as the confined basin is able to trap seismic energy by internal reflections in both the horizontal and vertical directions. A confined structure gives rise to the interaction of two basic phenomena; firstly resonance in the vertical direction as energy is repeatedly reflected between the basement interface and the free surface, and secondly, the diffraction and reflection of surface-waves from the sharp discontinuity at the sides of the basin producing resonance and constructive interference in the horizontal direction. Good overviews of the basin response problem may be found in Aki (1988, 1993), Bard (1994), Bouchon (1995), Hisada and Yamamoto (1996), Kazuyoshi (1995) and Rassem et. al. (1997).

The most significant pioneering work in basin response is generally accredited to Bard and Bouchon (1980a,b) who use a two-dimensional Aki-Larner technique in the time-domain to show that local surface waves are generated at the edge of basins and propagate back and forth to produce a response of both high amplification and long-duration. They also demonstrated that for the case of incident SH waves, Love waves (Love, 1892, 1911) are produced; and for incident SV or P waves, Rayleigh waves are produced from the basin edge. Bard and Bouchon (1980b, 1985) later used the Aki-Larner technique to model basin resonance in two-dimensions.

Significant observational work by King and Tucker (1984) and Tucker and King (1984) found that valley response was strongly dependant on the input signal's frequency and angles of incidence and azimuth, and the cross-valley position. Ground motion at valley-edge and mid-valley sites differed by as much as a factor of five.

2.2.1 DIFFRACTED SURFACE WAVES

Because the each side of a valley forms a sharp lateral discontinuity in material properties, surface-waves are generated at the discontinuity and are diffracted to propagate laterally across the basin. They are commonly referred to as edge-waves or basin-edge induced waves. When the sediments are vertically heterogeneous (layered), the diffracted Love waves are dispersive (as are the Rayleigh waves) and

may travel through deeper layers at different velocities. The main effect of edge waves is to increase the duration of shaking in the basin.

The effects of basin-edge induced waves have been noted and modelled in two-dimensions for Mexico City during the 1985 Michoacan earthquake (eg. Sanchez-Sesma et. al., 1988b; Kawase and Aki, 1989), the San Fernando Valley during the 1971 San Fernando (Vidale and Helmberger, 1988) and 1994 Northridge (Pitarka and Irikura, 1996) earthquakes, the Los Angeles Basin during the 1994 Northridge earthquake (Schrivner and Helmberger, 1994; Graves, 1995; Pitarka and Irikura, 1996), the Coachella Valley, California, during the 1992 Landers/Big Bear aftershock sequence (Field, 1996), the La Molina Valley, during the 1974 Lima, Peru earthquake (Espinosa et. al., 1977; Zahradnik and Hron, 1987), the Kanto Basin, Japan during the 1984 Nagano earthquake (Yamanaka et. al., 1989), the Ashigara Valley, Japan during the 1990 Odwara earthquake (Pitarka et. al., 1994, 1996), and Kirovakan, Armenia, during the 1988 earthquake (Bielak et. al., 1997). Several less site-specific studies have also been made (eg. Papapeorgiou, 1996; Sanchez-Sesma et. al., 1988a; Wang, 1996).

Two-dimensional studies have shown surface-wave amplitudes are dependant on the seismic-velocity contrast between sediment and bedrock, yet vary little with the shape of the basin-edge (Shibuya, 1992). Loukakis and Bielak (1995) concluded that surface-wave amplification is strongest when the angle of incidence is at the critical angle, when the horizontal component of the S-wave velocity equals the P-wave velocity and a strong coupling occurs. Both Zhang and Papageogiou (1995) in a study of the of the highly 3-D Marina District, San Francisco, and Pitarka et. al. (1994) for the Ashigara Valley conclude that a far more computationally efficient 2-D model, despite its shortcomings, is very useful for estimating ground motions for engineering considerations.

Three-dimensional simulations of basin response from Californian earthquakes (Frankel and Vidale, 1992; Frankel, 1993a,b; Graves, 1993; Olsen and Archuleta, 1996) have used the finite-difference method and a double-couple point source to combine the effects of a fault rupture with diffracted waves in a three-dimensional velocity model. Studies have been made of the San Fernando Valley using a 3-D FEM

(Bao et. al., 1997), the Kanto Basin, Japan, using the Gaussian beam method (Kato et. al., 1993) and the BEM (Hisada et. al., 1993). Several non site-specific studies have also been made using 3-D techniques (Sanchez-Sesma and Luzon, 1995; Chavez-Perez et. al., 1989; Toshinawa and Ohmachi, 1992).

2.2.2 *Multi-Dimensional Basin Resonance*

One-dimensional vertical resonance in a flat soft layer over a homogeneous half-space is a phenomena for which the resonant frequencies (eigenfrequencies), f_n, can be described analytically as a function of the fundamental resonant frequency, f_1, the shear-wave velocity ,V_s, and the thickness, H, of the soft layer (Haskell, 1960).

$$f_m = f_1(2m-1) \qquad m=1,2,3,...\infty \qquad [2.1]$$

$$f_1 = \frac{V_S}{4H} \qquad [2.2]$$

When a basin is bounded by bedrock on two opposing sides such as in a valley, diffracted Love waves propagate from both sides creating horizontal resonance. The interaction of resonant modes (eigenmodes) in both the vertical and horizontal directions forms a pattern of two-dimensional resonance in the basin.

Analytical methods for determining the amplification of two-dimensional resonant ground motions have been made for ideal semi-circular (Trifunac, 1971) and semi-elliptical valleys (Wong and Trifunac, 1974). Bard and Bouchon (1985) made the first comprehensive discussion on two-dimensional resonance patterns, and gave an analytical solution to the resonant frequencies (eigenfrequencies) of a valley with simple rectangular cross-section and infinite length (often termed rectangular-cylindrical), containing homogeneous elastic sediments surrounded on three sides by a rigid basement.

$$f_{mn} = f_1\sqrt{(2m-1)^2 + n^2\left(\frac{2H}{L}\right)^2} \qquad n,m=1,2,3,...\infty \qquad [2.3]$$

Here H is the valley depth, L is the width, f_1 is the fundamental natural frequency of a flat layer defined by equation [2.2], and f_{mn} is the eigenfrequency corresponding to the m^{th} vertical eigenmode and n^{th} horizontal eigenmode. Thus eigenfrequencies are a function only of the valley dimensions and sediment shear velocity. The displacement associated with each eigenmodeshape, $u_{mn}(x,y)$, is given by (Bielak, et. al., 1997)

$$u_{mn}(x,y) = \sin\frac{(2m-1)\pi y}{2H}\sin\frac{n\pi x}{L} \qquad n,m = 1,2,3,...\infty \qquad [2.4]$$

where the origin of the x-y coordinate system is the lower left corner of the cross-section, y is measured vertically up and the x-axis is horizontal. These modeshapes have been plotted in Figure 2.1. For each vertical mode, m, there exists a set of n horizontal modes. The ground surface response for an input frequency, f_{mn}, will have $(n+1)$ extremum points alternating between maxima and minima.

At the surface, modeshape u_{mn} has n extremum (E_{ni}) points and $n+1$ nodal (N_{nj}) points. The x-position (across the valley) for each is given by

$$x(E_{ni}) = \frac{2i-1}{2n}L \qquad i = 1,2,3,...n \qquad [2.5a]$$

$$x(N_{nj}) = \frac{j}{n}L \qquad j = 1,2,3,...n+1 \qquad [2.5b]$$

where L is again the valley width. Each point on Figure 2.2 represents an extremum (crest or trough) or a nodal (zero displacement) point in the mode shape expression on the surface. If the input contains a range of frequencies, we would expect the surface response (in the frequency-domain) to exhibit a pattern of extremum points as shown, with each higher vertical mode (and corresponding set of n horizontal modes) overlaying the previous vertical mode set. Thus the higher the frequency, the more complex the mode shape. Extremum points and nodal points for each vertical set lie on a distinctive set of curves. Bielak et. al. (1997) uses the terms extremum line and nodal line to describe them.

Solutions for two-dimensional eigenfrequencies have also been found for semi-circular cross-sections (Wirgin, 1995a,b), semi-elliptical cross-sections (Rial, 1989a,b; Rial and Ling, 1992) and valleys of smooth arbitrary shape (Ling and Rial, 1994; Zhou and Dravinski, 1994).

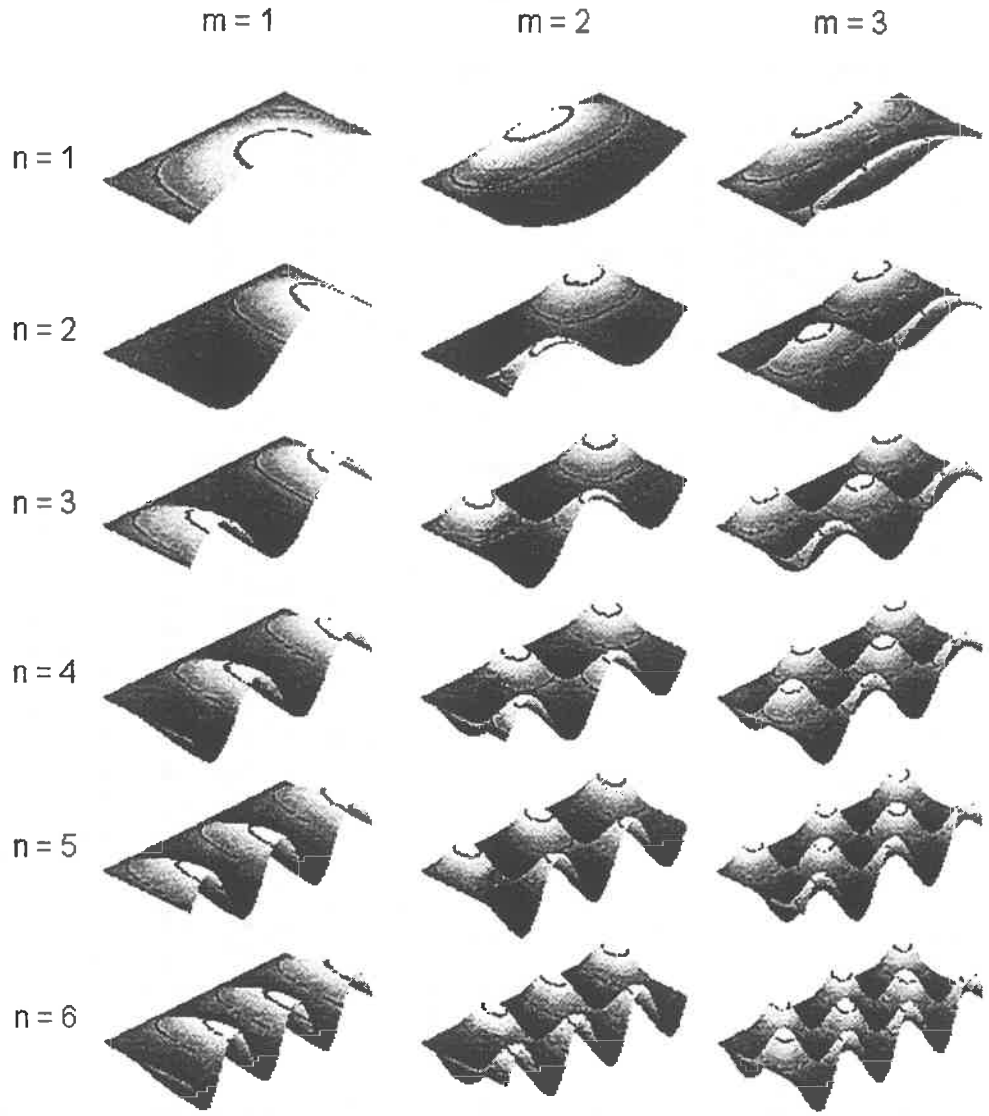

Figure 2.1. Anti-plane SH modeshapes, u_{mn}, of two-dimensional resonance in a valley of rectangular cross-section bounded on three sides by a rigid basement. Each cross-section is aligned such that the unbounded (ground) surface is on the lower right, with depth increasing toward the top left of the figure. Particle motion is in the out-of-plane (up-down) direction. Shown are the first three vertical (m) modes, each with the first six horizontal (n) modes.

Discussion on the 3-D resonant nature of enclosed basins has been made by Rial (1989a,b), where an analytical approach is used to estimate the resonant eigenfrequencies for a semi-ellipsoidal basin. Rial et. al. (1992) use a three-dimensional finite-element technique to model 3-D basin resonance. Stephenson (1974, 1975, 1989a,b) derives expressions for 3-D modes of cellular resonance in a cylindrical basin based on observations of resonant amplification in the Hutt Valley.

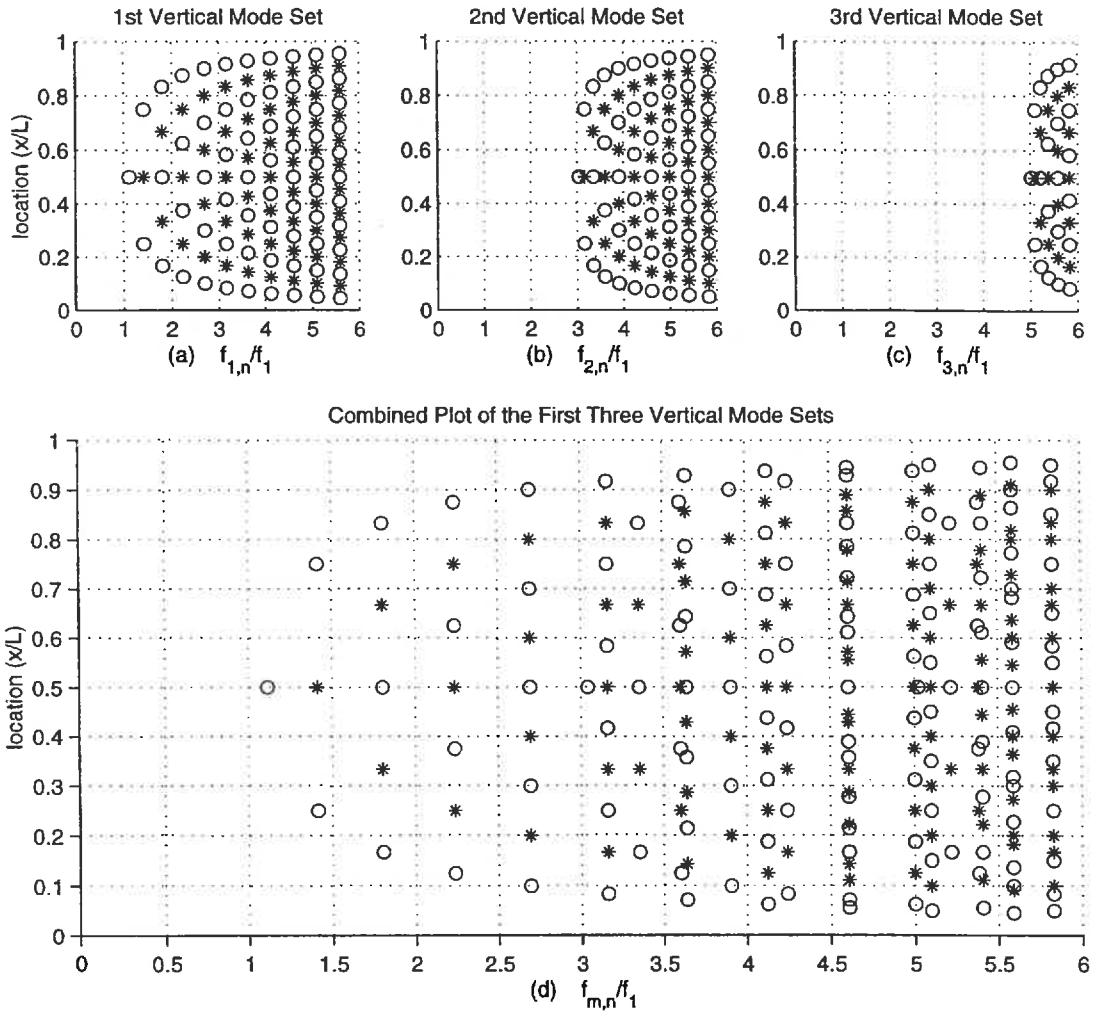

Figure 2.2. Theoretical resonant response of a dimensionless rectangular-cylindrical valley set in a rigid half-space. Locations (in space and frequency) of crests and troughs (o), and nodal points (*) are shown for each resonant mode. Subplots (a), (b), (c) each show a set of horizontal modes for each of the first three vertical modes respectively, while (d) shows the combined modal response (after Bielak et. al., 1997).

2.2.3 THE BASIN-EDGE EFFECT

The 1995 Hyogo-ken Nanbu earthquake which devastated Kobe and surrounding cities was characterised by a narrow band of intense damage about 0.8 to 1.0 km south of the Suma fault system, a strong lateral discontinuity between granitic bedrock and deep Pliocene and Pleistocene sediments of Osaka Bay. The band of intense damage extended parallel to the fault for some 30 km between Kobe and Nishinomiya (Finn et. al., 1996; Park et. al., 1995).

Kawase (1996a,b) hypothesised that amplification causing the damage belt in Kobe was due (at least in part) to constructive interference between the horizontally propagating Love waves and the direct shear wave propagating vertically through the sediments a short distance away from the basin side, a phenomenon he subsequently termed the '*basin-edge effect*'. In broad terms the waves from a rupture at depth reach the ground surface earlier through the rock and diffract surface waves into the basin. For the case of Kobe, the diffracted wave-field had travelled a horizontal distance of 0.8 to 1.0 km before the direct waves arrived through the sediment. Kawase used a finite-element method to analyse a two-dimensional velocity model of the deep Osaka basin and bounding bedrock and substantiate his hypothesis. Similar results have since been obtained by Pitarka et. al. (1998) using a three-dimensional velocity model and finite-difference method (FDM) to model the coupling of rupture effects (directivity) and the basin-edge effect in Kobe.

Graves et. al. (1998) identify the band of damage found in Santa Monica following the 1994 Northridge earthquake as an example of the basin-edge effect. The damage occurred just south of the 1km deep, complex basin-edge structure formed by the actively thrusting strand of the Santa Monica Fault. They use a 2-D FDM to calculate the P-SV and SH wave responses in the damaged area. Results show fairly conclusively a peak in displacements some 2km south of the fault trace. Although the mechanism of amplification is clear, there is still uncertainty as to the characteristics of this effect, especially the frequency content. They point out that the variety of building types damaged may indicate a broad-band nature in the amplification, suggesting that it may be due to interference between the short-period direct body waves and the longer-period basin-generated surface waves.

Prior to the recognition of its cause, several observations and modelling studies from various basins have given results that suggest the action of the basin-edge effect. Vidale and Helmberger (1988) found amplification at the edge of the San-Fernando Valley during the 1971 earthquake, and using a 2-D elastic FDM, attributed it to the action of diffracted basin-edge waves. Larkin and Marsh (1991) found that amplification effects were most significant at the valley edges by 2-D non-linear FDM modelling of idealised basins. Moczo and Bard (1993) clearly identified narrow stripes of intense shaking parallel to strong lateral discontinuities using a 2-D FDM with anelastic attenuation and vertically incident SH waves. Sanchez-Sesma and Luzon (1995) using a 3-D boundary-element method noted very large amplification of incident SH waves and attributed it to the 'constructive interference of various refracted waves. Pitarka et. al. (1994, 1996) found amplification at the basin edge for incident SH waves using a 2-D elastic FDM to approximate 3-D wave propagation from a double-couple point source in the Ashigara Valley during the 1990 Odawara (Japan) earthquake. They attributed the amplification to the basin structure. Pitarka and Irikura (1996) with a similar 2-D elastic FDM and double-couple point source found amplification along the northern edge of the Los Angeles basin during the 1994 Northridge earthquake, and accredited it to constructive contributions from both site effects and source processes.

Sketchy reports in Prescott (1982) for the 1868 California earthquake and Weischet (1963) for the city of Valdivia during the 1960 Chile earthquake, describe possible occurrences of the basin-edge effect. Moczo and Bard (1993) mention bands of intense damage adjacent to geologic lateral discontinuities from the 1909 France, 1979 Montenegro (Italy) and 1980 Irpinia (Italy) earthquakes. Other occurrences of bands of damage along basin edges have been reported following the Skopje, Yugoslavia earthquake of 1963 (Poceski, 1969), the Miyagiken-Oki, Japan earthquake of 1978 (Kubo and Isoyama, 1980) and the Shidian basin (China) during the 1976 Longlin earthquake (Yuan et. al., 1992).

For the case of a simple rectangular cross-section containing a homogeneous elastic sediment as shown in Figure 2.3, we may calculate the approximate position of the basin edge effect from the valley wall. Setting t_1 and t_2 to be the vertical travel times of a shear wave through the rock and sediments respectively, we obtain

$$t_1 = A + \frac{H}{V_R} \quad \text{and} \quad t_2 = A + \frac{H}{V_S} \qquad [2.6a,b]$$

such that $$t_3 = t_2 - t_1 = \frac{H}{V_S} - \frac{H}{V_R} \qquad [2.7]$$

where t_3 is the difference in arrival times at the surface, or the time in which the laterally propagating Love wave has to travel out into the sediments to meet the vertically incident shear wave to produce the constructive basin edge effect. The depth of sediments is H, V_R and V_S are the shear wave velocities of the rock and sediments respectively, while A is a constant representing travel time from the source.

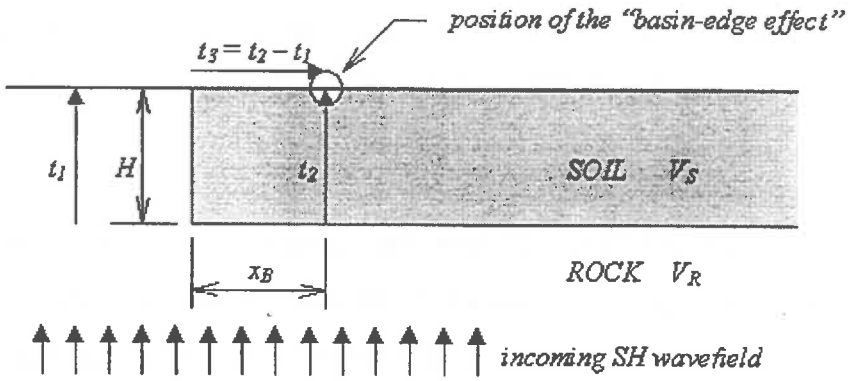

Figure 2.3. Geometry of a simple rectangular basin-edge (lateral discontinuity) showing the action of the basin-edge-effect. Times t_1 and t_2 represent travel times of the direct shear wave through the rock and sediments respectively, while t_3 is the travel time of the diffracted Love wave out into the sediments.

The position of the basin edge effect, x_B, measured horizontally from the vertical edge, becomes

$$x_B = t_3 V_L = V_L \left(\frac{H}{V_S} - \frac{H}{V_R} \right) \qquad [2.8]$$

and if we assume the Love wave phase velocity of the sediments, $V_L \approx V_S$, the position of the basin edge effect becomes

$$x_B \approx H\left(1-\frac{V_S}{V_R}\right) \qquad [2.9]$$

As the position of the basin edge effect depends strongly on the velocity of the horizontally propagating Love wave, it is also a frequency dependant phenomenon. In a multi-layered system of soft sediments it is difficult to tell through which horizontal layer the causal Love wave will travel. Shear velocities generally increase with depth, pushing the effect further into the basin.

2.3 Active Tectonics in the Wellington Region

The Wellington region is located at the southern end of the North Island Shear Belt. The area has been largely formed by active tectonics at the obliquely subducting boundary between the Pacific and Australian Plates. Dextral faulting in the area, trending to the north-east, dates back to the Late Tertiary.

On the north-eastern shore of Port Nicholson lies the Lower Hutt, an actively subsiding sedimentary valley formed by the tilting action of a large bedrock block to the east. On both sides it is bounded by a range of hills, each reaching around 300-400 metres in elevation. Ten kilometres inland, the valley narrows to a gorge that separates the Lower Hutt from the Upper Hutt. A wedge of sediments that has accumulated over successive glacial and inter-glacial periods extends down to Petone. The actively aggrading Hutt River has deposited the most recent sediments.

At the southern end of Port Nicholson, downtown Wellington lies atop the smaller Te Aro sedimentary basin, and extends out into Lambton Harbour on an area of reclaimed land. Begg and Mazengarb (1996), Cotton (1960), Lensen (1958), and Stevens (1958, 1990, 1991) contain good descriptions of geology in the Wellington area.

2.3.1 The Wellington Fault

One of the most striking landscape features in the area is the Wellington Fault, which has created a highly visible lineation in a NE-SW direction from the south coast, over

the hills, beside down-town Wellington, along the western shores of Port Nicholson, and up the western edge of the Hutt Valley before disappearing into the Tararua ranges to the north. The Wellington Fault is one of the major active dextral strike-slip faults in New Zealand and represents a significant hazard to the greater Wellington region. Both Lower Hutt City and the central business district of Wellington City lie immediately adjacent to the fault on essentially alluvial sediments forming a basin bounded by firm rock. The presence of the Wellington Fault was first recognised by McKay (1892), while it was named by Cotton (1912).

The 75 km long Wellington-Hutt Valley Segment of the Wellington Fault appears to behave in a characteristic fashion with the occurrence of maximum-magnitude ruptures at regular intervals. Paleoseismic studies (eg. Grant-Taylor, 1967; Lewis, 1989; Berryman, 1990; Van Dissen and Berryman, 1991; Van Dissen et al., 1992a, 1996) suggest a characteristic dextral offset of 3.2-4.7 metres with a small up-thrusting component of less than 1 in 10, or 0.3 metres (Berryman, 1990). The lateral slip rate has been a relatively constant 6.0-7.6 mm/year through the last 140 ka. (Berryman, 1990). The length of rupture and amount of slip have been used to estimate a probable surface-wave magnitude, M_S, of 7.1-7.8 (Berryman, 1990) and moment magnitude, M_W, of 7.3-7.9 (Van Dissen et. al., 1996). These figures indicate that a major rupture on the Wellington Fault would be of similar source characteristics, yet slightly larger than the 1995 Hyogo-ken Nanbu earthquake.

Elapsed time since the last rupture has been estimated at 290-440 cal B.P. (calendar years before A.D. 1950 AD), and the second most recent, 660-720 cal BP (Van Dissen and Berryman, 1996). The recurrence interval may be estimated from slip rate data to be 420-780 years (Van Dissen et. al., 1992a), or from time between the two most recent events to be 220-430 years. The probability of rupture in the next 100, 300 and 1000 years has been estimated at 25 $\pm$ 20%, 60 $\pm$ 30% and 90 $\pm$ 10% respectively (Van Dissen and Berryman, 1990).

A Wellington Fault earthquake is expected to produce mainly strike-slip and some thrust movement from a hypocentre around 10 km deep. Rupture length and slip suggest that the fault plane is upper crustal and dipping slightly to the west, not reaching the shallow-dipping subduction plane like the nearby Wairarapa Fault. The

path of seismic wave propagation will be essentially vertical, slightly inclined to the east. Source radiation (especially in the direction of the fault) is likely to be a significant factor, although the rupture could just as easily propagate in either or both directions.

2.4 *Seismic Wave Amplification Studies in the Lower Hutt and Wellington*

Several studies have been conducted looking at the frequency-dependant amplification found in recorded data from Wellington and the Lower Hutt. The exclusive availability of only relatively weak-motion records places questionable limitations on the applicability of these results to the estimation of strong shaking, although their usefulness for correlation with elastic modelling is nonetheless highly valuable.

Stritharan and McVerry (1992) describe ground shaking in the Lower Hutt Valley from the strong-motion instrument data of nine earthquakes between 40 and 240 km away with peak ground accelerations (PGA) in the order of 0.01-0.15g. They calculated Fourier spectral ratios (FSR) up to a factor of 10 at some recorder sites in the deepest part of the valley, and constructed a microzone map of the Lower Hutt Valley, which indicates areas that received the strongest ground shaking. Unusually located peaks from some earthquakes suggested the influence of two, or even three-dimensional site amplification.

Taber and Richardson (1992) calculated FSR from recorded weak motions at several Wellington City sites. They found particularly high amplification in Te Aro, on Kent Terrace, and close to the harbour. Average FSR of 5.1 to 6.6 were found within the narrow frequency range 1 to 2 Hz. Taber et. al. (1993) compares strong motion recorded data (PGA's between 0.005 and 0.10g) to weak motions (PGA's between 0.00005 and 0.004g) at six sites in the Lower Hutt and ten sites in Wellington. Non-linear behaviour does not appear to be significant at these levels of shaking. For strong motions, deep sites in the Hutt Valley had a greater low-frequency response while the peak amplification for a site near the edge occurred at higher frequencies.

Taber and Smith (1992) describe the spectral amplification at 24 weak-motion sites in the Lower Hutt Valley. Amplification of shaking appears to increase gradually when moving down-valley from the Taita Gorge to the Petone foreshore. They find peak FSR up to a factor of 14 at the lower end of the valley. Amplification at most sites occurred over a broad frequency band from 0.5 to 5.0 Hz. In general, the highest spectral peaks occur in the 1 to 3 Hz range. Van Dissen et. al. (1992b) have mapped out ground shaking hazard zones and estimated PGA in the Lower Hutt Valley due to a Wellington Fault rupture based on geological data and weak-motion data from the above studies.

Chapter 3: ARCHIMEDES F.E.M. SOFTWARE

Archimedes (Bao et. al., 1996) is an integrated set of computational software tools for performing large finite element method (FEM) simulations on parallel computers. It was originally developed for two-dimensional elastic simulations (eg. Bielak et. al., 1997), while three-dimensional (eg. Hisada et. al., 1998) and non-linear techniques are now in the final stages of refinement.

The software was developed as part of the National Science Foundation (NSF) Grand Challenge Quake Project, a joint venture between the Department of Civil and Environmental Engineering and the Department of Computer Science at Carnegie Mellon University (Pittsburgh, PA.), the Southern California Earthquake Center at the University of Southern California and the National University of Mexico. The Quake project has the goal of developing computer simulation methods for the prediction of ground motion in sedimentary basins during strong earthquake shaking.

Finite element methods allow the use of an unstructured mesh, enabling elements of differing sizes and proportions to give a high degree of geometric detail. Node spacing can be tailored in proportion to the local shear-wave velocity to give similar numerical accuracy and high computational efficiency throughout the geometry of the problem. Thus for problems such as ours, with shear-wave velocities differing by as much as a factor of 15 (100m/s and 1500m/s), large reductions in computation requirements can be made. For 2-D applications, the number of calculations is reduced by a power of two in the high-velocity region of the calculation area, whilst for 3-D, a power of three. For example, our 2-D unstructured mesh for the cross-section through Lower Hutt Central contained only 29,596 nodes compared to the ~200,000 nodes which would have been required in a uniform (structured) mesh of the same cross-section. Accordingly, the Archimedes simulations in 2-D are able to be run on single processors such as a 512 Megabyte D.E.C. Alpha operating under a UNIX system, with a processing time in the order of hours, while large 3-D simulations may be run on parallel machines over a number of days (eg. Bao et. al., 1997).

The structure of the tool set is shown in Figure 3.1. Input includes (a) the geometry and properties of the geological model and (b) an FEM algorithm. The tool set, developed by Dave O'Hallaron and Jonathan Shewchuk of the Department of Computer Science at CMU, includes the following:

1. ***Triangle*** (Shewchuck, 1996) is a two-dimensional triangular mesh generator designed specifically for FEM's. It uses Delaunay triangulation algorithms to create an efficient, unstructured mesh. Input to Triangle includes the geometry of layer boundaries, free-surfaces and computational boundaries, maximum triangle area and minimum internal angle; all in the form of an ASCII data file (.poly extension). It also has the option of creating quadratic elements (six nodes per element) for more efficient computation. Output from Triangle consists of a set of three data files (.node, .ele, and .poly extensions) describing the coordinate points of each node and the nodes associated with each element. The 3-D equivalent, ***Pyramid***, uses similar techniques to generate a three-dimensional unstructured tetrahedral mesh.

2. ***Show Me*** is a C program for graphically displaying on the screen meshes generated by Triangle. It also has functions for writing images to postscript files and for viewing the input geometry to Triangle.

3. A set of three programs - ***Absorb***, ***Slice*** and ***Parcel*** - are used to refine, partition and reorganise the mesh data into a form that may be used on parallel processors. For our purposes, these programs were run with the input argument of only one processor. Parcel also requires an extra input file (with a .fi extension) containing five lines describing the input ricker-wave central frequency, the time-step size and the simulation length.

4. ***Author*** is the central tool of Archimedes. As input it uses data files (with extensions .adj, .def, .ele, .node, .pack, .part and .ri) from the previous tools, as well as an FEM code file (with a .arch extension) written in ANSI C and containing an element-level description of the finite-element approximation, and a high-level description of the finite-element algorithm. The job of Author is to compile these files into a processor code for running the simulation.

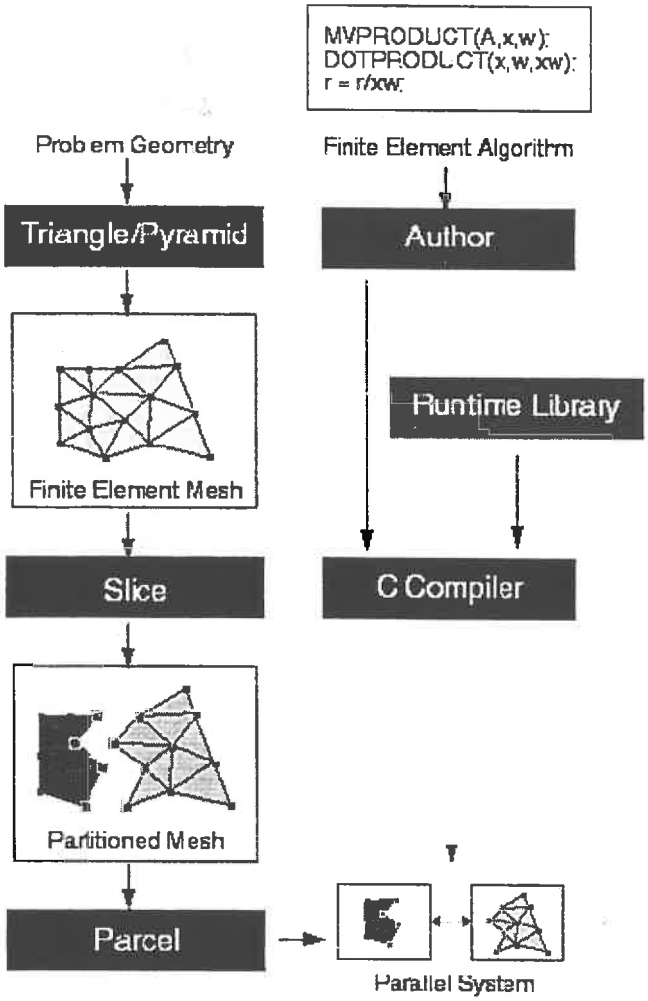

Figure 3.1: Structure of the Archimedes software tool set (after Bao et. al., 1996).

Up-to-date information and a description of the Archimedes tool chain may be found on the World Wide Web at http://www.cs.cmu.edu/~quake/archimedes.html. Complete documentation for the use of Archimedes has not yet been published, although complete instructions on the use of Triangle, the two-dimensional triangular mesh generator may be found at http://www.cs.cmu.edu/~quake/triangle.html.

3.1 MESH GENERATION

The degree of geometrical detail we have used for the bedrock and sediment-layer boundaries is on par with the degree of certainty we have from existing geological data in the Wellington region. The cross-sections are modelled with a set of straight

and circular-curve segments along layer boundaries. Greater complexity could easily be incorporated if better quality geological data existed.

For engineering purposes we are concerned with ground motions in the low frequency (long period) range. In order to achieve reasonable accuracy, it is desirable to use a maximum node spacing in the finite-element mesh of one-eighth (Kuhlemeyer and Lysmer, 1973) to one-fifth (Lysmer et. al., 1975) the shortest wavelength. Using six-noded quadratic-triangular elements, with an intermediate node between each vertex, we have worked toward a maximum element size of one-fourth the minimum wavelength, λ_{min}. Thus in order to simulate seismic motions within the frequency range $0 \leq f \leq f_{max}$, the corresponding maximum element size is required to be less than $\lambda_{min}/4 = V_S/4f_{max}$, where V_S, is the shear-wave velocity of the unit. Table 3.1 shows the element mesh size used for each of the Lower Hutt units (see Chapter 4) based on a maximum frequency of 6 Hz.

Layer	Shear Velocity V_S (m/s)	Min Wavelength $\lambda_{min}=V_S/f_{max}$ (m)	Max Element Size $\lambda_{min}/4$ (m)	Max Element Area (m^2)
A	100	16.7	4	9
B	175	29.2	8	27
C	285	47.5	12	71
D1	325	54.2	14	91
D2/3	460	76.7	20	184
D4/5	600	100.0	25	313
D6	675	112.5	30	395
E	1500	250.0	60	1953

Table 3.1. Showing the mesh sizes used to model each geological unit in the Lower Hutt Valley. The minimum wavelength and maximum allowable element size are based on a maximum frequency, f_{max}, of 6.0 Hertz.

3.2 THE FINITE ELEMENT ALGORITHM

We have the problem of elastic wave propagation within a heterogeneous soft basin surrounded by a homogeneous half-space of rock. The half-space is idealised as of uniform cross-section and infinite-length (often called a cylindrical cross-section). We want to consider the effect of a transient anti-plane SH wave incident on this half-space. An FEM analysis allows us to treat the whole basin as piecewise uniform so that the displacement field, u, within each element, satisfies the wave equation

$$\frac{\partial^2 u}{\partial t^2} = V_s^2 \nabla^2 u \qquad [3.1]$$

Boundary conditions are imposed which require the continuity of force and displacement across each element, and the absence of stress at the free surface. The equation of motion we wish to solve over the computational domain is a system of ordinary differential equations of the form

$$M\ddot{u} + C\dot{u} + Ku = f(t) \qquad [3.2]$$

where M, C, and K are the global mass, damping and stiffness matrices; u, $\dot{u}$ and $\ddot{u}$ are the time-dependant nodal displacements, velocities and accelerations respectively, and $f(t)$ is the applied nodal force

3.2.1 THE CONSTITUTIVE MODEL

Soil and rock materials are assumed to be linearly elastic, isotropic and homogeneous within each layer. In fact real soils are highly anisotropic and inhomogeneous and are not so clearly defined into separate layers as the model assumes. Borehole logs from the Hutt Valley (eg. Begg and Mazengarb, 1996; Dellow et. al., 1992) give an idea of the actual sub-surface conditions in the Port Nicholson basin; closely spaced layers of peat, sand and gravel are found throughout the column. Material properties (dilatational- and shear-wave velocity, density, shear modulus, Young's modulus and Poisson's ratio) are not precisely known, and may vary considerably within each layer. Greywacke bedrock in the Wellington region is also far-from-ideal, being

highly fractured, especially in the fault-parallel direction, and variably weathered. The assumed homogeneity of each geological unit appears crude, yet is a common assumption in many geotechnical applications rendering functional results.

The usefulness of a linear elastic model for application in the prediction and modelling of strong ground motion is the source of some controversy. In practice, near-surface sediments will generally behave in a non-linear fashion during large earthquakes, giving a response somewhat different than predicted by the model. The subject is discussed further in section 7.3.

3.2.2 MATERIAL DAMPING

Damping has the effect of soaking up energy within the soil matrix thus inhibiting wave propagation. We have assumed a likely value for the damping ratio, ζ, of 0.02 (2% of critical) in the soil mass. In fact we use a two-parameter (α and β) viscous Rayleigh damping model. Within each finite element, the damping matrix, C, has the form

$$C^e = \alpha\omega_o M^e + \frac{\beta}{\omega_o} K^e \qquad [3.3]$$

where α and β are arbitrary constants, ω_o is a reference frequency, and M^e and K^e are the element mass and stiffness matrices. The Rayleigh damping model thus varies with frequency, so we select the α and β parameters in such a way that the damping ratio averages out to 2% ($Q \approx 25$) across the desired frequency range (eg. 0.1-6.0 Hz). This model is shown in Figure 3.2, where damping is plotted with respect to frequency. Damping over the shown frequency range varies between 1.0 and 5.7 percent ($50 \geq Q \geq 9$). The approximate relationship between the damping ratio, ζ, and the quality factor, Q, is given by Bert (1973), $Q \approx 1/(2\zeta)$. As we have no real data on soil damping properties in the Wellington area, this frequency dependant Rayleigh damping model is assumed to be adequate.

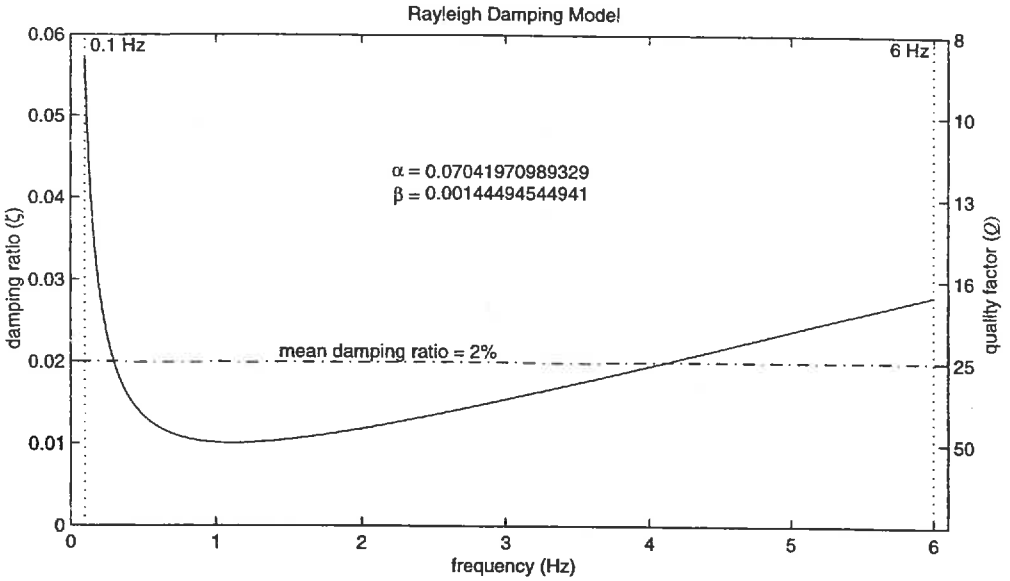

Figure 3.2. The viscous Rayleigh damping model used to approximate a constant two-percent damping over the desired frequency range. Here, the frequency range of interest is 0.1 – 6.0 Hz, and the required damping is 2% ($Q \approx 25$). The α and β values shown are those used in the Archimedes simulation.

3.2.3 ABSORBING BOUNDARY

Bedrock extends many kilometres below and to the sides, away from the soft basin. To keep memory requirements and calculation time to a minimum, we require a finite computational domain extending no more than a few hundred metres (several node spacings) into the rock. This introduces the problem of reflections from the artificial outer boundary, which need to be interrupted before they influence results. Al-Hunaidi (1989) describes and compares various solutions to this particular problem, one of which is the viscous boundary technique used here. A semi-circular absorbing boundary has been placed around the lower extent of the model, with the viscous boundary conditions, a distributed set of spring and dashpot models, imposed on the arc. The circular boundary has the advantage of being easy to describe mathematically as a singular bounding segment.

3.2.4 INPUT SIGNAL

The input motion is a single vertically propagating Ricker wavelet. In the time-domain, the displacement trace, $d(t)$, is given by (Ricker, 1940)

$$d(t) = A\left(1 - 2\pi^2 f_0^2 t^2\right) e^{-\pi^2 f_0^2 t^2} \qquad [3.4]$$

where f_0 is the central (dominant or characteristic) frequency in cycles per second (Hertz) and A is the wavelet amplitude. In Archimedes, this same wave is approximated by

$$d(t) = \begin{cases} a_1(\omega_0 t)^4 + a_2(\omega_0 t)^6 + a_3(\omega_0 t)^8 & 0 \le t < \frac{\sqrt{6}}{\omega_0} \\ \left[\frac{1}{4}\left(\omega_0 t - 3\sqrt{6}\right) - \frac{1}{2}\right] e^{-\frac{1}{4}\left(\omega_0 t - 3\sqrt{6}\right)} - \dfrac{13e^{-13.5}}{0.5 + 13e^{-13.5}} & \frac{\sqrt{6}}{\omega_0} \le t < \frac{5\sqrt{6}}{\omega_0} \\ a_1\left(\omega_0 t - 6\sqrt{6}\right)^4 + a_2\left(\omega_0 t - 6\sqrt{6}\right)^6 + a_3\left(\omega_0 t - 6\sqrt{6}\right)^8 & \frac{5\sqrt{6}}{\omega_0} \le t < \frac{6\sqrt{6}}{\omega_0} \\ 0 & \textit{elsewhere} \end{cases} \qquad [3.5]$$

where $\omega_0 = 2\pi f_0$, and a_1, a_2 and a_3 are polynomial coefficients. Here the wavelet has been given finite start and finish points by substituting 3rd order polynomials at the start and end of the function. The peak displacement now occurs at $3\sqrt{6}/(2\pi f_0)$ seconds. The Ricker waveform can be visualised in terms of displacement, *d(t)*, velocity, *v(t)*, or acceleration, *a(t)*, as shown in Figure 3.3.

With a central frequency of 2 Hz, the ricker pulse contains energy within the range 0-6 Hz. However, below 0.3 Hz and above 5.0 Hz, calculations within Archimedes appear to become unstable. At the low frequency limit, calculations tend towards a small, non-zero number, and at high frequencies the calculations begin to oscillate wildly.

The motion is entirely in the form of anti-plane SH-waves (horizontally-polarised shear waves) as is commonly used to represent motion from a strike-slip fault (eg. Kawase, 1996a). A problem arises because the major source of the motion is from outside the computational domain. For the case of the Wellington Fault, a characteristic strike-slip rupture is likely to release most of its energy in the form of SH-waves from a depth in the order of 10 km. Thus the excitation is incorporated into the computational domain along a smaller semi-circular arc inside the absorbing boundary. The time of excitation of each node on the arc is adjusted so to represent a pulse starting simultaneously over the width of the mesh from the same depth. The

method used is that developed by Bielak and Christiano (1984) and Cremonini et. al. (1988) whereby nodal forces are applied along this inner arc of finite elements.

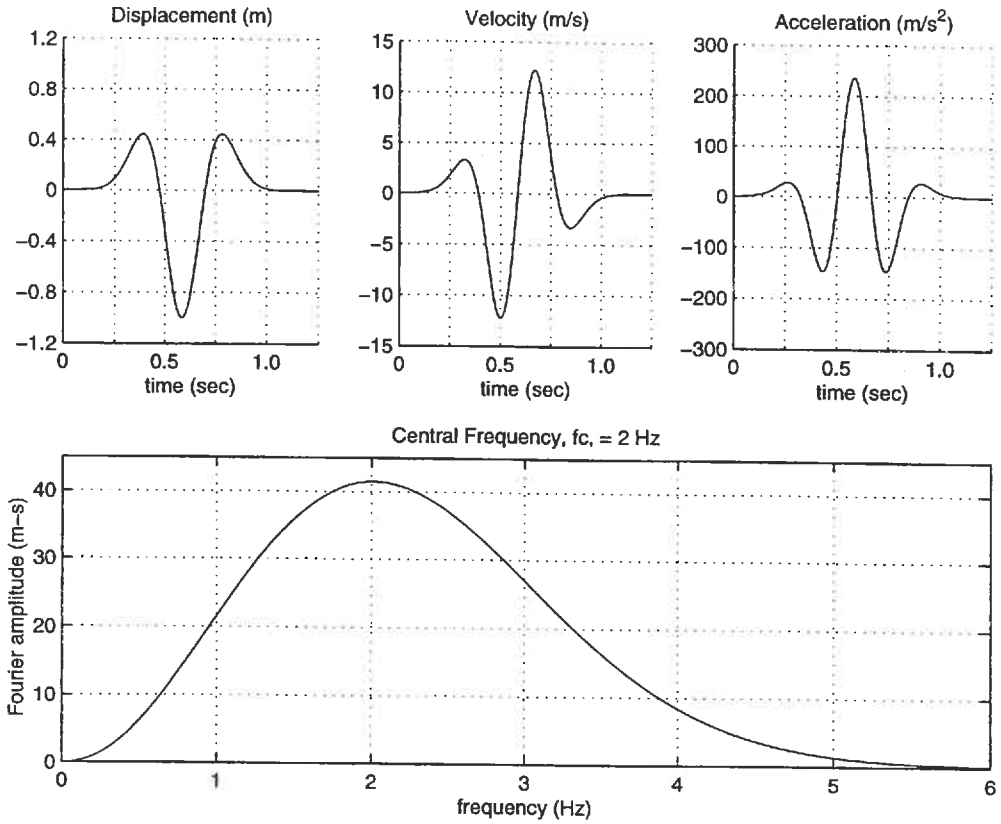

Figure 3.3. (a) Plots of a ricker wavelet in time domain and the corresponding Fourier amplitude spectra of displacement showing the central frequency and distribution of input energy.

The angle of incidence of the input wavelet may be varied throughout 180 degrees from horizontal to vertical. Thus we may model seismic motion coming from sources other than directly below the basin. Two-dimensional simulation cannot model the effects of rupture propagation or forward directivity which were shown to contribute to strong shaking in the 1995 Hyogo-ken Nanbu (Kobe) Earthquake (Pitarka et. al., 1998). We have attempted to account for this by using strong motion records with an element of forward-directivity, although this does not allow for the expected spatial variation of this effect.

Chapter 4: GEOLOGICAL MODELS

Two-dimensional cross-sections of the Lower Hutt Valley and the Wellington (Te Aro) Basin were constructed from existing sub-surface geological data. The cross-sections are used to define the geometry of the finite-element meshes, and along with the material properties are used as input to the calculation procedure. Within the Port Nicholson Basin (which includes both Te Aro Basin and Lower Hutt Valley) there are two separate geologic units of interest. Firstly the greywacke basement rock, and secondly the stratified sediments that have progressively in-filled the deepening depression.

4.1 GEOLOGICAL UNITS OF THE PORT NICHOLSON BASIN

The Wellington area is underlain by Upper Paleozoic to Mesozoic age basement rock of the Torlesse Complex. Interbedded layers of indurated sandstone (greywacke) and mudstone (argillite) were formed in a deep marine environment during a period of subduction at the continental margin. Small areas of basalt, chert, coloured argillite and limestones are also present (Begg and Mazengarb, 1996). The rocks have since been intensely folded and faulted in several directions, and are also closely jointed. Intact bedrock is generally strong to very strong, although the rock mass is weaker due to the 0.1-0.5 m joint spacing, the presence of many sheared zones and weathering near the surface (Dellow et. al., 1992; Grant-Taylor, 1959).

Substantial depths of Quaternary sediments have accumulated in the Port Nicholson basin over the last 450,000 years, since Cook Straight opened (Begg and Mazengarb, 1996). The thickest record of sediments in the Lower Hutt Valley (299m) is from the Gear Meat Drillhole which reaches basement on the Petone foreshore. The sediments within the Lower Hutt-Port Nicholson basin are referred to as the Hutt Formation and were laid down in alluvial, estuarine and marine environments, during a succession of interglacial and glacial periods (Stevens, 1956a,b; Grant-Taylor, 1959).

The most recent (Holocene) sediments were deposited during the current interglacial. Taita Alluvium is the fluviatile veneer over the Hutt Delta and consists of gravels with minor silts and clays with an average depth of 13m, overlying Melling Peat, a thin highly fossiliferous layer. The Petone Marine Beds – silts and clays of some seven metres in thickness bounded below by an impervious aquiclude – complete the 20m+ depth of Holocene sediments.

Dellow et. al. (1992) describes the near-surface Holocene materials above the aquifer as generally soft in nature, fine grained with high water contents and low SPT values ($N<10$). Coarser grained beds and lenses may form up to 40% of the total mass. Shear wave velocities of 175 m/s have been measured in some of these soft sediments (Stephenson and Barker, 1992). Their maximum thickness is 27 m in the lower, western valley, and they gradually thin and grade into the Taita Alluvium gravels up-valley. Only the lower half of the Hutt Valley is underlain by more than 10 m of soft sediments (Dellow et. al., 1992).

Waiwhetu Artesian Gravels originate from the last (Otiran) Glacial and consist of compact sandy gravel to form an aquifer ranging between 30 and 50 metres thick. Many boreholes penetrate into the Waiwhetu aquifer as fresh water supply for the Lower Hutt City. Below the aquifer lie a series of glacial and interglacial units consisting of gravels, sands and silts. Included amongst these are the marine Wilford Shell Beds from the last Interglacial (Kaihinu), and the Moera and Nemona Basal Gravels. Begg and Mazengarb (1996), Dellow et. al. (1992) and Stevens (1956b) all provide more complete descriptions of sediments in the Lower Hutt.

A layer of fill covers small parts of Lower Hutt and much of the Wellington inner city. Seaview, on the eastern side of the lower Hutt River is one such area, along with the Hutt Road up the western side of the valley. In Wellington, much of the city is sited on reclaimed land extending out into the harbour. Most of the central city has been built on more than two metres of fill, the majority of which is poorly compacted. The most commonly used material was weathered rock from nearby quarries, whilst hydraulic fill and demolished brickwork have been used in some areas (Begg and Mazengarb, 1996). These layers of fill have low strength and shear velocities and are likely to liquefy during strong shaking.

4.2 *Lower Hutt Valley Models*

Two lines across the valley were chosen; one through Petone and Seaview at the seaward (south-western) end of the Hutt Valley, and one through Lower Hutt Central and Waiwhetu, 2.45 km up-valley. Both cross-sections were taken along a line running 32 degrees west of north. Cross-sections have been aligned such that the in-plane horizontal (x) coordinate is measured perpendicular to the Wellington Fault, approximately south-east from the north-western edge (rock-soil interface) of the basin. The vertical (y) axis is negative below the ground surface (or mean sea level, in some cases), and the out-of-plane horizontal axis (z) runs fault-parallel down the length of the basin.

Layer	Name and Description (after Begg and Mazengarb, 1996)	S-wave velocity V_s m/s	P-wave velocity V_p m/s	Poisson's ratio ν	Density ρ kg/m^3	Shear modulus $G=\mu$ 10^6N/m^2	Lame's constant λ 10^6 N/m^2	Elastic modulus E 10^6N/m^2
A	Post-European loose rock and hydraulic fill	100	444	0.473	1750	18	309	52
B/Bb	Taita Alluvium, Melling Peat, Petone Marine Beds. Post-Glacial Holocene sands, silts and gravels	175	776	0.473	1750	54	947	158
C	Waiwhetu Artesian Gravels. Last Glacial (Otiran) gravels and sands with some clay	285	1264	0.473	1800	146	2584	431
D1	Last Interglacial (Kaihinu) gravels, sands and silts. Includes Wilford Shell Bed	325	1441	0.473	1850	195	3453	576
D2/3	Glacial (Waimea) and interglacial (Karoro) poorly-consolidated sediments	460	2040	0.473	1900	402	7104	1185
D4/5	Moera Basal Gravels. Glacial (Waimaunga) and interglacial (Brunswick) stiff sediments	600	2661	0.473	1950	702	12405	2068
D6	Nemona Glacial Gravels. Late Quarternary weathered and stiff sediments	675	2994	0.473	2000	911	16102	2685
E	Lithified, fractured basement Greywacke (Torlesse Complex of Upper Paleozoic to Mesozoic age)	1500	3489	0.387	2700	6075	20711	16847

Table 4.1. Geological units in Lower Hutt, with their associated elastic properties used for input data to the FEM simulation.

The total sediment depth and contours of the bedrock-sediment interface are estimated from a gravity survey (Cowan and Hatherton, 1968) with control provided by boreholes (Dellow et. al., 1992). The Institute of Geological and Nuclear Sciences (IGNS) in Wellington provided information from their database of borehole information for the Hutt Valley. Because of the artesian water supply in the Lower Hutt, numerous boreholes and associated logs exist for depths to 30 metres, however deep information is limited to only a few boreholes at the lower end of the valley, only two of which reach bedrock. Borehole data was used to both locate layer

interfaces and determine sediment properties. Geologic cross-sections of the valley were constructed from bedrock contours and borehole logs (N.D. Perrin, pers. comm.).

The highly heterogeneous quaternary soil deposits in the Lower Hutt have been grouped into seven stratigraphic units according to their estimated elastic properties (shear-wave velocity, bulk density and Poisson's ratio, from which all others are derived). The properties of these sedimentary layers and bedrock are given in Table 4.1. Shear wave velocities of the sediments have been estimated based on the Borcherdt method (N.D. Perrin, pers. comm.), which uses data from San Fransico and Los Angeles, and are validated with measured data from unit B (Stephenson and Barker, 1992). Poisson's Ratio and P-wave velocities are inferred from measurements in Wainuiomata (Duggan, 1997). Elastic properties of the basement greywacke have been estimated from measurements in the Wellington Motorway tunnel (Ingham, 1971) and at various other locations in the Wellington area (N.D. Perrin, pers. comm.).

4.2.1 SECTION AA: PETONE

The section chosen through Petone and Seaview crosses the southern end of the valley at its widest point (4.35 km) near the foreshore of the Wellington Harbour. The line intersects a mainly industrial and residential area of Lower Hutt, where buildings are between one and four storeys high. The fault trace and the position of the sub-surface vertical fault wall appear to be approximately 320m out from the western edge, while the Hutt River mouth is located approximately 3 km further east

The geologic cross-section in Figure 4.2(a) was converted to a set of coordinate (x,y) points, between which 70 straight-line segments could be defined to give the approximate interface geometry of the FEM mesh. The final 2-D mesh generated by Archimedes shown in Figure 4.3(a) is some 6.5 km wide by 1 km deep and consists of 37,787 nodes forming 18,256 triangular elements.

4.2.2 *SECTION BB: HUTT CENTRAL*

This second cross-section across the Hutt Valley shown in Figure 4.2(b) was chosen to intersect with the central business district of Lower Hutt (Lower Hutt Central). The Hutt River lies approximately 200m from the western edge, with the fault trace at approximately 160m. Lower Hutt Central contains commercial office blocks, shops and other buildings between one and seven storeys high, while the eastern two-thirds of the section across Waiwhetu is largely single and double-storey residential dwellings.

The sedimentary valley is 3.02 km wide at this point, and the sediment-bedrock interface extends to a maximum depth of 275m. Except for the top soft layer and the artesian gravels, which were plotted from nearby borehole data, layer interfaces have largely been extrapolated up-valley from the Petone cross-section (N.D. Perrin, pers. comm.).

As with the first model, cross-section BB includes no surface topography or elevation, disregarding the hills to either side of the valley. Several of the 40 segments from which the model has been constructed are circular curves, which give a more realistic approximation of interface geometry. The final FEM mesh shown in Figure 4.3(b) is again 6.5 km wide by 1 km deep, and contains 27,676 nodes forming 13,479 elements.

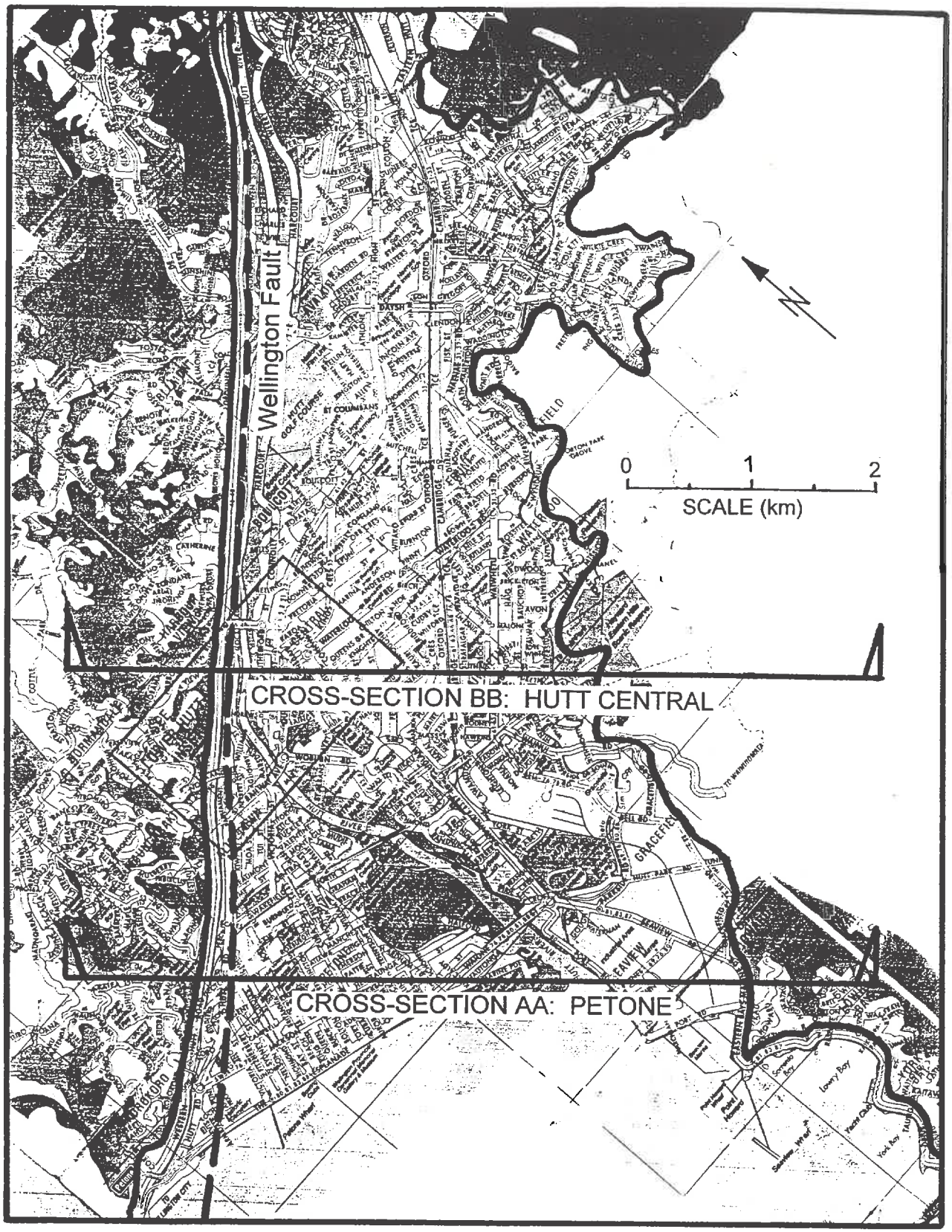

Figure 4.1. Map of the Lower Hutt Valley showing the position and orientation of the two geologic cross-sections. The dark line shows the sediment-bedrock interface at the sides of the valley, while the position of the Wellington Fault running along the northwestern boundary is indicated by a dashed line.

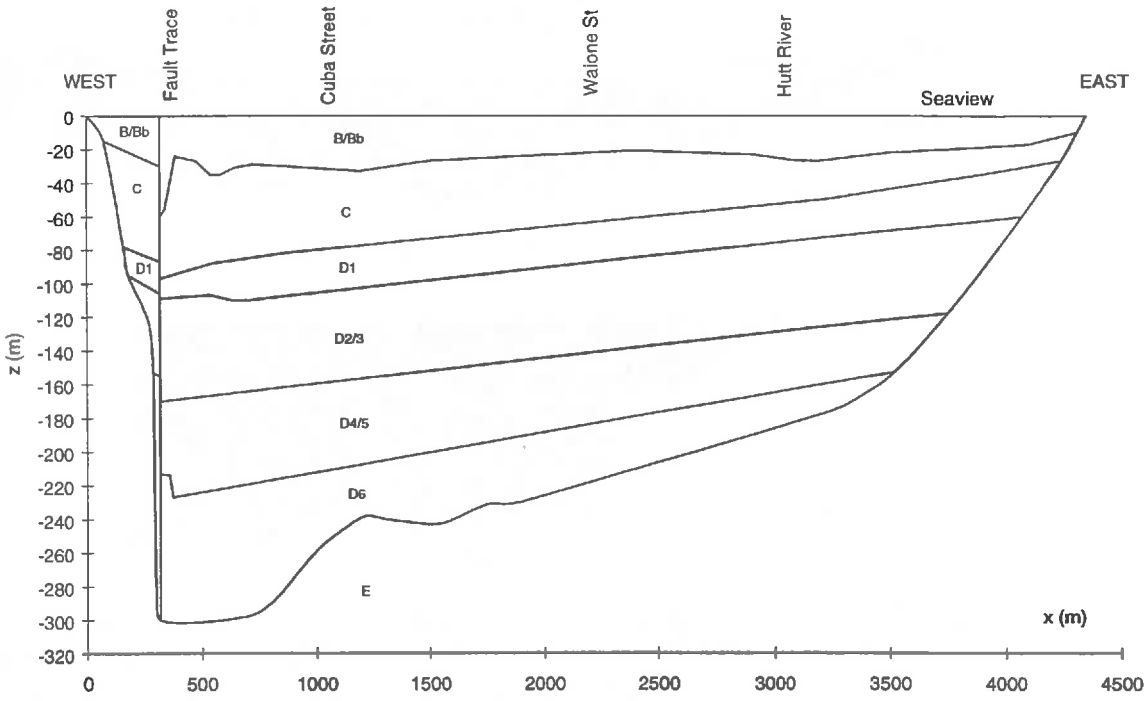

(a)

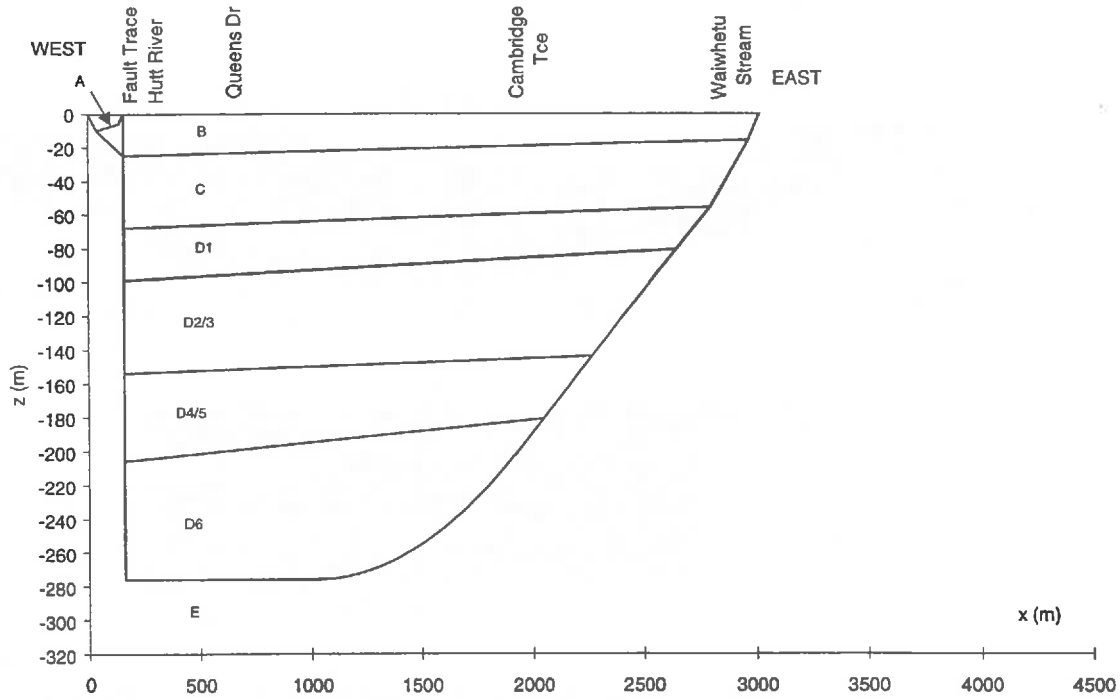

(b)

Figure 4.2. (a) Geologic cross-section AA though Petone at the seaward end of the Hutt Valley and (b) cross-section BB through Lower Hutt Central, some 2.45 km up valley. Note the vertical exaggeration.

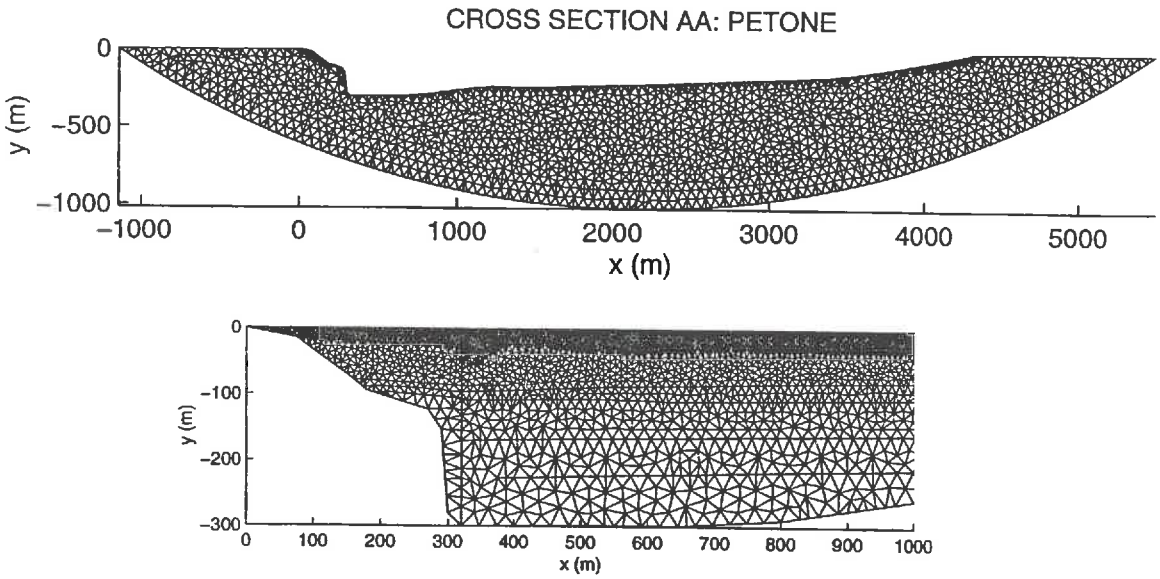

Figure 4.3(a). FEM mesh generated by Triangle, of the Archimedes tool set, for Section AA through PETONE. The top plot shows the full mesh domain (excluding the sedimentary valley), with the semicircular lower boundary and flat top surface. The lower plot shows an enlarged view of the left-hand (fault-bounded) edge of the sedimentary valley, cut from the top plot.

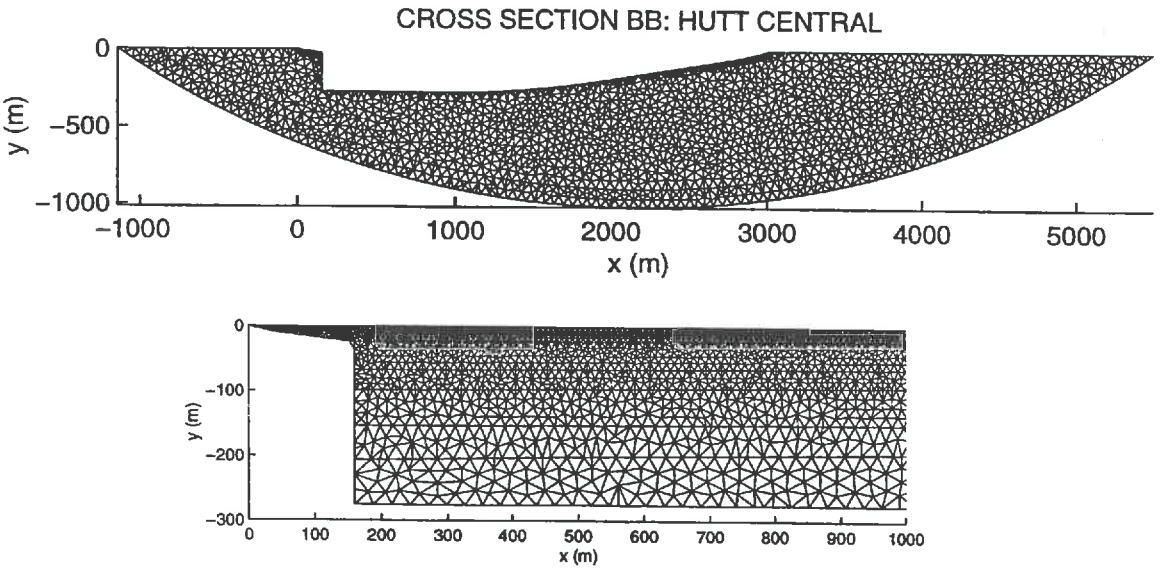

Figure 4.3(b). FEM mesh of Section BB through HUTT CENTRAL. The top plot shows the full mesh domain (excluding the sedimentary valley), with the semicircular lower boundary and flat top surface. The lower plot shows an enlarged view of the left-hand (fault-bounded) edge of the sedimentary valley, cut from the top plot.

4.3 WELLINGTON (TE ARO) BASIN MODEL

Te Aro Basin lies between Kelburn and Mount Victoria, underlying the central business district of Wellington City. It is approximately 1100 m wide and about as long, extending from the Lambton waterfront south to Basin Reserve. A map of Te Aro Basin is shown in Figure 4.4. The sediments reach a maximum depth of 140 m slightly east of centre beneath the National Museum, Te Papa. The basin is not bounded by the Wellington Fault, as with the Hutt Valley, so the bedrock on each side forms a gently sloping interface with the soft sediments. The Wellington Fault runs perpendicular to the basin cross-section some 1100 horizontal metres from its western edge.

Layer	Description	S-wave velocity V_s m/s	P-wave velocity V_p m/s	Poisson's ratio ν	Density ρ kg/m^3	Shear modulus $G=\mu$ 10^6N/m^2	Lame's constant λ 10^6N/m^2	Elastic modulus E 10^6N/m^2
A	Post-European loose rock and hydraulic fill	100	444	0.473	1800	18	318.1	53
B/C	Post-glacial soft silts, sands and gravels	150	665	0.473	1800	41	715.7	119
D1	Pleistocene stiff sediments. Gravels with silts and clays.	250	1109	0.473	2050	128	2264.1	378
D2		300	1331	0.473	2098	189	3336.6	556
D3		500	2218	0.473	2098	525	9268.3	1545
E	Lithified, fractured basement greywacke (Torlesse Complex of Upper Paleozoic to Mesozoic age)	1200	2791	0.387	2700	3888	13254.9	10782

Table 4.2. Material properties of geologic units in Te Aro Basin.

4.3.1 SECTION CC: TE ARO

Te Aro cross-section CC in Figure 4.5 cuts across the open northern end of the basin, passing along Cable Street and through downtown Wellington. Te Aro Basin contains a very similar set of sediments to the Hutt Valley. They have been grouped into five sedimentary units as shown in Table 4.2. Shear-wave velocities have been estimated from SPT tests (Perrin and Campbell, 1992; Millar, 1991). Contours of the outcropping hills to either side of the valley are taken from published topographical data (DOSLI, 1996).

The FEM mesh of Te Aro Basin includes the hills for 600m to either side, as well as the variable elevation of the centrally dipping sediment surface. It is constructed from 40 linear segments with a domain 2.4 km wide by 450 m deep. The final triangular mesh (Figure 4.6) generated by Archimedes contains 6,955 nodes forming 3,274 elements.

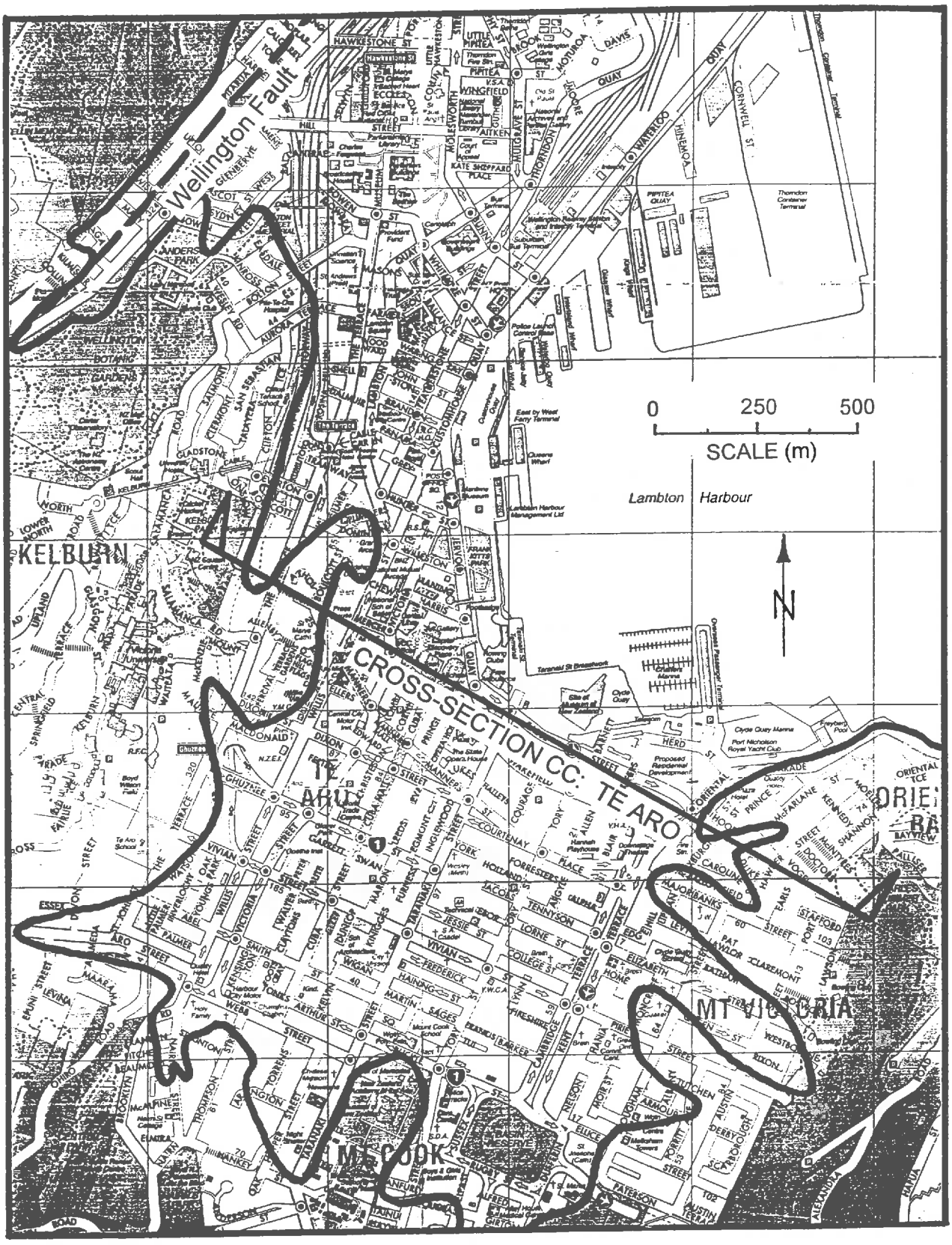

Figure 4.4. Map of Wellington showing the position and orientation of cross-section CC: Te Aro. The dark line shows the bedrock-sediment interface around the periphery of the basin. The Wellington Fault runs perpendicular to the cross-section some 1.1 km northwest.

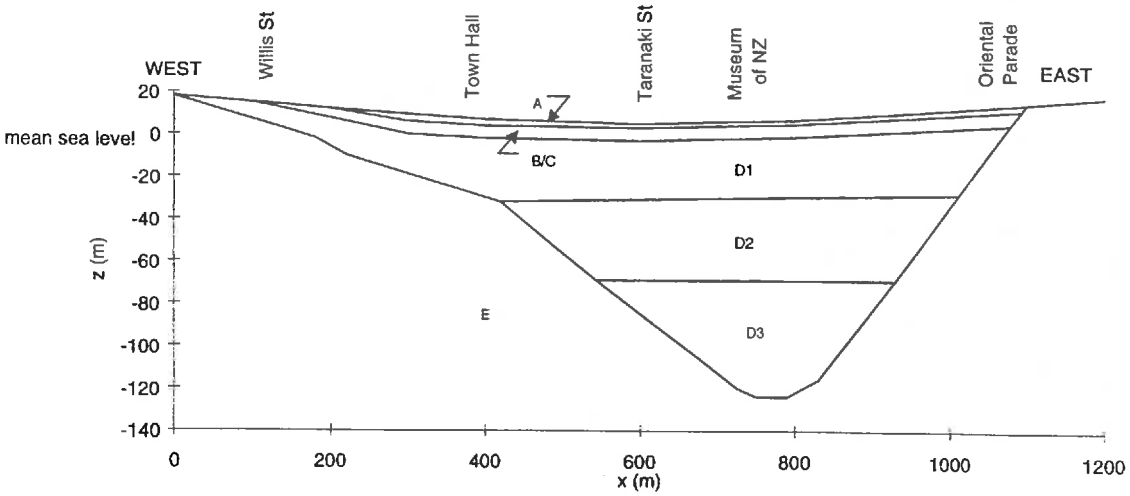

Figure 4.5. Geological cross-section through Te Aro Basin in downtown Wellington. Note the vertical exaggeration.

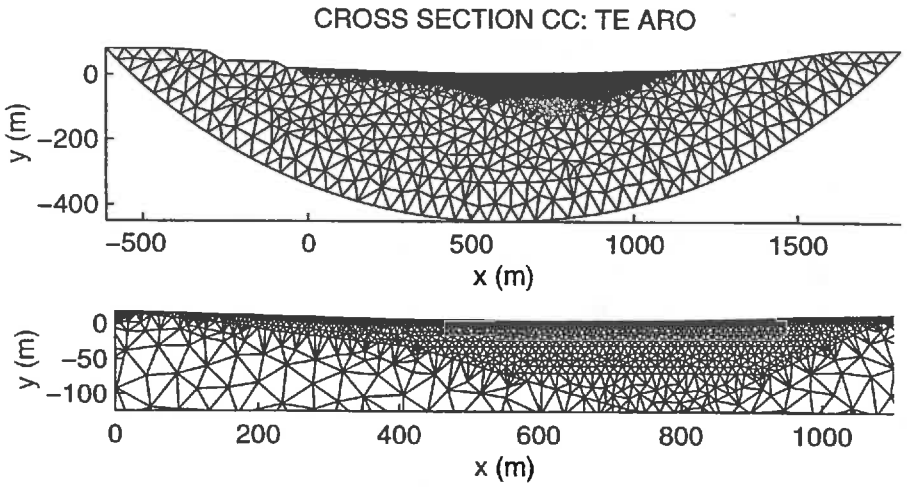

Figure 4.6. FEM mesh generated by Triangle of the Archimedes tool set. An enlargement of the basin shows more detail.

Chapter 5: DATA PROCESSING METHODS

Data from Archimedes was handled with the technical computation, graphing and programming application MATLAB version 5.1 in both UNIX and Windows operating systems. MATLAB was used for plotting, numerical integration, Fourier analysis and other general manipulation of the data.

5.1 Output Data

The Archimedes simulation was set up to generate output in the form of ASCII data files. For each iteration, displacement and acceleration data were captured from an evenly spaced set of nodes on the ground surface. In the Hutt Valley at Petone, 303 nodes were captured, each approximately 20 metres apart, while for Te-Aro Basin in Wellington, 140 nodes at approximately 10 metre spacing were used. Each line of output also included, for reference, the node coordinate and number and the iteration number. Most simulations were continued up to 4000 iterations to obtain 20 seconds of information. Thus output files would be in the order of 10^6 lines long, and 10-20 Megabytes in size.

5.2 Time-Domain Seismograms

The captured data allowed for direct plotting of displacement and acceleration seismograms for each node. Numerical integration of the acceleration trace also gave velocity seismograms. Each seismogram represents the transient soil response at a discrete location on the ground surface due to a single input Ricker pulse. The seismograms were plotted close together on a position-time axis to give, in effect, a single continuous space-time seismogram for the ground surface of each model. Amplitude is shown as a colour scale. Using this technique, position-time paths of surface waves can be clearly seen.

5.3 FOURIER FREQUENCY ANALYSIS

Fourier techniques were used to convert time-domain data (acceleration, velocity and displacement records) into the frequency-domain for the generation of transfer functions, Fourier spectral ratios, real-time earthquake records and response spectra. The radix-2 fast Fourier transform algorithm built into the MATLAB function library (Mathworks, 1997) was found to be the most convenient method. Time sequences of 4000 points were typically padded with trailing zeros to a length, N, of 2^{14} (16384) in order to give sufficient accuracy in the frequency-domain. A time-step, Δt, of 0.005 seconds in the time-history record produces a frequency-step, Δf, of $1/(N\Delta t) = 1/(2^{14} \times 0.005) = 0.0122$ hertz on the frequency plot; and permits the frequency response up to the Nyquist critical frequency, $f_{Nyquist}$, of $1/(2\Delta t) = 1/(2 \times 0.005) = 100$ hertz.

Each term of the discrete Fourier transformed sequence is a complex variable, $z = x + iy$, (with real and imaginary parts) containing both amplitude and phase information. The Fourier amplitude spectrum, FAS, is given by the magnitude (modulus) of each complex term.

$$FAS = |F(i\omega)| = \sqrt{z \times z^*} \qquad [5.1]$$

Here, $i\omega$ is used to indicate a complex sequence in frequency domain and z^* is the complex conjugate of z. The Fourier phase spectrum, $\phi(\omega)$, is given by the angle

$$\phi(\omega) = \tan^{-1}\left(\frac{\mathrm{Im}(z)}{\mathrm{Re}(z)}\right) \qquad [5.2]$$

5.3.1 TRANSFER FUNCTION

The Fourier transform of the output seismogram at the soil surface $F_{o,surface}(i\omega)$ was normalised against the Fourier transform of the input bedrock motion, $F_{i,bedrock}(i\omega)$, to give a transfer function, $H(i\omega)$, for the soil at each location. Thus the transfer function

is defined[1] as the *ratio of the Fourier transform of the acceleration (or displacement, etc) time-history at the ground surface to that of a simultaneous time-history in the sub-surface bedrock.* It is obtained by division of the two complex spectra.

$$H(i\omega)=\frac{F_{o,surface}(i\omega)}{F_{i,bedrock}(i\omega)} \qquad [5.3]$$

The transfer function is also complex. Its modulus, $|H(i\omega)|$, is the ratio of the ground and bedrock Fourier amplitudes, and its phase angle, $\phi(\omega)$, is the difference between phase angles of the ground and bedrock. It gives a complete description of how the sub-surface sedimentary layers and other local geology affect the magnitude and phase of incoming seismic waves; and is used primarily to compute realistic time-history records, as described below.

5.3.2 FOURIER SPECTRAL RATIO

Closely related to the transfer function is the Fourier spectral ratio (FSR), first used by Borcherdt (1970). The FSR is the ratio of the Fourier amplitude from a recording on the *soil surface* to the Fourier amplitude from a simultaneous recording on a *bedrock outcrop*.

$$FSR(\omega)=\frac{\left|F_{soil\ surface}(i\omega)\right|}{\left|F_{rock\ outcrop}(i\omega)\right|} \qquad [5.4]$$

All phase information is lost in the calculation of the FSR. For the case of a uniform half-space of perfectly elastic rock, the outcrop surface motion (ie. the output from the simulation) is expected to have twice the amplitude of the bedrock basement motion (ie. the input to the simulation). The actual response from the computer simulations was slightly erratic, although of similar amplitude and shape to the ideal. Thus to obtain a smoother FSR from model results, it is calculated directly from the modulus of the transfer function.

---

[1] *It should be noted that the general definition of a transfer function is simply the ratio of one parameter to another. In seismology it is sometimes defined as the ratio of the response of ground motion and rock-outcrop motion (similar to the Fourier spectral ratio), or the ratio of motion at any point in the soil column to motion in the bedrock. Here we use the most common definition: the ratio of surface to bedrock motion.*

$$FSR(\omega) = \frac{\left|F_{o,surface}(i\omega)\right|}{2\left|F_{i,bedrock}(i\omega)\right|}$$
$$FSR(\omega) = \frac{1}{2}\left|H(i\omega)\right| \qquad [5.5]$$

FSR at each evenly spaced position across the valley can also be plotted close together in a similar fashion to the seismograms, with amplitude shown as a colour scale. These plots show clearly patterns of amplification as a function of position and frequency.

5.4 *Artificial Earthquake Motions*

To obtain an idea of the actual response of the ground surface in a real earthquake, we can multiply a record of real bedrock motion, $F_{i,eq}(i\omega)$, by the transfer function to get an estimate of the Fourier spectrum for our model, $F_{o,model}(i\omega)$, under a real excitation

$$F_{i,Model}(i\omega) = H(i\omega) \times F_{i,eq}(i\omega) \qquad [5.6]$$

The transfer function effectively acts as a numerical filter on the real earthquake Fourier transform to give a Fourier transform for the motion in the soil at the ground surface. A time-domain response can then be found by calculating the inverse fast Fourier transform of the sequence. Again the MATLAB radix-2 algorithm is used. The time-domain response is effectively a real-valued sequence, yet small imaginary parts exist due to calculation error and are ignored.

5.4.1 Earthquake Basement Records

A seismogram record from the Kobe University site during the Hyogo-ken Nanbu earthquake of 17 January 1995 is used as a basement input. The Kobe University (KBU) site is located on dense gravel near a rock outcrop, and is considered to be located above the source area. A maximum horizontal velocity of 55.1 cm/s was recorded in the north-south direction, with corresponding maximum accelerations and displacements of 269.8 cm/s and 14.9 cm (Toki et. al., 1995). The Kobe University record with its associated Fourier amplitude spectrum (FAS) is shown in Figure 5.1.

The Hyogo-ken Nambu earthquake had a Richter magnitude of 7.2, a surface wave magnitude of 6.9 and a moment magnitude of 6.8 (Byrne et. al., 1996) to 6.9 (Park et. al., 1995). The hypocentre was located at a depth of 14 km, just west of downtown Kobe, and the bilateral rupture propagated in the southwest and northeast directions on the Suma and Nojima faults. The fault mechanism was primarily right lateral strike-slip with a smaller thrust component, producing 11 km of exposed fault rupture on the Nojima fault. The average movement was 1.0-1.5 m horizontally and 0.3 m vertical.

The KBU north-south acceleration data is corrected for baseline, high-frequency and low-frequency errors by a method based somewhat on that used at the California Institute of Technology for the routine computer processing of strong-motion accelerograms (Trifunac and Lee, 1973; Caltech, 1971; Trifunac, 1970). Essentially, the baseline error is corrected for with successive least squares regression and integration to give velocity and displacement traces. The record is then put through a 0.05 Hz high-pass and a 6.5 Hz low-pass Ormsby filter.

The weights for the Ormsby filter window of length $T_W = N\Delta t$ with the time coordinate $t_n = n\Delta t$ are given by (Trifunac, 1970)

$$w_N(n) = \frac{\cos 2\pi n\lambda_C - \cos 2\pi n\lambda_T}{2\lambda_R(\pi n)^2} \qquad n = 0,\pm1,\pm2,\pm3,\ldots,\pm N \qquad [5.7]$$

where $\lambda_C = f_C\Delta t$, $\lambda_T = f_T\Delta t$, $\lambda_R = (f_T - f_C)\Delta t$, f_C is the cut-off frequency and f_T is the roll-off termination frequency. For $N\rightarrow\infty$, the complex filter, $H(if)$, approaches the ideal given by

$$\hat{H}(if) = \begin{cases} 1 & f \le f_C \\ \dfrac{f_T - f}{f_T - f_C} & f_C \le f \le f_T \\ 0 & f > f_T \end{cases} \qquad [5.8]$$

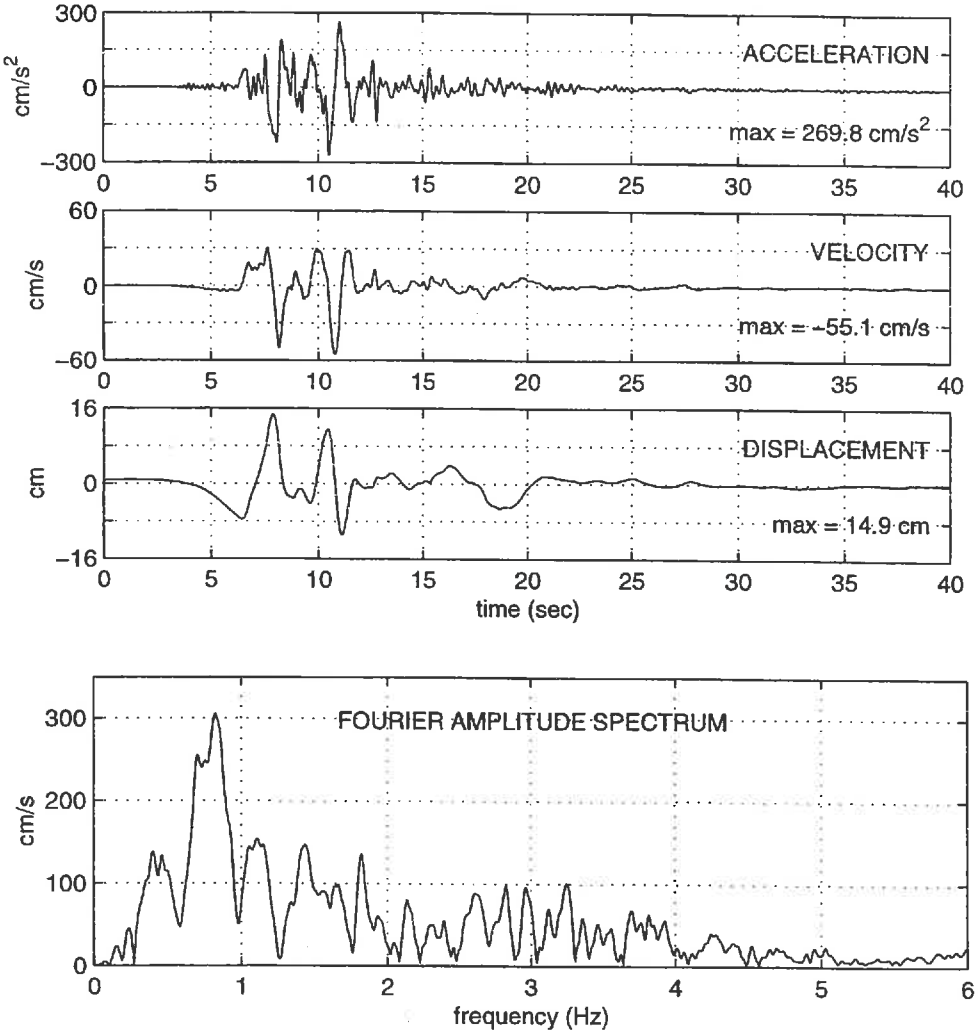

Figure 5.1. Kobe University (KBU) north-south record (Toki et. al., 1995; Toshinawa, 1998). Velocity and displacement traces have been integrated from the acceleration record with baseline correction and digital bandpass filtering between 0.05 and 6.5 Hz)

Berrill (1996) has computed a design velocity spectrum for the Parliament buildings in Wellington, using a set of scaled near-field strong motion records from around the world. The design Psuedo-velocity response spectrum (PSV) for 5% structural damping is shown in Figure 5.2, on top of the KBU 5% PSV. Also shown is a spectrum derived from the New Zealand Loadings Code, NZS4203 (Standards New Zealand, 1992) for elastic response (μ = 1). The KBU record lies below the design response for short-period excitation. The agreement is good at periods around 1.0 seconds, yet the KBU response drops off again at higher periods. The Kobe earthquake had a slightly lower magnitude (M_S 6.9) than what we might expect from a Wellington fault rupture (M_S 7.1-7.8), yet it is similar in mechanism.

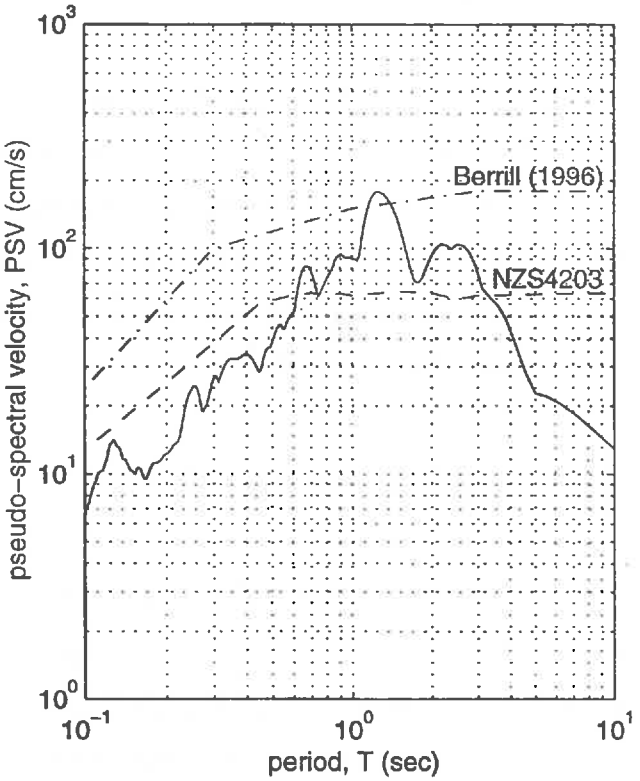

Figure 5.2. Pseudo-spectral velocity 5% damped response for the Kobe University north-south record. Also shown is a design velocity spectrum (5% damping) for Wellington (Berrill, 1996) and the NZS4203 Loadings Code spectrum (Standards New Zealand, 1992).

Generally the actual bedrock motion from most earthquakes is unknown. We estimate the bedrock motion to be half that of the motion on a rock outcrop at the surface by assuming elastic behaviour of the rock and the absence of topographical effects.

5.4.2 Filtering of Transfer Functions and Artificial Records

Transfer functions are initially filtered above 5.5 Hz and below 0.25 Hz to remove noise generated by the Archimedes FEM process. They are then suitable to use for the calculation of artificial records within the basin. Artificial records are corrected for low frequency errors by a method similar to that used on the KBU data using a high-pass Ormsby filter of 0.25 Hz.

5.5 *RESPONSE SPECTRA*

Response spectra techniques describe the response of a single-degree-of-freedom (SDOF), viscously damped, linear oscillator to an earthquake excitation. They act as a narrow band-pass filter on the record to smooth the frequency response. Spectra are drawn by computing the maximum response of a SDOF oscillator of given natural frequency under an earthquake base excitation. The time-history is found by solving the equation of motion for an SDOF oscillator

$$\ddot{x}+2\omega\zeta\dot{x}+\omega^2 x=-a(t) \qquad [5.7]$$

where x is the relative motion of the oscillator, ω is the natural frequency of the oscillator in radians per second, ζ is the damping ratio and $a(t)$ it the ground acceleration. Here we use an efficient exact analytical solution to this equation first published by Nigam and Jennings (1969). The method has since been used most notably in the processing of strong motion records at Caltech (1972), and has been refined by Gupta (1990). Given a time-history approximated as a discrete valued function, the equation of motion is rewritten as

$$\ddot{x}+2\omega\zeta\dot{x}+\omega^2 x=-a_i+\frac{\Delta a_i}{\Delta t}(t-t_i) \qquad t_i\le t\le t_{i+1} \qquad [5.8]$$

where the time step $\Delta t=t_{i+1}-t_i$, and $\Delta a_i=a_{i+1}-a_i$. The solution to the relative displacement and velocity at the end of each time step may be expressed in a recursive matrix form as

$$\begin{Bmatrix} x_{i+1} \\ \dot{x}_{i+1} \end{Bmatrix}=[A(\zeta,\omega,\Delta t)]\begin{Bmatrix} x_i \\ \dot{x}_i \end{Bmatrix}+[B(\zeta,\omega,\Delta t)]\begin{Bmatrix} a_i \\ a_{i+1} \end{Bmatrix} \qquad [5.9a]$$

$$\text{where}\quad A=\begin{bmatrix} a_{11} & a_{12} \\ a_{21} & a_{22} \end{bmatrix}, \qquad B=\begin{bmatrix} b_{11} & b_{12} \\ b_{21} & b_{22} \end{bmatrix} \qquad [5.9b]$$

The coefficients of [*A*] and [*B*] are

$$
\begin{aligned}
a_{11} &= e^{-\zeta\omega\Delta t_i}\left(\frac{\zeta}{\sqrt{1-\zeta^2}}\sin\omega_d\Delta t_i + \cos\omega_d\Delta t_i\right)\\
a_{12} &= \frac{e^{-\zeta\omega\Delta t_i}}{\omega_d}\sin\omega_d\Delta t_i\\
a_{21} &= -\frac{\omega}{\sqrt{1-\zeta^2}}e^{-\zeta\omega\Delta t_i}\sin\omega_d\Delta t_i\\
a_{22} &= e^{-\zeta\omega\Delta t_i}\left(\cos\omega_d\Delta t_i - \frac{\zeta}{\sqrt{1-\zeta^2}}\sin\omega_d\Delta t_i\right)
\end{aligned}
\qquad [5.9c]
$$

and

$$
\begin{aligned}
b_{11} &= e^{-\zeta\omega\Delta t_i}\left[\left(\frac{2\zeta^2-1}{\omega^2\Delta t_i}+\frac{\zeta}{\omega}\right)\frac{\sin\omega_d\Delta t_i}{\omega_d}+\left(\frac{2\zeta}{\omega^3\Delta t_i}+\frac{1}{\omega^2}\right)\cos\omega_d\Delta t_i\right]-\frac{2\zeta}{\omega^3\Delta t_i}\\
b_{12} &= -e^{-\zeta\omega\Delta t_i}\left[\left(\frac{2\zeta^2-1}{\omega^2\Delta t_i}\right)\frac{\sin\omega_d\Delta t_i}{\omega_d}+\left(\frac{2\zeta}{\omega^3\Delta t_i}\right)\cos\omega_d\Delta t_i\right]+\frac{2\zeta}{\omega^3\Delta t_i}-\frac{1}{\omega^2}\\
b_{21} &= e^{-\zeta\omega\Delta t_i}\left[\begin{array}{l}\left(\frac{2\zeta^2-1}{\omega^2\Delta t_i}+\frac{\zeta}{\omega}\right)\left(\cos\omega_d\Delta t_i-\frac{\zeta}{\sqrt{1-\zeta^2}}\sin\omega_d\Delta t_i\right)\\ \quad -\left(\frac{2\zeta}{\omega^3\Delta t_i}+\frac{1}{\omega^2}\right)\left(\omega_d\sin\omega_d\Delta t_i+\zeta\omega\cos\omega_d\Delta t_i\right)\end{array}\right]+\frac{1}{\omega^2\Delta t_i}\\
b_{22} &= -b_{21}-a_{12}
\end{aligned}
\qquad [5.9d]
$$

Thus the displacement and velocity time-history of the SDOF oscillator is calculated by a step-by-step application of equation [5.9]. The procedure is repeated for a range of oscillators, each with a different natural frequency. The maximum displacement of each oscillator is found in order to plot a single point on the spectral displacement (SD) curve. Pseudo-spectral velocity (PSV) and pseudo-spectral acceleration (PSA) curves can then easily be calculated for each level of structural damping.

$$SD(\omega,\zeta) = |x(t,\omega,\zeta)|_{max}$$
$$PSV(\omega,\zeta) = \omega SD \qquad [5.10a,b,c]$$
$$PSA(\omega,\zeta) = \omega^2 SD$$

Pseudo-acceleration spectra for 5% structural damping have been calculated at various positions across the valley.

Chapter 6: RESULTS

This section provides a description of the results captured at the surface of each cross-section after input Ricker waves have been transmitted through the FEM mesh. The transient response of each basin due to an incident Ricker wavelet is first described in the time-domain, where the waves can be visualised as they bounce around within the basin. We then look at results in the frequency domain, which allows the observation of resonant behaviour in the sediments and the associated surface amplification. Finally, we present realistic transient soil responses for each basin based on the Kobe University record from the 1995 Hyogo-ken-Nanbu earthquake.

6.1 LOWER HUTT VALLEY

Both the Petone and Hutt Central cross-sections through the Lower Hutt Valley yielded somewhat similar results. Throughout this section we will look at the results of the two models side-by-side in order to make comparisons and gauge a general picture of the valley as a whole.

6.1.1 TIME-DOMAIN RESPONSE

A set of displacement seismograms plotted at various positions across each model is shown in Figure 6.1. The Ricker pulse arrives first at the surface in the rock where free-surface doubling gives a peak displacement of approximately twice the input. Softer sediments in the valley delay the arrival of the Ricker pulse and amplify both the duration and intensity of shaking.

On the space-time seismograms (see section 5.2) in Figure 6.2 we see three distinct locations where ground motions are highly amplified; the first two being close to each edge, and the third a few hundred metres in from the valley's western side. The latter is the site of the largest displacement (see Figure 6.1, position *c*), and occurs in both sections during the initial arrival of the ricker pulse. Further results will identify this as the Basin Edge Effect (Kawase, 1996a), while peaks at the valley edges appear to be caused by a

slightly different phenomenon. Each model shows a slightly different response and will be described separately.

Cross-Section AA: Petone

The space-time seismogram in Figure 6.2a clearly shows dispersive surface waves propagating in from each edge of the basin once the direct Ricker-pulse arrives through the rock. On the western side of the Petone cross-section, the surface wave appears to originate from a point some 80 metres in from the edge, where the surface layer [B] is 15 metres deep, and the bedrock dip angle increases from 11° to 37°. It has a group velocity of 175 metres per second, calculated from the slope of a line joining the highest displacements, the energy centroid of the wave train. The phase velocity is measured from the slope of the wave peaks that peel off the front of the wave train at approximately 300 m/s. These peaks tend to both increase in speed and decrease in amplitude as they travel away from the train.

On the eastern edge, two surface waves of differing velocity appear to originate from the point at which the bedrock reaches ground level. The slower wave is of similar characteristics to that refracted from the east, while the faster edge-wave has a group velocity of 240 m/s, and a phase velocity of 520 m/s. This faster edge-wave may be associated with the second layer [C] in the soil column.

The first vertical reflection of the incident SH wave from the basin floor can be seen approximately one second after the first arrival. Note the displacement trace of this wave has been inverted (turned upside-down) during the reflection process. Further vertical reflection cannot be clearly identified in the seismogram record amongst the myriad of interfering troughs and peaks.

Figure 6.3a shows plots of maximum displacement, velocity and acceleration on each surface seismogram against across-valley position. Large displacement peaks at x = 100m and x = 4150m (100m in from each edge) appear to be caused by simple 1-D vertical resonance of the top layer [B].

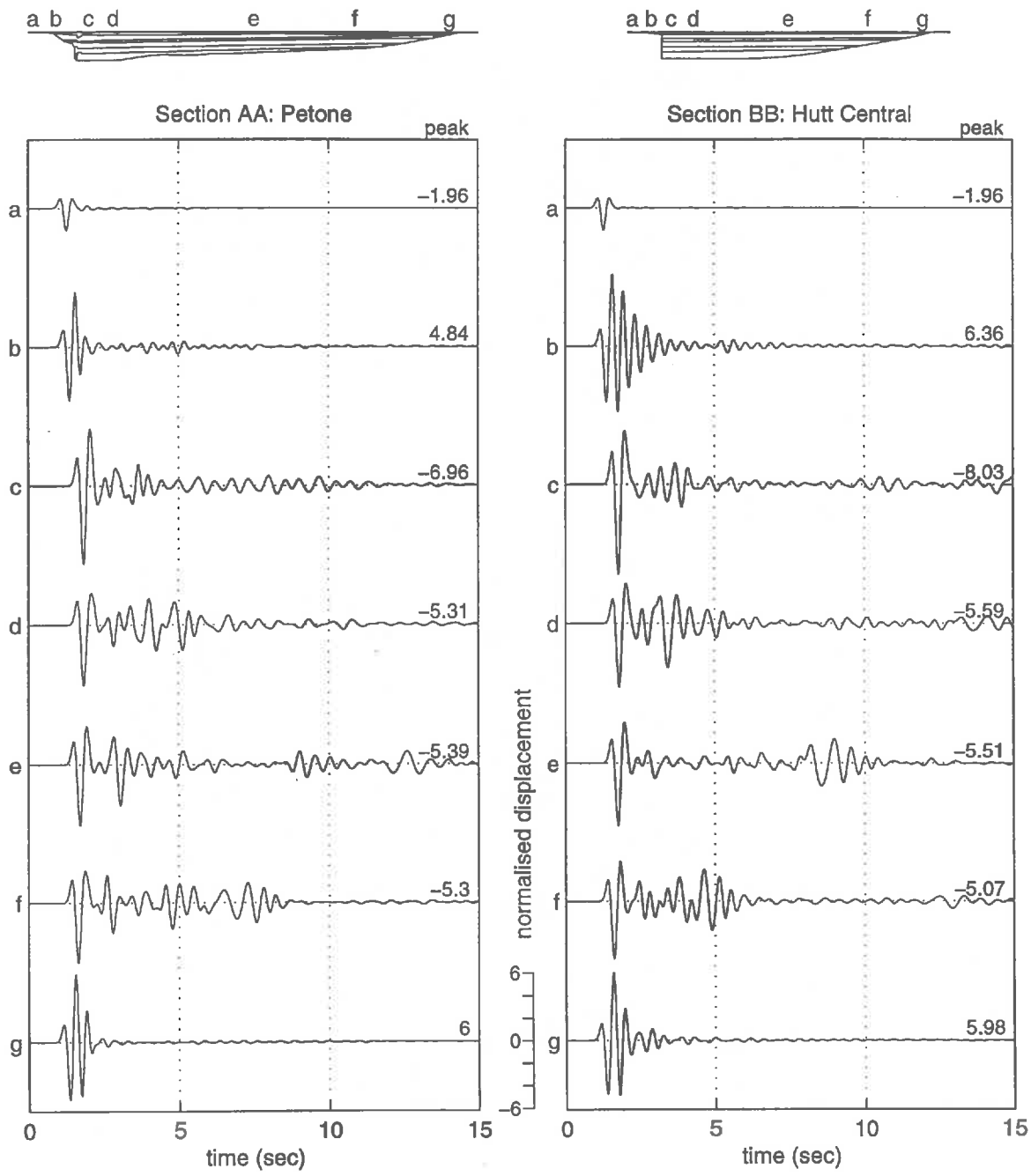

Figure 6.1. Displacement seismograms plotted at intervals across the surface of both cross-sections. Position [a] is located on outcropping rock to the side of the valley. Positions [b] to [g] are located above soft soils within the basin.

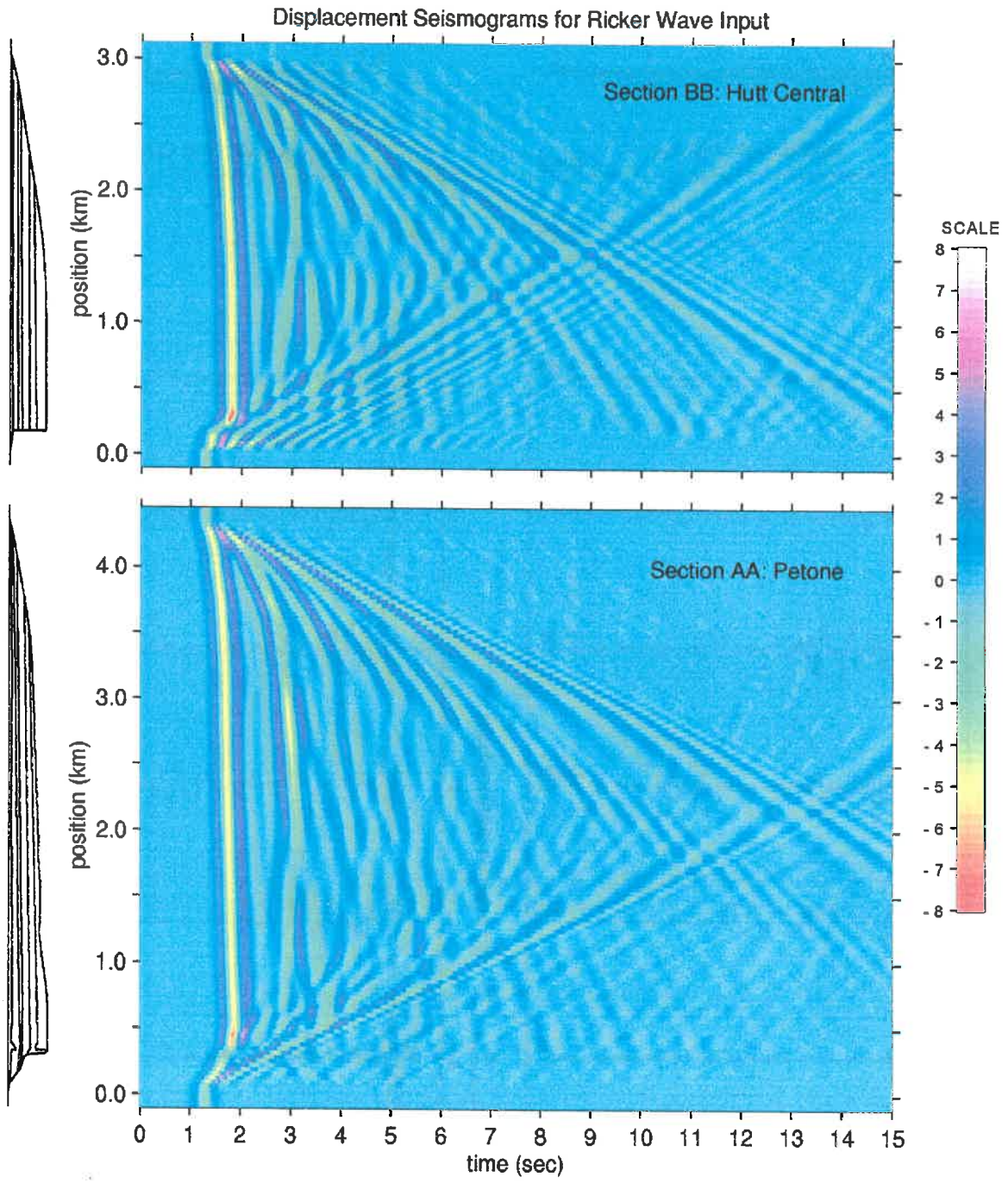

Figure 6.2. Space-time seismograms showing a continuum of transient displacement data across the entire surface of each cross-section. Amplitude is shown as a colour scale (white positive, red negative).

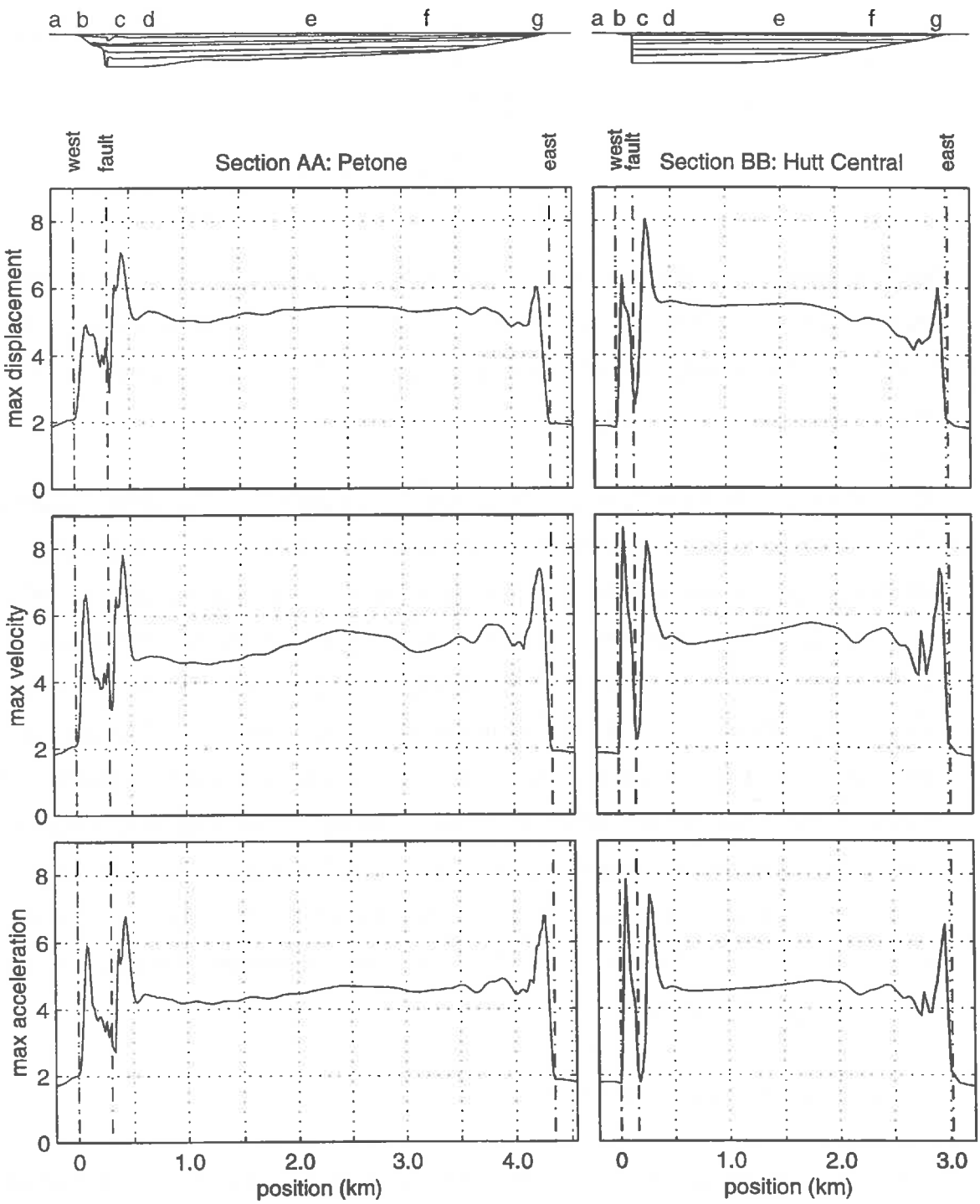

Figure 6.3. Plots of maximum displacement, velocity and acceleration versus across-valley position for each Lower Hutt cross section. Amplitude has been normalised against the maximum displacement, velocity and acceleration associated with the input Ricker wavelet (see section 3.2.4).

This is validated by an application of equation [2.2] which predicts correctly the fundamental natural period of the layer, T_1, the time between vertically reflected waves at the surface, measured from the plot.

$$T_1 = \frac{1}{f_1} = \frac{4H}{V_S} \qquad [6.1]$$

$$T_1 = \frac{4(15m)}{175m/s} = 0.34s$$

Vertical resonance in this top layer appears also to produce a horizontally propagating edge wave refracted from the bedrock interface at x = 80m, every 0.34 seconds. The first of these is not suprisingly the strongest. They appear to have a velocity of some 230-240 m/s.

The basin-edge effect can be seen in Figures 6.1, 6.2a and 6.3a as the displacement peak 440 metres in from the western edge, or 140 metres east of the deep vertical wall forming the valley edge (position *c* in Fig 6.1). The peak extends from approximately x = 350 to x = 515m. The effect of the sloping bedrock interface has complicated the phenomena and made it difficult to distinguish the horizontally propagating edge waves from the first arrival of the SH wave through the sediments. If we are to assume, as it appears on first glance, that the causal edge wave is refracted from x = 80m, it would be required to travel horizontally at some 730 m/s, much faster than expected. We are thus lead to hypothesise that the initial disturbance between x = 0 to x = 370m is the first arrival of the SH wave, and that the causal edge wave propagates horizontally through a deeper layer (eg. layer [C]) of higher shear velocity, being refracted from the bedrock boundary at a point correspondingly further east.

Cross-Section BB: Hutt Central

The response of cross-section BB, this time through the Lower Hutt Central, 2.45 km up-valley, is quite similar to Petone. Again, an edge-wave is refracted from both sides. The wave from the eastern edge has a group velocity of approximately 175 m/s, and has two identifiable phase velocities of 240 m/s and 470 m/s. From the western edge the group velocity is difficult to recognise, although we see a number of peaks of phase velocity 240

m/s being refracted into the basin at regular intervals, 0.4 seconds apart. The first seven of these can be identified and appear to originate from x = 40 m, below layer [A].

It is speculated that this regular output of edge waves is caused by the same phenomena causing the high displacement near the edges at x = 50m and x = 2930m in Figure 6.3b. Namely 1-D vertical resonance, this time most strongly in the softer layer [A] on the western edge. The fundamental natural period can again validated by equation [7.1]. Layer [A] is 10 m deep with an approximate shear velocity of 100 m/s.

$$T_1 = \frac{4(10m)}{100m/s} = 0.40s$$

The other peak in Figure 6.3b can again be attributed to the basin edge effect. Here occurring at x = 120-370 m or 100 m from the deep vertical edge of the valley. With a much simpler stratigraphy compared to the previous cross-section, we can see the edge-wave propagate away from the vertical edge of the basin at approximately 240 m/s. The speed indicating that it is travelling near the B-C interface, 25 metres below the surface.

6.1.2 FREQUENCY-DOMAIN RESPONSE

A set of Fourier spectral ratios have been plotted at intervals across the valley in Figure 6.4. At position [a], on outcropping bedrock, the FSR is approximately unity, as expected. On the edges of both models in positions [b] and [g], we see a reasonably smooth peak of energy in the 2.5 to 3.0 Hz range. The FSR plots at positions [c] to [f] show a vast number of low frequency peaks below 2.5 Hz.

Turning to the space-frequency plots (see section 6.4) of FSR in Figure 6.5, we see in both models that the complex pattern of low frequency spikes is one of 2-D amplification. Curving extremum lines of amplified motions – as expected from analytical theory described in section 2.2.2 – are prominent features. Amplification within any given vertical mode set (eg. for m=1, n=1,2,3,...) appears to be strongly correlated with the extremum lines, rather than particular eigenfrequencies. At least the first 4-5 vertical (m = 1,2,3,4,5) modes, each with a corresponding set of horizontal (n = 1,2,3,...) modes can be recognised, the eigenfrequencies of which have been listed in Table 6.1.

The 2-D resonance pattern causes widespread amplification across the valley roughly within the range 0.4 to 3.5 Hz. The amplification is highly variable in both the spatial and frequency dimensions. A 300m change in position might shift the FSR from unity to 14, as could a 0.1 Hz change in input frequency. Amplifications of the order of 8 to 12 occur only within the band 0.5-2.5 Hz.

f_{mn} (Hz)		Section AA: Petone Vertical Mode (m)				Section BB: Hutt Central Vertical Mode (m)			
		1	2	3	4	1	2	3	4
Horizontal Mode (n)	1	0.45	1.10	1.65	2.15	0.49	1.15	1.80	2.50
	2	0.52				0.58			
	3	0.59				0.67			
	4	0.65				0.75			
	5	0.70				0.83			
	6	0.75				0.90			
	7	0.80				0.97			
	8	0.85				1.04			
	9	0.89				1.11			
	10	0.94				1.18			
	11	0.99				1.25			
	12	1.04				1.31			
	13	1.08				1.37			
	14					1.43			
	15					1.49			

Table 6.1. Identifiable eigenfrequencies from figure 6.5. Blank spaces indicate modes that do not cause significant amplification

On the whole, eigenfrequencies of section BB are 5 to 20% higher than those of section AA. Referring to equation [2.3], this observation is supported in that f_{mn} is higher for shallower basins with higher depth to width (H/L) ratios.

Cross-Section AA: Petone

Referring to Figure 6.5a and Table 6.1, the peak and trough locations of the first 13 horizontal modes can be clearly identified between 0.45 and 1.08 Hz. Beyond 1.10 Hz, the picture is overlain by modeshapes of the next-higher vertical mode (m = 2), then again at 1.65 Hz (m = 3), 2.15 Hz (m = 4) and so on. Peak displacement for each fundamental horizontal mode occurs at approximately x = 750m, in the deepest part of the valley, close to the western edge. Each higher n^{th} modeshape has n extremum points spread across the width of the valley, with a distribution centred toward the deepest part.

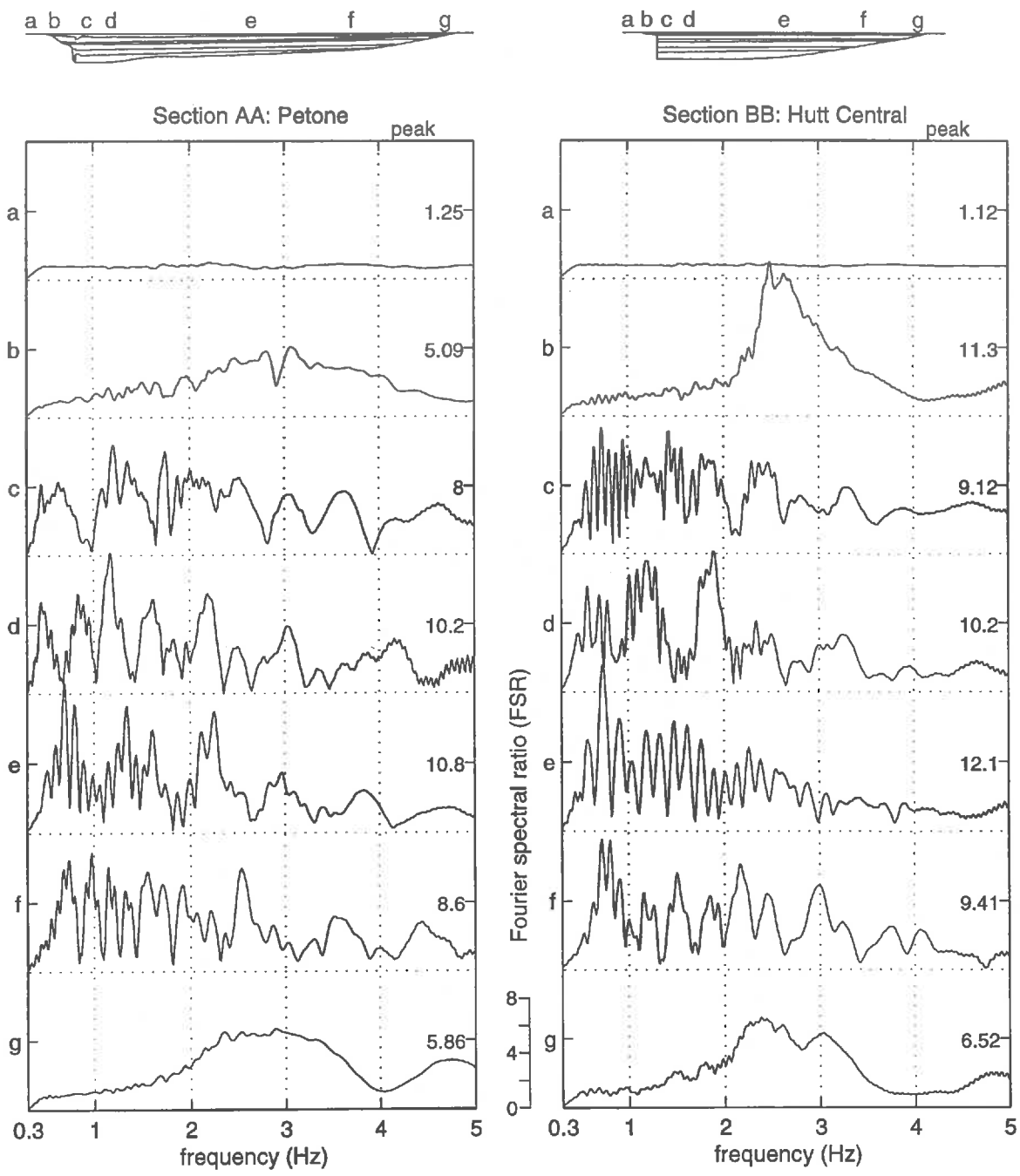

Figure 6.4. Fourier spectral ratio plotted at intervals across the surface of each model. Noisy results below 0.3 Hz have been filtered out.

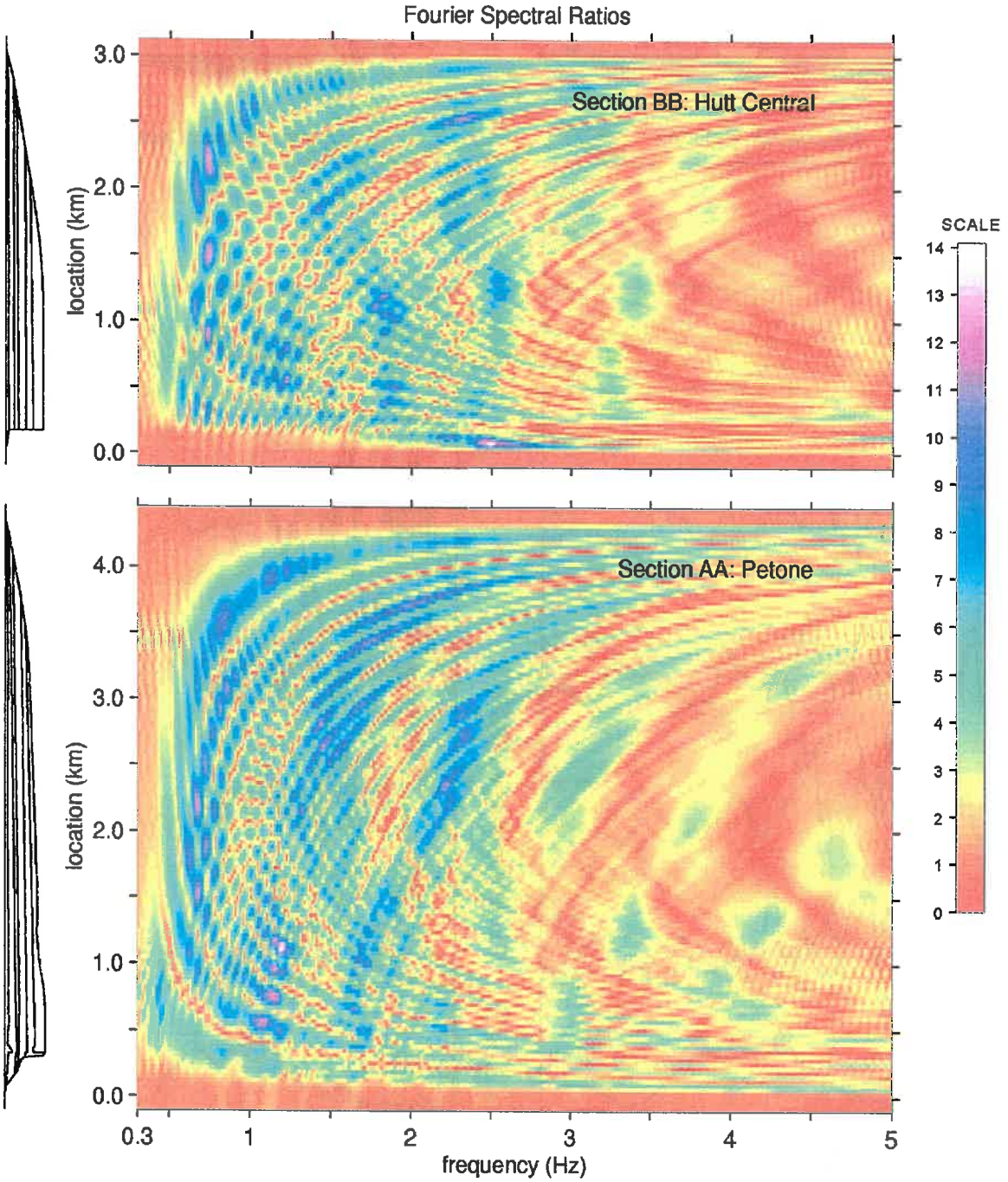

Figure 6.5. Space-frequency plot of Fourier spectral ratio for each cross-section. Amplitude is shown as a colour scale.

For any given eigenfrequency, f_{mn}, motions at the n peak/trough locations are amplified to differing degrees. For the first six or so horizontal modes (n = 1,2,3,..,6), the highest amplifications occur towards the centre of the valley, while for higher horizontal modes, the highest amplifications are found toward the edges. It appears that the highest amplifications within the first vertical mode set (m = 1) are closely associated with the first three extremum lines.

Amplification above 1.10 Hz is dependant on constructive interference between the first (m = 1) and higher (m = 2,3,4) vertical-mode sets. These *interference effects* (Wirgin, 1995a) alter the apparent strength and position of the resonant amplification. The highest amplification on the plot in Figure 6.5a occurs at x = 1100 m and f = 1.15 Hz where the second vertical mode set (m = 2) superimposes itself atop the 13th to 18th horizontal modes of the first vertical mode (m = 1, n = 13,14,..,18). Three other distinct patches of amplification in the region above 1.10 Hz also appear to occur due to interference.

Cross-Section BB: Hutt Central

The space-frequency FSR plot in Figure 6.5b shows amplification of a similar pattern and magnitude to that of the Petone cross-section. The first four vertical 2-D resonance sets (m = 1,2,3,4) can be identified on the plot, along with the first 15 horizontal modes of the first vertical mode (m = 1, n = 1,2,3,...,15). The eigenfrequencies from the plot are also listed in Table 6.1.

Widespread amplification with a FSR above 4 occurs in the range 0.4-3.5 Hz, and FSR above 8 occurs only below 3 Hz. The highest amplifications are associated both with the first few extremum lines of the first vertical mode set, and with interference between higher vertical mode-sets.

The distinct difference between this and the Petone Section, is the extremely large amplification (FSR = 14) on the western edge of the valley at 2.5 Hz. In section 6.1.1 we used 1-D elastic layer theory (Haskell, 1960) to calculate the fundamental resonant period as 0.4 seconds, corresponding to a frequency of 2.5 Hz. It appears that at the edge of the basin, the soil behaviour may be characterised by 1-D vertical resonance.

6.1.3 *REALISTIC EARTHQUAKE MOTIONS*

Using the transfer function method described in section 5.4, and employing the Kobe University basement record, transient acceleration traces were synthesised for various positions across the valley. The traces are shown in Figure 6.6. At position [a] at a rock site, the record is almost identical to the original KBU record shown previously in Figure 5.1, while at positions [b] to [g] the record has been extended in both duration and magnitude.

Traces at the edge positions [b] and [g] exhibit much stronger high frequency components than others. Here peak ground accelerations (PGA) reach approximately 0.59g, with the exception of position [b] on the Hutt Central section where the soft layer of fill excites ground accelerations up to 0.69g. At central positions within the valley, PGA varies from 0.8 to1.4g.

Figure 6.7 shows pseudo-spectral acceleration (PSA) response of a single-degree of freedom oscillator with 5% structural damping. The curves are very similar in shape to the FSR curves in Figure 6.4. Position [a] on the rock again mimics the original Kobe University data in section 5.4.1. At central positions [c], [d], [e] and [f] the maximum response occurs for input within the 0.5-2.5 Hz range, with often the highest peak around a frequency of 0.8 Hz. Peak PSA appears to vary between 3.0 and 5.5g. Edge positions [b] and [g] show a strong response for frequencies in the 2.5-3.5 Hz range, with a maximum response between 1.3 and 1.6g.

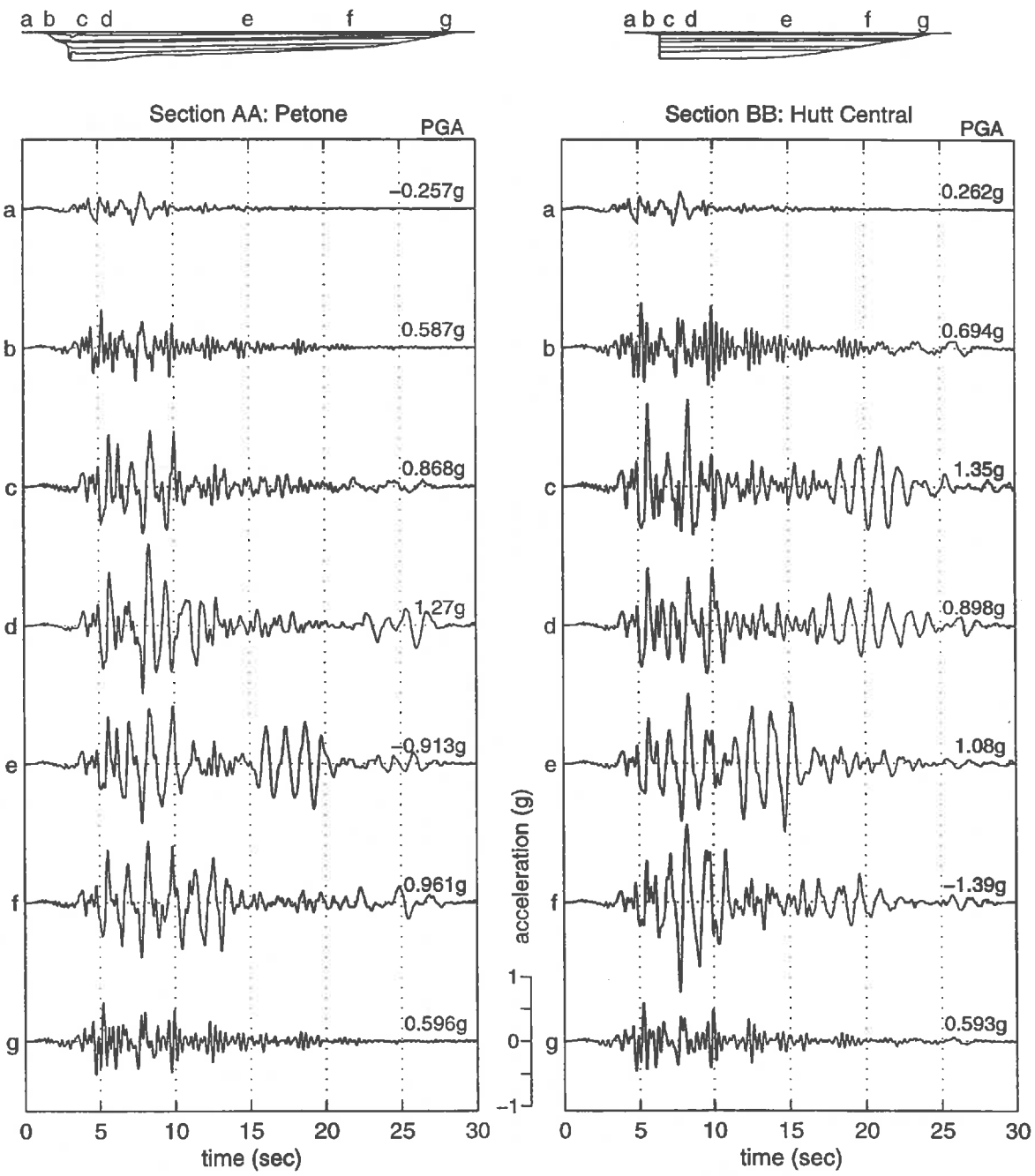

Figure 6.6. Synthetic acceleration traces for Lower Hutt cross sections. The time-histories have been calculated with transfer functions using the Kobe University basement record.

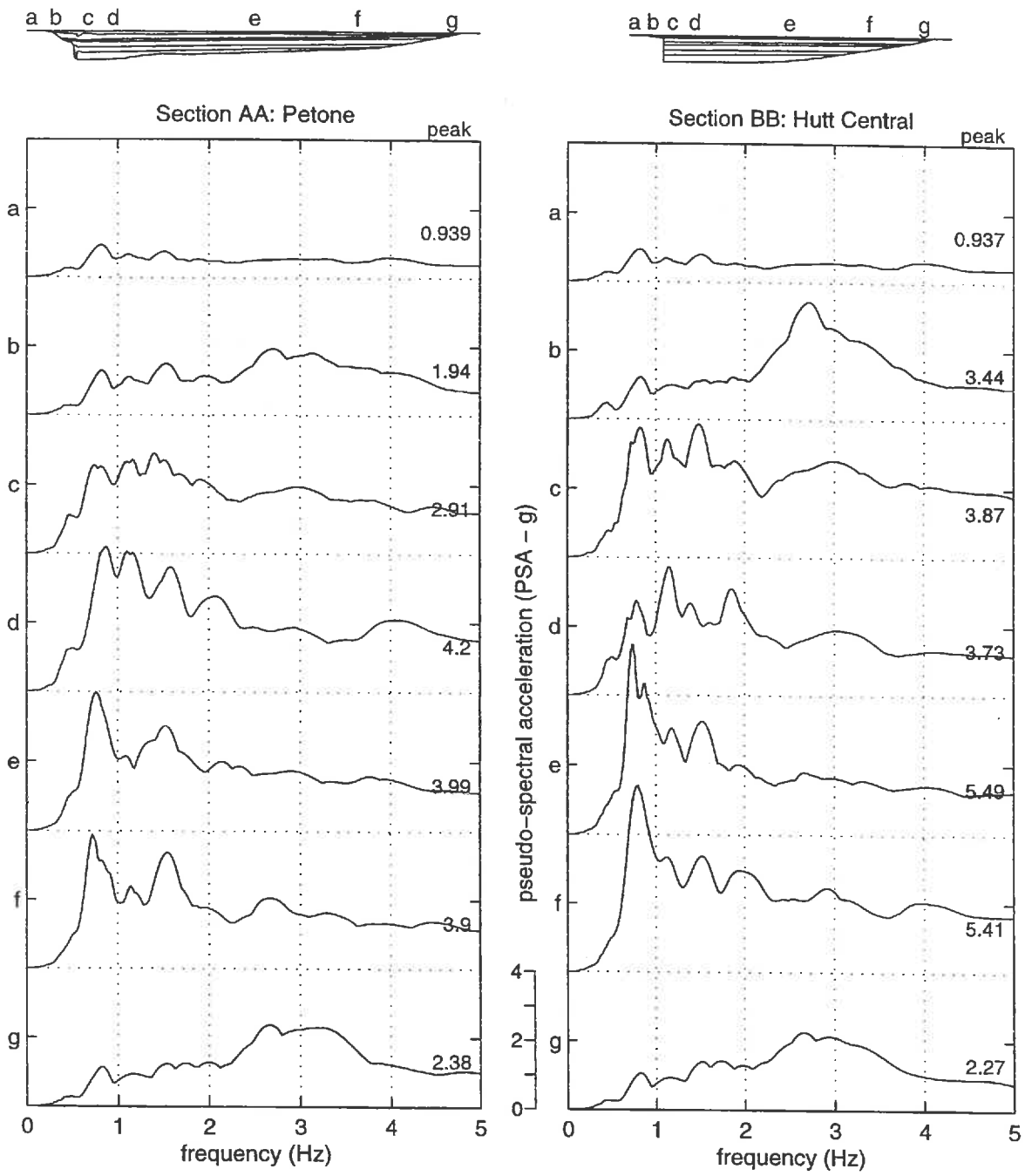

Figure 6.7. Pseudo-spectral acceleration (PSA) plots at various locations across each Lower Hutt section.

6.2 WELLINGTON (TE ARO) BASIN

The Te Aro basin beneath Wellington City is much smaller and shallower than the Lower Hutt Valley. A 2-D resonant amplification at higher frequencies than the Lower Hutt Valley is observed.

6.2.1 TIME-DOMAIN RESPONSE

Figure 6.8 shows a set of displacement seismograms at various positions across the valley. At position [a] on the rock, we see approximate free surface doubling of the Ricker wavelet displacement. Deformation in its shape may be due to topographical effects of the hills. At position [b] sited on shallow stiff sediment, there appears to be little amplification, while at other positions, the surface response has both a lengthened duration and amplified motions by up to six times that of the input. Figure 6.9 shows the maximum response of the seismograms against cross-valley position. The strongest peaks occur on the edges of the deep part of the basin at x = 230-400 m and x = 950-1060 m.

On the space-time displacement seismogram in Figure 6.10 we can recognise the amplified and delayed first arrival of the SH wave through the sediments, which is followed by a strong vertical reflection of the same wave off the sediment-rock interface.

Several edge waves appear to be induced and these travel across the basin from both sides. To the east, the edge waves appear to originate in the third layer down (D1) and have a phase velocity of approximately 260 m/s. Edge waves from the west appear to originate from various locations between 200 and 350 metres from the edge where the sediment thickness is between 15 and 55 metres deep. The phase velocity is approximately 250 m/s.

6.2.2 FREQUENCY-DOMAIN RESPONSE

The space-frequency plot of FSR in Figure 6.11 shows a quite systematic pattern of 2-D resonant amplification across the basin width.

Table 6.2 lists all the identifiable eigenfrequencies on the plot. Only the odd-numbered horizontal modeshapes can be seen, apparently due to the somewhat symmetrical nature of

the cross-section. High amplifications are associated in particular with the first extremum line, and the 5th horizontal mode belonging to the first vertical where we have FSR values up to 19. In general spectral ratios in the deep part of the basin are in the order of 6 to 10 over the frequency range 0.7 – 5.0 Hz.

Resonant amplification occurs only over the deep part of the basin. The area from x = 0-100 m, underlain by less than 10 m of stiffer sediment exhibits no special amplification. The 2-D modeshapes in the deeper part are skewed to the east such that the peak of the first horizontal mode lies above the deepest sedimentary column.

f_{mn} (Hz)	Horizontal Mode (n)	Vertical Mode (m) 1	2	3
	1	0.80	3.00	4.50
	2			
	3	1.20		
	4			
	5	1.45		
	6			
	7	1.70		
	8			
	9	1.90		
	10			
	11	2.12		
	12			
	13	2.32		
	14			
	15	2.50		
	16			
	17	2.70		

Table 6.2. Identifiable eigenfrequencies from Figure 6.11. Blank spaces indicate modes that do not cause significant amplification

6.2.3 REALISTIC EARTHQUAKE MOTIONS

Time-histories have been calculated at various positions across the Te Aro basin, again using the Kobe University basement motion. The results have been plotted in Figure 6.12. At positions [a] and [b], on rock and shallow sediments respectively, the output is similar to the input KBU record. At other sites within the deeper part of the basin, the motion has been amplified and extended in duration. The largest motion occurs in the deepest part of the basin at approximately x = 800 m. Here the PGA is as high as 1.2g.

Figure 6.13 shows the pseudo-spectral response of a SDOF oscillator at various positions. The strongest response (4.6g) occurs at position [f] for a frequency of 0.8 Hz. Positions [d]

and [e] show quite a broad-spectrum response with peaks of 3.1 and 3.8g respectively. At the edge positions [c] and [g] peak response occurs around 3-4 Hz, while position [b] shows no significant amplification.

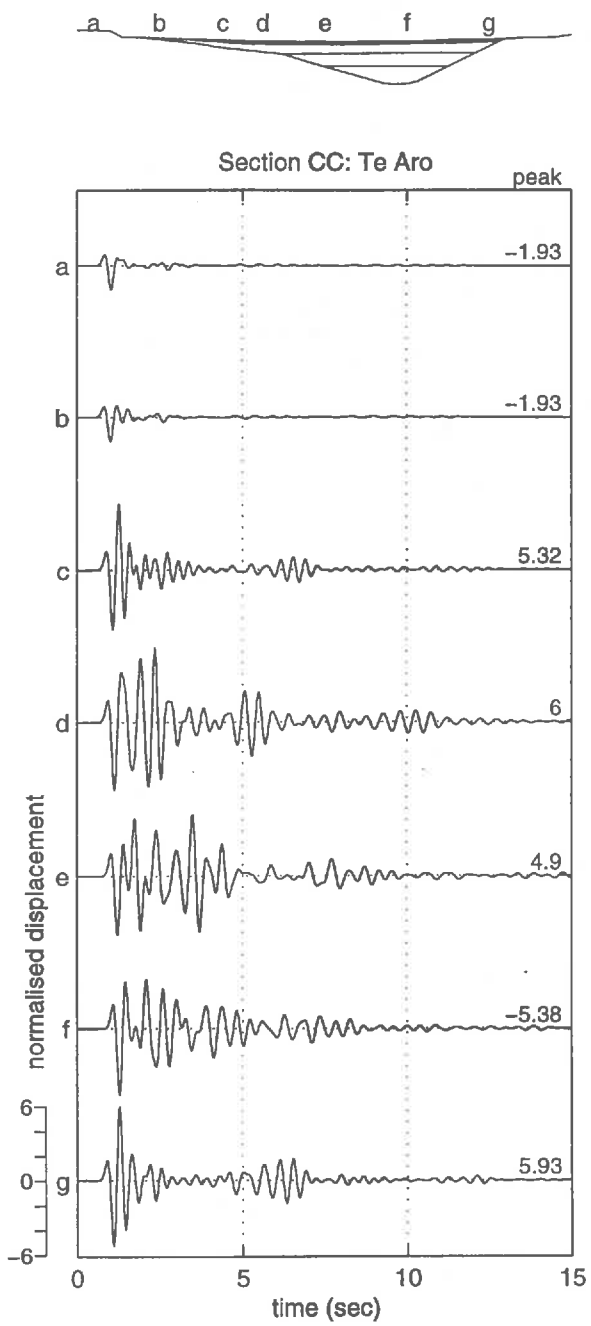

Figure 6.8. Displacement seismograms at various positions across the Te Aro section for a Ricker wave input.

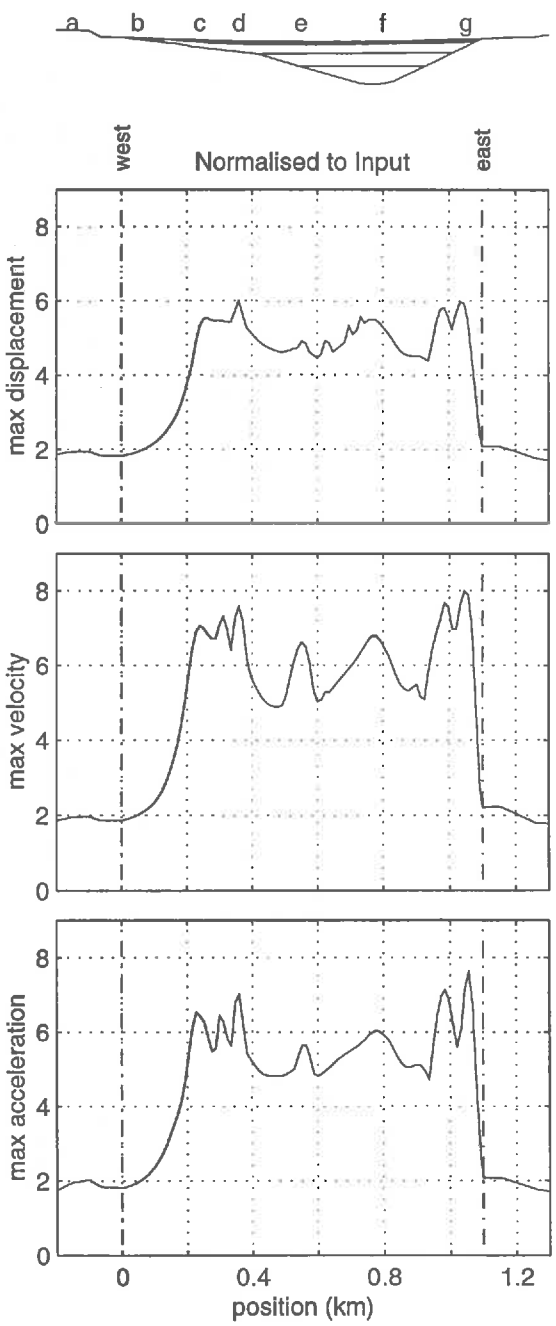

Figure 6.9. Plots of maximum displacement, velocity and acceleration versus across-valley position for the Te Aro cross section. Amplitude has been normalised with respect to the input Ricker wavelet (see section 3.2.4).

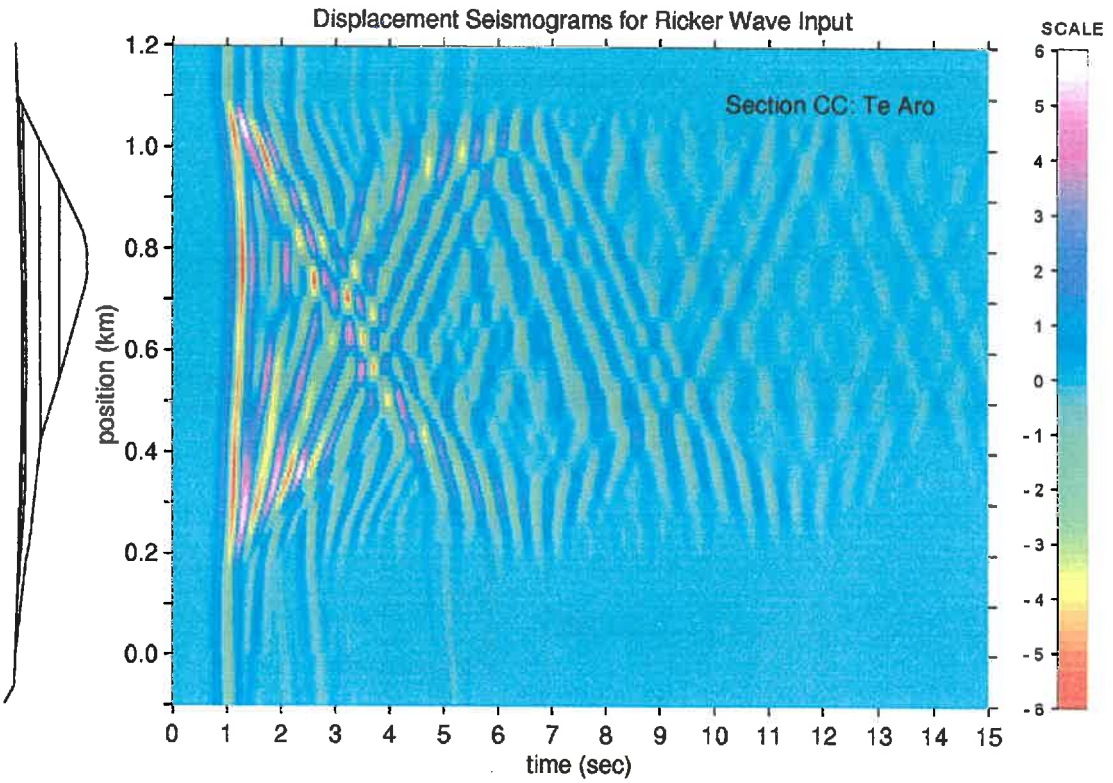

Figure 6.10. Space-time plot of displacement seismograms for an incident Ricker wavelet through the Te Aro cross-section.

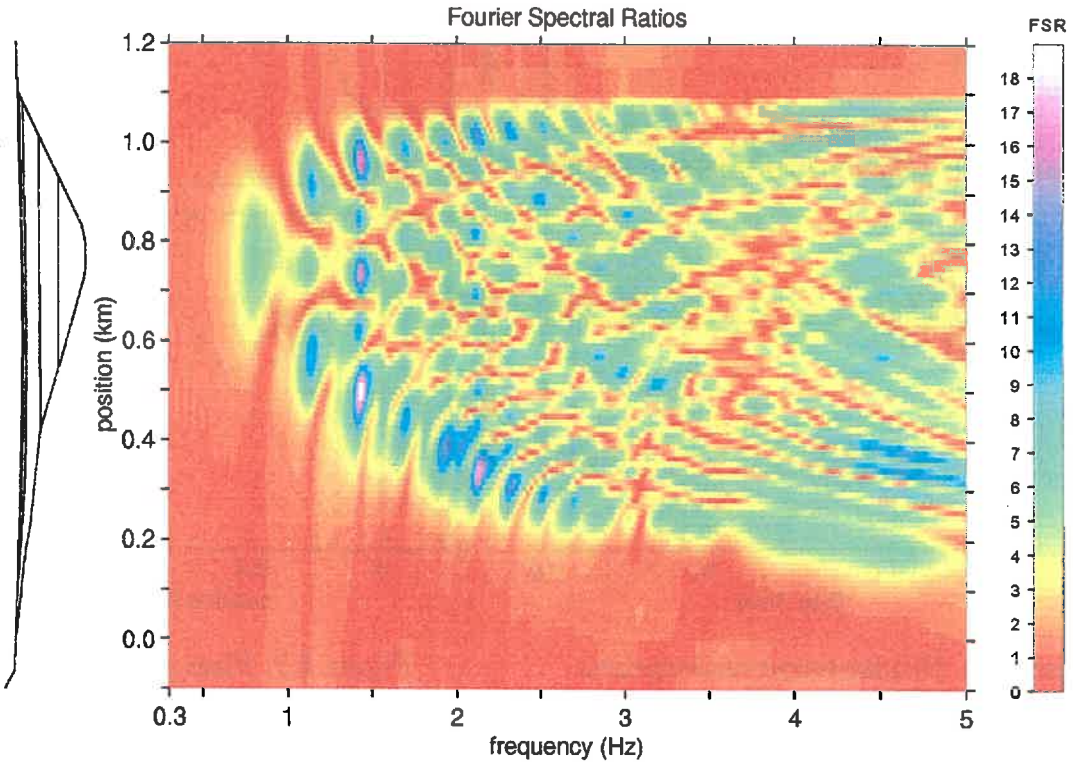

Figure 6.11. Space-frequency plot of Fourier spectral ratio for the Wellington cross-section.

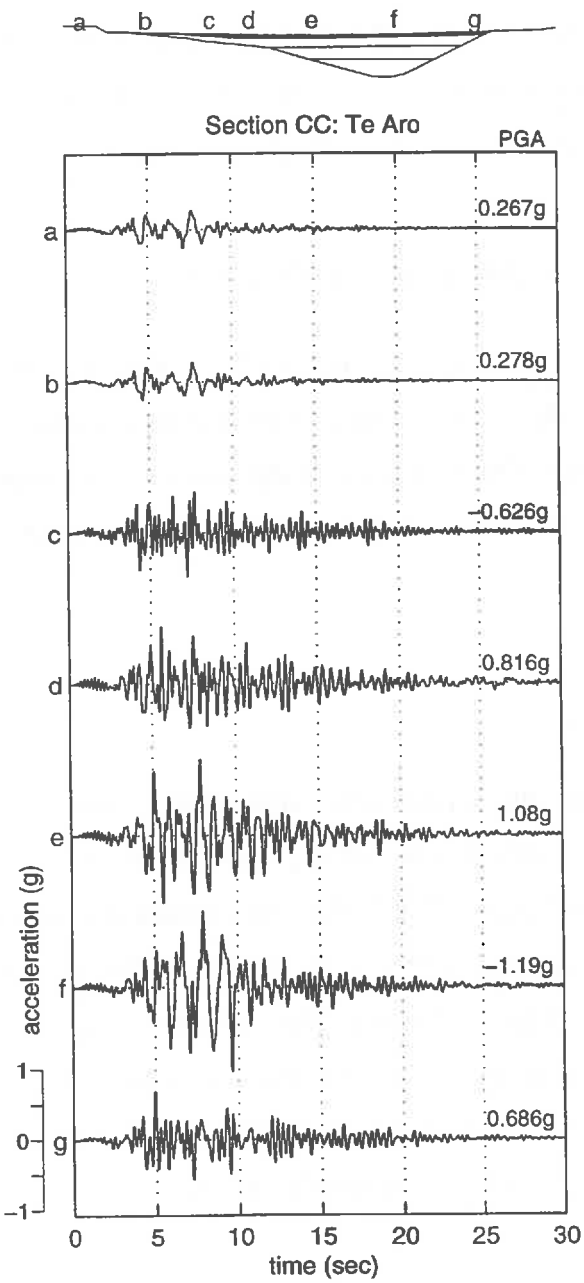

Figure 6.12. Synthetic acceleration traces for the Te Aro bsain. The time-histories have been calculated with transfer functions using the Kobe University basement record.

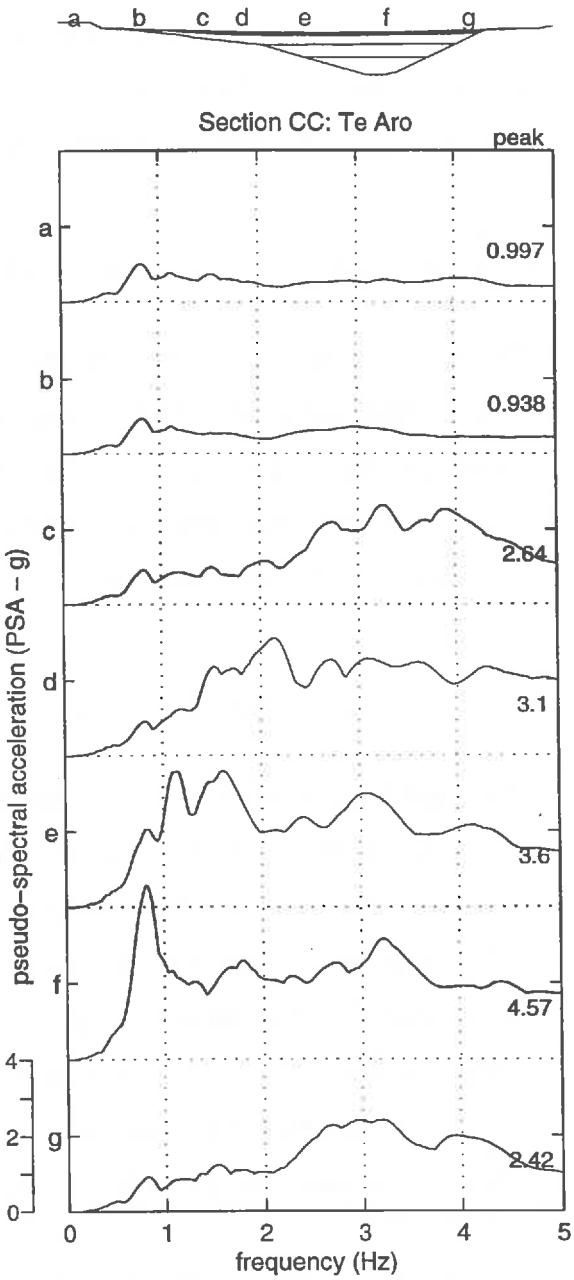

Figure 6.13. Pseudo-spectral acceleration (PSA) plots at various locations across Te Aro.

Chapter 7: DISCUSSION

Results indicate that various parts of the Lower Hutt and Wellington regions are likely to be dominated to various degrees by the effects of one-, two- or three-dimensional resonance; and edge effects such as vertical resonance or the basin edge effect.

7.1 Seismic Behaviour of the Lower Hutt Valley

Results from cross-sections through the Lower Hutt Valley both at Petone and Hutt Central have many similarities. It appears that the response is governed by the interaction of two significant 2-D features of the valley. The first is the sharp lateral discontinuity in the form of the Wellington Fault along the western side of the valley, and the second is the two-dimensional basin structure.

7.1.1 The Basin Edge Effect

The fault-plane forming a vertical western edge to the valley appears to lie between 100 and 300 metres from the base of the western hills (Begg and Mazengarb, 1996). Seismograms from both cross-sections in Figure 6.2 and plots of maximum response in Figure 6.3 indicate that the *basin edge effect* will occur some 70-200 m further into the valley from this discontinuity. In both cases the basin-edge effect creates strong pulses of energy in the displacement, velocity or acceleration seismograms. It is likely that these strong pulses could be damaging in a real earthquake. In the frequency-domain it is difficult to identify any amplification due solely to the basin-edge effect.

Indications are that the basin-edge effect should occur along the whole length of the Lower Hutt Valley's western edge. Its distance from the vertical fault-plane is likely to decrease further up the valley as the sediment thins. The narrow band of strong motion will, at the top end of the valley, be situated along the line of the Hutt River, which meanders down the western edge until reaching Lower Hutt Central where its course takes it diagonally across the valley. The lack of buildings close to the river will be beneficial, although the strong shaking here could increase the liklihood of liquefaction on the

riverbanks, and damage to the important Ewen, Melling, and Kennedy Good Bridges. South of Lower Hutt Central, through Petone, the band of strong shaking will be located in an area of residential and industrial buildings.

7.1.2 TWO-DIMENSIONAL RESONANCE

Plots of Fourier spectral ratio show clearly a two-dimensional resonant amplification pattern in the Hutt Valley with many similarities to the analytical solution for a simple homogeneous rectangular valley (Bard and Bouchon, 1985; Bielak et. al., 1997) in figure 2.2. Because the deepest part of the valley is found adjacent to the fault along the western edge, the resonant modeshapes are all skewed westward. Higher resonant modes (both vertical and horizontal) have been attenuated in the soft soil, and have much lower amplitudes. In general, the soil exhibits spectral ratios up to 14 at certain locations across the entire width of the valley between 0.3 and 2.5 Hz, and ratios up to 4 over the whole frequency range studied (0-5Hz).

The close spacing of eigenfrequencies in the Hutt Valley are a distinguishing feature separating it from smaller basins such as Te Aro, Wellington. From equation [2.3] for eigenfrequencies in a simple rectangular valley we can see that the frequency spacing of horizontal eigenmodes ($f_{m,n}, f_{m,n+1}, f_{m,n+2}, \ldots$) is a function the ratio $2H/L$, thus the wider and shallower the valley, the closer the modes will be. Since the width:depth ratio is relatively constant over the lower 5km of the valley, the resonant frequencies are similar for both cross-sections.

Although the 2-D pattern is clear, interference from higher vertical-mode sets has created a complex patchwork of amplification. While in a general sense, we can characterise amplification by patches in space-frequency, in a local sense amplification is also highly variable in both dimensions. A 0.1 Hz change on frequency or a 300 m change in cross-valley position may alter the amplification by as much as 14 times. Whether or not it is possible to actually record such sharp changes in amplification is unknown.

The synthesis of realistic earthquake records using computed transfer functions and the Kobe University north-south record gives an idea of ground motions likely during a major rupture of the Wellington fault. The KBU record contains most of its energy in the low

frequency 0-2.0 Hz range. This coincides nicely with the high spectral amplification of the basin in the 0.3 – 2.5 Hz range. Thus for most positions within the basin, frequencies between 0.5 and 2.0 Hz are most strongly excited. The highest values of PSA are found at approximately 0.8 Hz in both cross-sections.

7.1.3 Validity of a Two-Dimensional Analysis

The use of 2-D rather than 1-D modeling has shown beyond doubt the significance of 2-D effects in magnifying and changing the form of the basin response. It is crucial then that we have some idea of how good our 2-D approximation is at modeling the real 3-D situation in the Hutt Valley. The geometry of the valley is essentially a triangular wedge of sediments extending 10km southwest from Taita Gorge, to reach a maximum width of 4.5km and depth of 300m at the Petone shoreline. The two sides of the wedge diverge at an angle of approximately 21°, while the rock basement surface has a down-valley dip of approximately 1.5°. Similarly deep sediments extend out into Port Nicholson below the sea level, before terminating gradually near Wellington and the harbour entrance as basement rock rises to the surface.

The western side of the valley is relatively straight, following the vertical edge of the Wellington Fault. Several streams (such as Korokoro, Speedys and others) have incised into the surrounding hills triangular-shaped valleys draining into the Hutt Valley and forming small infilled 'nicks' in the otherwise straight valley side. The eastern side of the valley forms a much more ragged edge as sediments have been deposited along the contour of the hill. One major irregularity on the eastern side is the Naenae basin, which widens the valley locally from 2.0 to 3.5km near the northern end. These irregular eastern hills also indicate that the base of the sediment wedge is likely to also have an irregular surface in the longitudinal direction.

Although the sediment wedge does not extend as a prismatic shape with constant cross-section to infinity in either direction, we do have a basin that is significantly longer than wide. Our cross-sections of width 3-4km and depth 0.3km are modelling a sediment wedge approximately 18km long. Marsh (1992) suggests that because 2-D effects become insignificant in the central regions of a cross-section for which the width is greater than 16 times the depth, it should be adequate to disregard 3-D effects when the out-of-plane

distance to the basin edge is greater than 8 times the depth. For our 300m deep cross-section this would equate to only 2.4km, while there exists at least 8km in each direction. The conclusion is that we can disregard 2-D effects when a site is sufficiently far from the basin edge such that edge waves have decayed in amplitude such that they are too small to cause amplification by horizontal resonance or interference edge effects.

The open-ended nature of the Lower Hutt valley makes the presence of horizontal resonance in the longitudinal direction unlikely, although edge effects in this direction are a distinct possibility. The northern 4-5km of the valley and the Naenae sub-basin are very likely to exhibit a 3-D response due to the highly enclosed and irregular nature of their geometry. Down valley, however, the 5km from Avalon to Petone is quite open-ended in both directions, and likely to be dominated by 2-D cross-valley behaviour. This lower part of the valley will, however, still be subject to some longitudinal (3-D) edge effects. Irregularities along the eastern margin appear to have the potential to create localised out-of-plane edge waves that cannot be accounted for in the 2-D model. Directivity (rupture propagation) and energy radiation effects are also likely to be significant, yet are unaccounted for by the 2-D model.

7.2 Seismic Behaviour of Wellington City

With the absence of a sub-surface vertical side to the Te Aro basin, and with no evidence of the basin edge effect in the results, it appears that multi-dimensional resonance of the sediments will be the major concern in the Te Aro area of Wellington City. The Thorndon area of the City is, however, sited adjacent to the Wellington Fault and may be subject to the basin edge effect.

7.2.1 Two- and Three-Dimensional Resonance and Edge Effects

The Te Aro basin is much more three-dimensional than in the Hutt Valley, being only as long as it is wide (refer to Figure 4.4). Surface waves are generated on the eastern and western edges of our section to create resonance in the east-west direction. To the south, the basin is bounded by bedrock only 1km perpendicular from our cross-section. To the north, the basin is quite open ended and unlikely to trap seismic energy thus eliminating

the likelihood of horizontal resonance in the north-south direction. For this reason it is unlikely that the resonant frequencies of the basin will change with a 3-D analysis.

Edge waves will undoubtedly still be refracted from the south (as well as the east and west), creating a longer and stronger response. Spectral ratios may be increased slightly in a broad-band fashion, giving a slightly stronger response at all frequencies. With these limitations of our 2-D model in mind, it would be prudent to view results from this 2-D analysis as a good indication toward the real response.

7.2.2 Possibility of the Basin Edge Effect in Thorndon

In the Thorndon area, a deep layer of sediments is bounded to the west by the sub-vertical bedrock wall of the Wellington Fault. The situation is complicated by the sharp ridge of Kelburn hill dipping into the sediments from the south. The sediments here are largely unbounded to the east. Although we have not simulated shaking in this area, the steep sub-surface wall along the fault-line could well be expected to create a 2-D response with similarities to that identified in the Lower Hutt.

Edge-waves refracted from the basin edge along Tinakori and Kelburn hills are likely to produce significantly stronger shaking of longer duration than a 1-D model would predict. The basin edge effect is prone to occur in a similar fashion as it does up the length of the Lower Hutt, some 70-200m out from the vertical wall of the fault. The area susceptible includes a strip of land a few-hundred metres wide from the Tinakori-Hutt Road out past the Wellington Urban Motorway into Thorndon and the railway yards, from the Hill Street overbridge north past the InterIslander Ferry Terminal.

The presence of the Kelburn spur dipping beneath Thorndon does create a very interesting problem of wave diffraction and reflection in the Thorndon waterfront area. Only a three-dimensional analysis of the situation would give a realistic idea of the response. It is suggested that engineers and planners working in this area take into account the possibility of a much stronger than expected shaking.

7.3 NON-LINEAR SOIL BEHAVIOUR

Soft flexible basin sediments are expected to lose stiffness and behave in a non-linear inelastic manner during strong seismic excitation. Non-linear behaviour tends to increase the damping and reduce the shear modulus and shear-wave velocity, thus decreasing the natural frequencies of a basin. A reduction in the maximum displacements, velocities and accelerations and an increase in the duration of strong motion are also expected. Testing of soft cohesionless sands and gravels has shown that material damping increases dramatically above cyclic shear strains of 10^{-2} to 10^{-3} %, indicating the onset of inelastic behaviour (Beresnev and Wen, 1996; Isibashi and Zhang, 1993; Seed et. al., 1986). Non-linearity generally becomes apparent above PGA's of 0.1 to 0.2g, above which permanent soil deformation should be expected (Beresnev and Wen, 1996).

In this study we have used the computationally efficient linear method of analysis, assuming elastic behaviour of all modelled materials. Maximum strains between 3×10^{-1} - 6×10^{-1} % (ε_{yz}) and 5×10^{-1} - 14×10^{-1} % (ε_{xz}) have been calculated at the surface of the section through Lower Hutt Central, under a Kobe (1995) type loading. Peak ground accelerations of up to 1.2-1.4g are also expected in both the Lower Hutt and Te Aro. These suggest that the soft cohesionless soils would definitely exhibit highly non-linear behaviour during a major earthquake. There is, however, substantial evidence that results from an elastic analysis can be quite accurate at determining the spatial distribution, resonant frequencies and Fourier spectral ratios of amplification and to a lesser extent the form of the expected seismogram.

Larkin and Marsh (1991) and Marsh (1992) with their 2-D finite-difference modelling, compared linear and non-linear solutions, concluding that non-linear effects on basin response were important for large-magnitude earthquakes. At shear strains of 0.31%, non-linearity had the effect of stretching the duration of intense shaking by a factor of 2, while reducing the peak ground acceleration by a factor of 1.5 and reducing the acceleration response spectra by a factor of 2. A surprising result was the similarity of both amplitude and frequency in the Fourier spectra of the two analyses.

There is substantial evidence (eg. King and Tucker, 1984; Borcherdt et. al., 1989) that linear results from elastic modelling or weak-motion recordings may be used successfully

to predict both the amplified frequencies and to a lesser extent the amplitude of spectral ratio peaks for strong motion shaking up to at least 0.1 or 0.2g. For higher PGA, Lermo and Chavez-Garcia (1994) conclude from studies in Oaxaca, Acapulco and Mexico City that micro-tremors can be used successfully to estimate at least the fundamental frequency of a site in the range 0.3 to 5.0 Hz.

Taber and Smith (1992) suggest that the frequency of amplified shaking will remain the same for when extrapolating Fourier spectral data from weak to strong motions. Since weak motions have been used to successfully predict zones of strong shaking during a large earthquake (Taber, 1995), it is reasonable to expect that the spatial variability of shaking observed in our elastic models will hold approximately during a major event.

Results from our elastic analyses are likely to be on the conservative side of reality in terms of peak response. Non-linear effects will probably lead to lower peak velocity and accelerations. The spectral ratios may be reasonably accurate, while the real duration of shaking is likely to be much longer than predicted. It would be sagacious to look at records from other bedrock-bounded valleys to get an idea of the duration to be expected.

7.4 Model Sensitivity

Various factors have the ability to influence the form and values of our results. Small errors associated with the material properties and geometric shape of the model, or the input of shaking may lead to uncertainty in the resonant frequencies, spectral ratios, peak values, shaking duration and spatial distribution of shaking. Although we have done no specific sensitivity testing for our models, we can make reasonable estimates toward the uncertainty associated with various factors.

7.4.1 Material Properties

Elastic Properties

The elastic nature of the rock and soil units is described in our model by the shear wave velocity, Poisson's ratio and the bulk density. For each layer we have made estimates for the value of each property as described in Chapter 4. It is likely that our estimates are

within 20% of reality. Lower shear wave velocities in the sediments would lead to a magnification of the elastic soil response and a lowering of the basin's natural frequencies.

The impedance ratio between the bedrock and soil – a function of the difference in shear wave velocity and density between the units - determines the amount of energy that is trapped within the basin by internal reflections. Thus it determines the amplification of both magnitude and duration, especially that caused by vertical and horizontal resonance. Although the impedance ratio has no effect on eigenfrequencies nor the position of resonant peaks - both of which are purely a function of the geometry and shear wave velocity of the sediments - it does determine the position of the basin edge effect. Using equation [2.9] for a simple valley shape and Hutt-Valley-like dimensions and shear wave velocities, we find a 20% change in the velocity ratio may alter the position of the basin edge effect in the order of only 10 m.

Damping

Both the rock and soil units have been assigned material damping ratios 2% of critical. Damping determines the amount of energy that is absorbed by seismic waves as they travel through a medium. In particular, damping determines the rate of amplitude loss and hence the effective distance that surface waves travel back and forth across a basin. Thus it is a factor in the magnitude but not the spatial location of resonant and basin edge amplification. Since soil damping will undoubtedly increase with the onset of non-linear behaviour, this low value is quite conservative.

7.4.2 BASIN GEOMETRY

The bedrock boundary is reasonably well described by gravity survey contours for both the Lower Hutt Valley and the Te Aro Basin. Comparing section AA and section BB in the Lower Hutt, we see the difference in cross-sectional shape has little influence on the overall behaviour of the basin, eigenfrequencies, spectral ratios, peak ground accelerations or the shaking duration. A change in width does alter the spatial resonance pattern, grouping extremum points closer together. The position of the basin edge effect is highly dependant on the shape of the bedrock-sediment boundary at the edge, as it appears to determine which layer the causal edge-wave will propagate through. Nevertheless, the

basin edge effect in the Lower Hutt cross sections appears to depend more so on the position of the vertical fault wall.

7.5 RECOMMENDATIONS FOR FURTHER WORK

During the course of this study we have identified several lines of research that could lead on from our reported work:

1. Modelling the effects of topographic hills on each side of the valley to determine their influence on the valley response.

2. Use of 3-D non-linear modelling techniques (eg. Hisada, et. al., 1998).

3. Modelling other incident waveforms. In this study we have restricted ourselves to the anti-plane SH case.

4. Including fault rupture within the model (eg. Pitarka et. al., 1998).

5. Modelling other urbanised sedimentary basins in the region for multi-dimensional resonance and edge effects.

6. Validating model results with data from closely spaced seismic arrays in the Lower Hutt and Wellington.

The authors are currently engaged in further investigation of the basin edge effect. Weak-motion data from a closely spaced set of recorders across the fault trace in Lower Hutt has recently been collected for comparison with modelling results.

Chapter 8: CONCLUSIONS

The seismic response of the southern Lower Hutt Valley is characterised by two-dimensional resonance across its width, the basin-edge effect along a band parallel to the Wellington Fault and one-dimensional vertical resonance close to all edges.

- Two-dimensional resonance describes the behaviour of the full width excluding a 100m wide band adjacent to each edge. Frequencies within the range 0.3 to 3.5 Hz are amplified up to a Fourier spectral ratio (FSR) exceeding 14. The distribution of amplification is highly variable with both location and frequency. Resonant interference effects are the cause strong amplification at frequencies above 1.1 Hz. Two-dimensional resonance in the event of a Wellington Fault rupture may produce peak ground accelerations (PGA) in the order of 0.8g to 1.3g across most of the valley. Pseudo-spectral acceleration (PSA) is maximum in the central two-thirds of the valley for frequencies between 0.5 and 2.0 Hz, and is expected to have a peak value of 3.0-5.5g for frequencies around 0.8 Hz.

- The basin-edge effect creates strong displacement, velocity, and acceleration pulses in the seismogram along a narrow band parallel-to and some 70-200 m southeast of the Wellington Fault trace. PGA may reach 1.4g in the event of a Wellington Fault rupture. The basin-edge effect is strongly dependant on the presence of the sub-surface vertical wall forming the western side of the valley.

- One-dimensional vertical resonance of shallow sediments within 100 metres of the valley edges amplifies frequencies within the range 2.0 to 3.5 Hz up to a FSR exceeding 6. In areas of soft fill, the FSR may exceed 14. PGA at these locations for a Wellington fault rupture is estimated at 0.6- 0.7g. PSA shows broad-band amplification between 0.5 and 3.5 Hz, with peak values up to 3.5g for 2.5 Hz input.

The smaller Te Aro Basin in Wellington City exhibits a multi-dimensional resonant response across its deeper parts, while the edges may be characterised by 1-D vertical resonant effects.

- Our modelling shows two-dimensional resonance amplifying frequencies between 0.7 and 5.0 Hz up to a FSR exceeding 19. In the event of a Wellington Fault rupture, PGA may reach 1.2g in the deepest part of the basin, decaying to 0.65g at the edges. Corresponding pseudo-spectral accelerations are amplified over a broad band between 0.5 and 4.5 Hz, with a peak value of 4.6g at 0.85 Hz in the deepest part of the valley. The propagation of surface waves in a northerly direction may increase amplification further.

- One-dimensional resonance of soft shallow sediments at the basin edges amplifies frequencies in the 3 to 5 Hz range up to FSR of approximately 8. Here PGA may reach values of 0.69g and PSA may reach 1.12g over a broad frequency band.

Other locations in the Wellington region may be subject to strong shaking as a result of multi-dimensional site effects.

- The Thorndon area will undoubtedly be subject to an amplification caused by surface waves propagating away from Tinakori and Kelburn hills. It is likely that some form of the constructive basin-edge effect will occur in this area, creating strong and damaging pulses of energy.

- Various other sedimentary basins such as Upper Hutt, Wainuiomata, Porirua and Mirimar are likely to amplify seismic motions by the mechanisms of two- and three-dimensional resonance.

A two-dimensional technique of analysis has been proved to be very useful in determining the seismic response of both the Lower Hutt Valley and Te Aro Basin. Both depressions are open-ended in at least one direction, making the presence of horizontal resonance in that direction unlikely. The propagation of surface waves in the out-of-plane (z) direction is, however, likely to cause higher amplification throughout and constructive edge-effects in both cross-sections that have been left unaccounted-for by our 2-D modelling.

The FEM elastic analysis tool, Archimedes, has delivered accurate results throughout the modelling. Several results such as the resonant frequency for a one-dimensional flat layer,

the surface doubling effect of waves at the free surface and the pattern of two-dimensional resonance have been verified by analytical theory.

Although we are using linear methods to model soils that will probably behave in a highly non-linear fashion, our results can be applied to strong-motion shaking. Our elastic model should conservatively over-predict values of PGA and PSA. It should provide a reasonable estimate of the frequency content of shaking and the FSR values. The model should also accurately determine the important spatial distribution of amplification. We do however expect it to under-predict the duration of shaking

Finally, it would be prudent for planners and developers to be aware of the risks associated with urban development within the Lower Hutt Valley and Te Aro Basin, and to ensure adequate protection is available to withstand the type of very strong ground shaking outlined above.

ACKNOWLEDGEMENTS

We are indebted to Jacobo Beilak, Jifeng Xu (Department of Civil and Environmental Engineering, Carnegie Mellon University, Pittsburgh, PA.) and Dave O'Hallaron (Department of Computer Science, CMU) for their help with the Archimedes computation.

Thanks to Nick Perrin, Peter Wood, John Haines, Rafael Benites and Bill Stephenson (Institute of Geological and Nuclear Sciences, Lower Hutt) for their useful discussions and help with collation of the geological data.

This research was funded by the Earthquake Commission of New Zealand (EQC) and the University of Canterbury.

REFERENCES

Aki, K. (1988) Local Site Effects on Strong Ground Motion. Proc. Earthquake Eng. Soil Dyn. II: 103-155.

Aki, K. (1993) Local Site Effects on Weak and Strong Ground Motion. Tectonophysics 218: 93-111.

Aki, K. and Larner, KL. (1970) Surface Motion of a Layered Medium Having an Irregular Interface due to Incident Plane SH Waves. J. Geophys. Res. 75: 933-954.

Al-Hunaidi, M.O. (1989) Numerical Modelling of the Radiation Condition of Unbounded Media. In: Engineering Seismology and Site Response: Proceedings of the 4th International Conference on Soil Dymanics and Earthquake Engineering, Mexico City, Mexico, October 1989. Editors: A.S. Cakmak and I. Herrera.

Bao, H.; Bielak, J.; Ghattas, O.; Kallivokas, LF.; O'Hallaron, DR.; Shewchuk, JR.; Xu, J. (1996) Earthquake Ground Motion Modeling on Parallel Computers. Proc. Supercomputing '96, November 1996, Pittsburgh, PA.

Bao, H.; Bielak, J.; Ghattas, O.; Kallivokas, LF.; O'Hallaron, DR.; Shewchuk, JR.; Xu, J. (1997) Large-Scale Simulation of Elastic Wave Propagation in Heterogeneous Media on Parallel Computers. Technical Report No. CMU-CML-97-100, Carnegie Mellon University, Pittsburgh, PA.

Bard, PY. (1994) Effects of Surface Geology on Ground Motion: Recent Results and Remaining Issues. Proc. 10th European Conference on Earthquake Engineering, 1: 305-325.

Bard, PY. and Bouchon, M. (1985) The Two-Dimensional Resonance of Sediment-Filled Valleys. Bull. Seism. Soc. Am. 75: 519-541.

Bard, PY.; Bouchon, M. (1980a) Seismic Response of Sediment Filled Valleys Part 1: The Case of Incident SH Waves. Bull. Seism. Soc. Am. 70(4):1263-1286.

Bard, PY.; Bouchon, M. (1980b) Seismic Response of Sediment Filled Valleys Part 2: The Case of Incident P and SV Waves. Bull. Seism. Soc. Am. 70(4):1921-1941.

Bardet, JP.; Kapusker, M.; Martin, GR.; Proubet, J. (1992) Marina District: Site-Response Analyses. U.S. Geological Survey Professional Paper 1551-F ppF85-F140.

Begg, JG.; Mazengarb, C. (1996) Geology of the Wellington Area, Scale 1:50,000. Institute of Geological and Nuclear Sciences Geological Map 22. 1 sheet + 128p. Lower Hutt, NZ: IGNS Ltd.

Beresnev, IA. And Wen, KL. (1996) Review: Non-Linear Soil Response - A Reality? Bull. Seism. Soc. Am. 86(6): 1964-1978.

Berrill, JB. (1996) Near Field Seismic Design Motions: A Case Study from Wellington, New Zealand. Proc. 7th A. NZ. Geomech. Conf. Adelaide, pp 282-287.

Bert, C.W. (1973) Material Damping: An Introductory Review of Mathematical Models, Measures and Experimental Techniques. Journal of Sound and Vibration 29(2): 129-153.

Berryman, KR. (1990) Late Quaternary Movement on the Wellington Fault in the Upper Hutt Area, New Zealand. NZ. J. Geol. Geophys. 33: 257-270.

Bielak, J. and Christiano, P. (1984) On the Effective Seismic Input for Nonlinear Soil-Structure Interaction Systems. Earthq. Eng. and Struct. Dyn. 12: 107-119.

Bielak, J.; Xu, J.; Ghattas, O. (1997) On earthquake Ground Motion and Structural Response in Alluvial Valleys. Technical Report No. CMU-CML-97-101, Carnegie Mellon University, Pittsburgh, PA.

Boore, DM. (1970) Love Waves in Nonuniform Wave Guides: Finite Difference Calculations. J. Geophys. Res. 75 (8): 1512-1527.

Boore, DM. (1972) Finite Difference Methods for Seismic Wave Propagation in Heterogenous Materials. In: Methods in Computational Physics, 11: 1-36. Ed. BA. Bolt, Academic Press, New York.

Boore, DM.; Larner, KL.; Aki, K. (1971) Comparison of Two Independent Methods for the Solution of Wave Scattering Problems: Response of a Sedimentary Basin to Incident SH Waves. J. Geophys. Res. 76: 558-569.

Borcherdt, R.D. (1970) Effects of Local Geology on Ground Motion Near San Fransisco Bay. Bull. Seism. Soc. Am. 60 (1): 29-61.

Borcherdt, R.D.; Glassmoyer, G.; Andrews, M.; Cranswick, E. (1989) Effects of Site Conditions on Ground Motion and Damage. In: Armenia Earthquake Reconnaissance Report. Earthquake Spectra. Special Supplement: 23-42.

Bouchon, M. (1995) Site Response: Physics and Modelling. Proc. 5th Intl. Conf. Seismic Zonation, part III: 1869-1877.

Bouchon, M. (1996) The Discrete Wavenumber Formulation of Boundary Integral Equations and Boundary Element Methods: A Review of Applications to the Simulation of Seismic Wave Propagation in Complex Geological Structures. Pure and Applied Geophysics. 148(1/2): 3-20.

Bouchon, M. and Aki, K. (1977) Discrete Wave-number Representation of Seismic-Source Wave Fields. Bull. Seism. Soc. Am. 67(2): 259-277.

Byrne, PM.; Finn, WDL.; Ventura, CE. (1996) The Hyogo-ken Nambu (Kobe) Earthquake of 17 January 1995: Seismological Aspects and Ground Motions. Can. J. Civ. Eng. 23(3):771-777.

Caltech (1971) Strong Motion Earthquake Accelerograms: Digitized and Plotted Data. Volume II: Corrected Accelerograms and Integrated Ground Velocity and Displacement Curves. Part A. EERL 71-50. California Institute of Technology Earthquake Engineering Laboratory, Pasadena, California.

Caltech (1972) Analysis of Stong Motion Earthquake Accelerograms. Volume III: Response Spectra. Part A. EERL 72-80. California Institute of Technology Earthquake Engineering Laboratory, Pasadena, California.

Chavez-Perez, S.; Ramos-Martinez, J.; Sanchez-Sesma, F.J. (1989) Seismic Response of Three-Dimensional Alluvial Basins of Axisymmetric Shape. In: Engineering Seismology and Site Response: Proceedings of the 4th Intl. Conf. on Soil Dyn. and Earthq. Eng, Mexico City, Mexico, October 1989. Editors: A.S. Cakmak and I. Herrera.

Constantino, CJ. Wachowski, A.; Barnwell, UL. (1967) Finite Element Solution for Wave Propagation in Layered Media Caused by Nuclear Detonation. Proc. Intl. Symp. On Wave Propagation and Dynamic Properties of Earth Materials, Mexico. pp 59-70.

Cotton, CA. (1912) Recent and Sub-Recent Movements of Uplift and Subsidence near Wellington, New Zealand. Scottish Geographical Magazine. 28: 306-312.

Cotton, CA. (1960) Hutt Valley Fault Scarps. NZ. J. Geol. Geophys. 3:218-221.

Cowan, M. and Hatherton, T. (1968) Gravity Surveys in Wellington and Hutt Valley. N.Z. J. Geol. Geophys. 11(1): 1-15.

Cremonini, MG.; Christiano, P.; Beilak, J. (1988) Implementation of Effective Seismic Input for Soil-Structure Interaction Systems. Earthquake Engr. Struct. Dyn. 16: 615-625.

Dellow, GD.; Read, SAL.; Begg, JG.; Van Dissen, RJ.; Perrin, ND. (1992) Distribution of Geological Materials in Lower Hutt and Porirua, New Zealand: A Component of a Ground Shaking Hazard Assessment. Bull. N.Z. Natl. Soc. Earthquake Eng. 25(4):332-344.

DOSLI (1996) Topomap Wellington: Infomap 260 R27, R28 & Pt. Q27. 3rd Ed. Department of Survey and Land Information, Wellington, N.Z.

Douglas, A. (1970) Finite Elements for Geological Modelling. Nature. 226: 630-631.

Drake, LA. (1972a) Love and Rayleigh Waves in Non-horizontally Layered Media. Bull. Seism. Soc. Am. 62:1241-1258.

Drake, LA. (1972b) Rayleigh Waves at a Continental Boundary by the Finite Element Method. Bull. Seism. Soc. Am. 62: 1259-1268.

Dravinski and Mossessian (1987) Scattering of Plane Harmonic P, SV and Rayleigh Waves by Dipping Layers of Arbitrary Shape. Bull. Seism. Soc. Am. 77: 212-235.

Duggan, E.B. (1997) Shallow Siesmic Structure of Parkway Basin, Wainuiomata, New Zealand. Unpublished BSc(Hons) Thesis lodged in Victoria University Library, Wellington, N.Z.

Espinosa, AF.; Husid, R.; Algermissen, ST. De las Casas, J. (1977) The Lima Earthquake of October 3, 1974: Intensity Distribution. Bull. Seism. Soc. Am. 67: 1429-1439.

Fah, D. (1996) Hybrid Methods for Simulating Site Effects. Proc. 11th World Conf. Earthquake Eng. Paper no. 2039.

Field, EH. (1996) Spectral Amplification in a Sediment-Filled Valley Exhibiting Clear Basin-Edge-Induced Waves. Bull. Seism. Soc. Am. 86(4): 991-1005.

Finn, WDL.; Byrne, PM.; Evans, S.; Law, T. (1996) Some Geotechnical Aspects of the Hyogo-ken Nambu (Kobe) Earthquake of January 17, 1995. Can. J. Civ. Eng. 23(3):778-796.

Frankel, A. (1993a) Effects of Three-Dimensional Bedrock Topography on Earthquake Motions in Sedimantary Basins. In: Earthquake Induced Ground Failure Hazards. National Academy Press, Washigton, D.C. pp1-8.

Frankel, A. (1993b) Three-Dimensional Simulation of Ground Motion in the San-Bernandino Valley, California, for Hypothetical Earthquakes on the San Andreas Fault. Bull. Seism. Soc. Am. 83(4): 1020-1041.

Frankel, A. and Vidale, J. (1992) A Three Dimensional Simulation of Seismic Waves in the Santa Clara Valley, California from a Loma Prieta Aftershock. Bull. Seism. Soc. Am. 82(5): 2045-2074.

Grant-Taylor, TL. (1959) Geology of the Hutt Valley. Proceedings of the N.Z. Ecological Society. 6:31-35.

Grant-Taylor, TL. (1967) Fault Movement and Deformation on the Wellington Fault in the Wellington Region. NZ. Geol. Survey Rep. 27, 14p.

Graves, RW. (1993) Modelling Three-Dimensional Site-Response Effects in the Marina District, San Francisco, California. Bull. Seism. Soc. Am. 83(5): 2045-2074.

Graves, RW. (1995) Preliminary Analysis of Long Period Basin Response in the Los Angeles Region from the 1994 Northridge Earthquake. Geophys. Res. Lett. 22(2): 101-104.

Graves, R.W.; Pitarka, A.; Somerville, P.G. (1998) Ground Motion Amplification in the Santa Monica Area: Effects of Shallow Basin-Edge Structure. Bull. Seism. Soc. Am. 88(5): 1224-1242.

Gupta, A. K. (1990) Response Spectrum Method: In Seismic Analysis and Design of Structures. Blackwell Scientific, Boston. 170p.

Haskell, NA. (1960) Crustal Reflection of Plane SH Waves. J. Geophs. Res. 65 (12): 4147-4150.

Helmberger, DV. and Vidale, JE. (1988) Modelling Strong Ground Motions Produced by Earthquakes with Two-Dimensional Numerical Codes. Bull. Seism. Soc. Am. 78: 109-121.

Hisada, Y.; Bao, H.; Bielak, J.; Ghattas, O.; O'Hallaron, D.R. (1998) Simulations of Long-Period Ground Motions during the 1995 Hyogoken-Nanbu (Kobe) Earthquake using 3D Finite Element Method. Proc. 2nd Intl. Symposium on the Effect of Surface Geology on Seismic Ground Motion, Yokohama, Japan, Dec. 1-3, 1998.

Hisada, Y. and Yamamoto, S. (1996) One-, Two- and Three-Dimensional Site Effects in Sediment-Filled Basins. Proc. 11th World Conf. Earthquake Eng, Acupulco, Mexico. Paper no. 2040

Hisada, Y.; Aki, K.; Teng, TI. (1993) Three-Dimensional Simulations of Surface Wave Propagation in the Kanto Sedimentary Basin, Japan. Part 2: Application of the Surface Wave BEM. Bull. Seism. Soc. Am. 83: 1700-1720.

Ingham, C.E. (1971) Elastic Properties of Rock: Wellington Urban Motorway Tunnel. Department of Scientific and Industrial Research Geophysics Division Report No. 71. N.Z.

Ishibashi, I. And Zhang, X. (1993) Unified Dynamic Shear Moduli and Damping Ratios of Sand and Clay. Soils and Foundations 33 (1): 182-191.

Jackson, PS. (1971) The Focussing of Earthquakes. Bull. Seism. Soc. Am. 61: 685-695.

Kato, K.; Aki, K.; Teng, TL. (1993) Three-Dimensional Simulations of Surface Wave Propagation in the Kanto Sedimentary Basin, Japan. Part 1: Application of the Surface Wave Gaussian Beam Method. Bull. Seism. Soc. Am. 83: 1676-1699.

Kawase, H. (1988) Time-Domain Response of a Semi-Circular Canyon for Incident SV, P and Rayleigh Waves Calculated by the Discrete Wavenumber Boundary Element Method. Bull. Seism. Soc. Am. 78: 1415-1437.

Kawase, H. (1996a) The cause of the Damage Belt in Kobe: "The Basin-Edge Effect", Constructive Interference of the Direct S-Wave with the Basin Induced Diffracted/Rayleigh Waves. Seismol. Research Lett. 67(5):25-34.

Kawase, H. (1996b) Site Effects Observed During the Hyogo-Ken Nambu Earthquake of 1995 and Strong Motion Simulation Including the Basin Edge Effect. Proc. 11th World Conf. Earthquake Eng. Paper no. 2031.

Kawase, H. and Aki, K. (1989) A Study on the Response of Soft Basin for Incident S, P and Rayleigh Waves with Special Reference to the Long Duration Observed in Mexico City. Bull. Seism. Soc. Am. 79(5): 1361-1382.

Kawase, H. and Aki, K. (1990) Topography Effect at the Critical SV-Wave Incidence: Possible Explanation of Damage Pattern by the Whitter Narrows, California Earthquake of 1 October 1987. Bull. Seism. Soc. Am. 80: 1-22.

Kazuyoshi, K. (1995) Practical Estimates of Site Response: State-of-Art-Report. Proc. 5th Intl. Conf. Seismic Zonation, part III: 1878-1907.

King, JL. And Tucker, BE. (1984) Observed Variations of Earthquake Motion Across a Sediment-Filled Valley. Bull. Seism. Soc. Am. 74(1): 137-151.

Kosloff, R. and Kosloff, D. (1986) Absorbing Boundaries for Wave Propagation Problems. J. Comp. Phys. 1(63): 363-376.

Kubo, K. and Isoyama, R. (1980) Damage to Buried Utility Pipes in the 1978 Miyagiken-Oki Earthquake. Proc 7th World Conf. Earthquake Eng., Istanbul, Turkey, vol 8, pp 225-232.

Kuhlemeyer, P.L. and Lysmer, J. (1973) Finite Element Method Accuracy for Wave Propagation Problems. J. Soil Mech. And Foundations Division, ASCE vol. 199 (SM5): 421-427.

Larkin, T. and Marsh, J. (1991) 2-D Non-Linear Site Response Analysis. Proc. Pacf. Conf. Earthquake Eng. 3:217-227. or Bull. N.Z. Natl. Soc. Earthquake Eng. 25(3):222-229.

Lensen, G.J. (1958) The Wellington Fault from Cook Straight to Manawatu Gorge. NZ. J. Geol. Geophys. 1:178-196.

Lermo, J. and Charvez-Garcia, EJ. (1994) Are Micro-tremors Useful in Site Response Evaluation. Bull. Seism. Soc. Am. 84(5): 1350-1364.

Lewis, K.B. (1989) A Reversal of Throw and Change of Trend on the Wellington Fault in Wellington Harbour. NZ. J. Geol. Geophys. 32: 293-298.

Ling, H. and Rial, J.A. (1994) Asymptotic Analysis of SH-wave Modes in Geologic Resonators (Sedimentary Basins) of Non-Separable Geometry. Wave Motions 19: 245-270.

Loo, HY. and Jin, XS. (1984) Finite-Element Analysis for Ground Motion of 1976 Tangshan Earthquake. Proc. 8th World Conf. Earthquake Eng., vol II: 343-400.

Love, AEH. (1892) A Treatise on the Mathematical Theory of Elasticity. Cambridge University Press. (reprinted 1944 by Dover Publications, New York).

Love, AEH. (1911) Some Problems of Geodynamics. Cambridge University Press.

Luokakis, KE. and Bielak, J. (1995) Seismic Response of 2D-Valleys: Local Sit Effects. Proc. 3rd Int. Conf. Recent Adv. in Geotechnical Earthquake Eng. Soil Dyn. vol II: 595-599.

Lysmer, J. and Drake, LA. (1972a) A Finite Element Method for Seismology. In: Methods in Computational Physics. 11:181-215. Ed. BA. Bolt, Academic Press, New York.

Lysmer, J. and Drake, LA. (1972b) Propagation of Love Waves Across Non-Horizontally Layered Structures. Bull. Seisem. Soc. Am. 61: 1233-1251.

Lysmer, J. and Kuhlemeyer, RL. (1969) Finite Dynamic Model for Infinite Media. Journal of the Engineering Mechanics Division, ASCE. 95 (EM4): 859-877.

Lysmer, J. and Waas, G. (1972) Shear Wave in Plane Infinite Structure. Journal of the Engineering Mechanics Division, ASCE. 98 (EM1): 85-105.

Lysmer, J.; Udaha, T.; Tsai, C.F.; Seed, H.B. (1975) FLUSH: A Computer Program for Approximate 3-D Anaylsis of Soil Structure Systems. Report EERC 74-4, Earthquake Engineering Research Center, University of California, Berkley, 83p.

Marsh, E.J. (1992) Two Dimensional Nonlinear Seismic Ground Response Studies. Report No. 536, School of Engineering, University of Auckland, N.Z.

Mathworks (1997) MATLAB Version 5.1: The Language of Technical Computing. The Mathworks Inc, Natick, MA.

McKay, A. (1892) On the geology of Marlborough and Southeast Nelson. Part 2. NZGS Reports of Geological Explorations During 1890-91 (21): 1-28.

Millar, P.J. (1991) Museum of New Zealand Te Papa Tongarewai: Geotechnical Investigations Draft Report. Report to the NZ Museum Project. Tonkin and Taylor Ltd, Wellington, New Zealand.

Moczo, P. and Bard, PY. (1993) Wave-Diffraction, Amplification and Differential Motion Near Strong Lateral Discontinuities. Bull. Seism. Soc. Am. 83(1): 85-106.

Nigam, N.C. and Jenningss, P.C. (1969) Calculation of Response Spectra from Strong-Motion Earthquake Records. Bull. Seism. Soc. Am. 59 (2): 909-922.

Ohtsuki, A. and Harumi, K. (1983) Effect of Topography and Subsurface Inhomogeneities on Seismic SV Waves. Earthquake Eng. Struc. Dyn. 11: 441-462.

Olsen, KB. And Archuleta, RJ. (1996) Three-Dimensional Simulation of Earthquakes on the Los Angeles Fault System. Bull. Seism. Soc. Am. 86: 575-596.

Papageorgiou, A. (1996) Two- and Three-Dimensional Effects on Ground Motion. NCEER Bulletin 10 (1): 7-11.

Park, R.; Billings, IJ.; Clifton, GC.; Cousins, J.; Filiatrault, A.; Jennings, DN.; Jones, LCP.; Perrin, ND.; Rooney, SL.; Sinclair, J.; Spurr, DD.; Tanaka, H.; Walker, G. (1995) The Hyogo-ken Nambu Earthquake (The Great Hanshin Earthquake of 17 January 1995): Report of the NZNSEE Reconnaissance Team. Bull. NZ. Natl. Soc. Earthquake Eng. 28 (1): 1-9.

Perrin, N.D. and Campbell, H.J. (1992) Compliation of Geological Data, Wellington Area. DSIR Geology and Geophysics Contract Report No. 1992/24. Part 3 of the 1991/92 study for the Wellington Regional Council.

Pitarka, A. and Irikura, K. (1996) Basin Structure Effects on Long-Period Strong Motions in the San Fernando valley and the Los Angeles Basin. Bull. Seism. Soc. Am. 86 (1B): S126-S137.

Pitarka, A.; Irikura, K.; Iwata, T.; Segiguchi, H. (1998) Three-Dimensional Simulation of the Near-Fault Ground Motion for the 1995 Hyogo-ken Nanbu (Kobe), Japan, Earthquake. Bull. Seism. Soc. Am. 88: 428-440.

Pitarka, A.; Suetsugu, D.; Takenaka, H. (1996) Elastic Finite Difference Modelling of Strong Motion in Ashigara Valley for the 1990 Odawara, Japan Earthquake. Bull. Seism. Soc. Am. 86 (4): 981-990.

Pitarka, A.; Takenaka, H.; Suetsugu, D. (1994) Modelling Strong Motion in Ashigara Valley for the 1990 Odawara, Japan Earthquake. Bull. Seism. Soc. Am. 84 (5): 1327-1335.

Poceski, A. (1969) The Ground Effect of the Scopie July 26 1963 Earthquake. Bull. Seism. Soc. Am. 59(1): 1-22.

Prescott, WH. (1982) Circumstances Surrounding the Preparation and Suppression of a Report on the 1868 California Earthquake. Bull. Seism. Soc. Am. 72(6): 2389-2393.

Rassem, M.; Ghaobarah, A.; Heinebrecht, AC. (1997) Engineering Perspective for the Seismic Site Response of Alluvial Valleys. Earthq. Eng. and Struct. Dyn. 26: 477-493.

Rial, J.A. (1989a) Geologic Resonators of Arbitrary Geometry: Chaotic Behavior of Trapped Seismic Waves. In: Engineering Seismology and Site Response: Proceedings of the 4th Intl. Conf. on Soil Dyn. and Earthq. Eng, Mexico City, Mexico, October 1989. Editors: A.S. Cakmak and I. Herrera.

Rial, J.A. (1989b) Seismic Wave Resonances in 3-D Sedimentary Basins. Geophys. J. Int. 99: 81-90.

Rial, JA. and Ling, H. (1992) Theoretical Estimation of the Eigenfrequencies of 2-D Resonant Sedimentary Basins: Numerical Computations and Analytical Approximations to the Elastic Problem. Bull. Seism. Soc. Am. 82 (6): 2350-2367.

Rial, JA.; Saltzman, NG.; Ling, H. (1992) Earthquake Induced Resonance in Sedimentary Basins. American Scientist 80: 566-578.

Ricker, N. (1940) The Form and Nature of seismic Wavelets and the Structure of Seismograms. Geophysics 5: 348-366.

Sanchez-Sesma, F. (1987) Site Effects on Strong Ground Motion. Soil Dyn. Earthquake Eng. 6: 124-132.

Sanchez-Sesma, F. and Luzon, F. (1995) Seismic Response of Three-Dimensional Alluvial Valleys for Incident P, S, and Rayleigh Waves. Bull. Seism. Soc. Am. 85 (1): 269-284.

Sanchez-Sesma, F.; Chavez-Garcia, F.; Bravo, M. (1988a) Seismic Response of a Class of Alluvial Valleys for incident SH Waves. Bull. Seism. Soc. Am. 78: 83-95.

Sanchez-Sesma, F.; Chavez-Garcia, F.; Suarez, MA.; Bravo, M.; Perez-Rocha, LE. (1988b) On the Seismic Response of the Valley of Mexico. Earthquake Spectra. 4: 569-589.

Schrivner, C.W. and Helmberger, D.V. (1994) Seismic Waveform Modelling in the Los Angeles Basin. Bull. Seism. Soc. Am. 84(5): 1310-1326.

Seed, H.B.; Wong, R.T.; Idriss, I.M. Tokimatsu, K. (1986) Moduli and Damping Factors for Dynamic Analyses of Cohesionless Soils. ASCE Journal of Geotechnical Engineering 112 (11): 1016-1032.

Seki, T. and Nishikawa, T. (1988) Absorbing Boundaries for Wave Propagation Problems (Using Kosloff's Method in Absorbing Region. Proc. 10th World Conf. Earthquake Eng. vol II:629-634.

Shewchuck, J.R. (1996) Triangle: Engineering a 2D Quality Mesh Generator and Delaunay Triangulator. First Workshop on Applied Computational Geometry (Philidelphia, PA.), pp124-133, ACM, May 1996.

Shibuya, J. (1992) Amplitude of Surface Waves in Ground Motion on Alluvial Basins. Proc. 10th World Conf. Earthquake Eng. vol II: 629-634.

Smith, WD. (1974) A Non-Reflecting Plane Boundary for Wave Propagation Problems. J. Comp. Phys. 15: 492-503.

Smith, WD. (1975) The Application of Finite Element Analysis to Body Wave Propagation Problems. Geophys. J. Astr. Soc. 42:747-768.

Standards New Zealand (1992) NZS 4203: 1992 Loadings Standard: Code of Practice for General Structural Design and Design Loadings for Buildings. Sec 4.6: Seismic Design Actions. Vol 1: Code of Practice pp 40-47. Vol 2: Commentary pp 32-37.

Stephenson, W.R. (1974) Earthquake Induced Resonant Motion of Alluvium. Bull. N.Z. Natl. Soc. Earthquake Eng. 7 (3): 144-146.

Stephenson, W.R. (1975) Cellular Normal Modes of Alluvium Response. Bull. N.Z. Natl. Soc. Earthquake Eng. 8 (4): 245-254.

Stephenson, W.R. (1989a) Normal Modes of a "Cylindrical Valley of Alluvium. Bull. N.Z. Natl. Soc. Earthquake Eng. 22 (2): 76-80.

Stephenson, W.R. (1989b) Observation of a Directed Resonance in Soil Driven by Transverse Rock Motion. Bull. N.Z. Natl. Soc. Earthquake Eng. 22 (2): 81-89.

Stephenson, W.R. and Barker, P.R. (1992) Evaluation of the Sediment Properties in the Lower Hutt and Porirua Areas by Means of Cone and Seismic Cone Penetration Tests. Bull. N.Z. Natl. Soc. Earthquake Eng. 25(4):265-285.

Stevens, GR. (1956) Stratigraphy of the Hutt Valley, New Zealand. N.Z. J. Sci. Tech. 38B (3):201-235.

Stevens, GR. (1958) The Wellington Fault. Trans. Roy. Soc. NZ. 85.

Stevens, GR. (1990) Rugged Landscape: The Geology of Central New Zealand. DSIR, Wellington, New Zealand.

Stevens, GR. (1991) On Shaky Ground. A Geological Guide to the Wellington Metropolitan Region. DSIR, Lower Hutt, New Zealand.

Stritharan, S.; McVerry, GH. (1992) Microzone Effects in the Hutt Valley in Records from a Strong-Motion Acceleograph Array. Bull. N.Z. Natl. Soc. Earthquake Eng. 25(4):246-264.

Taber, J.J. (1995) Limits to Microzonation due to Real Variability in Site Response. Proc 5th Intl. Conf. Seismic Zonation, Nice, France. pp 1157-1164.

Taber, J.J. and Richardson, W.P. (1992) Frequency Dependant Amplification of Weak Ground Motions in Wellington City and the Kapiti Coast. Report Prepared for the Wellington Regional Council.

Taber, JJ.; Smith, EGC. (1992) Frequency Dependant Amplification of Weak Ground Motions in Porirua and Lower Hutt, New Zealand. Bull. N.Z. Natl. Soc. Earthquake Eng. 25(4):303-331.

Taber, JJ.; Stritharan, S.; McVerry, GH.; Ansell, JH. (1993) Site Effects from Seismic Shaking: A comparison of Strong and Weak Ground-Motion in Wellington City and the Hutt Valley. A report to Earthquake and War Damage Commission.

Toki, K.; Irikura, K.; Kagawa, T. (1995) Strong Motion Records in the Source Area of the Hyogoken-Nambu Earthquake, January 17, 1995, Japan. J. Nat. Disaster Sci. 16 (2): 23-30.

Toshinawa, T. (1998) Kobe University (KBU) Digital Records from the 1995 Hyogo-ken Nambu Earthquake. Obtained via ftp, Takumi Toshinawa, Tokyo Institute of Technology, Japan.

Toshinawa, T. and Ohmachi, T. (1992) Love Wave Propagation in a Three-Dimensional Sedimentary Basin. Bull. Seism. Soc. Am. 82: 1661-1667.

Touhei, T. and Yoshida, N. (1988) A Coupled Boundary and FEM for the Time Marching Analysis. Proc. 9th World Conf. Earthquake Eng. II: 623-628.

Trifunac, M.D. (1970) Low Frequency Digitization Errors and a New Method for Zero Baseline Correction of Strong Motion Accelerograms. EERL 70-07. California Institute of Technology Earthquake Engineering Laboratory, Pasadena, California.

Trifunac, M.D. and Lee, V. (1973) Routine Computer Processing of Strong-Motion Accelerograms. EERL 73-03. California Institute of Technology Earthquake Engineering Laboratory, Pasadena, California.

Trifunac, MD. (1971) Surface Motion of a Semi-Cylindrical Alluvial Valley for Incident Plane SH Waves. Bull. Seism. Soc. Am. 61: 1755-1770.

Tucker, BE. and King, JL. (1984) Dependance of Sediment-Filled Valley Response in Input Amplitude and Valley Properties. Bull. Seism. Soc. Am. 74(1): 153-165.

Van Dissen, R.J. and Berryman, K.R. (1996) Surface rupture earthquakes over the last ~1000 years in the Wellington region, New Zealand, and implications for ground shaking hazard. J. Geophys. Res. 101(B3): 5999-6019.

Van Dissen, R.J. and Berryman, K.R. (1991) Timing, Size and Reccurence Interval of Prehistoric Earthquakes in the Wellington Region, New Zealand. In: Proceedings, Pacific Conference on Earthquake Engineering, Auckland, New Zealand 3:239-249.

Van Dissen, R.J. and Berryman, K.R. (1990) Seismic Hazard Assessment of the Wellington-Hutt Valley Segment of the Wellington Fault. Regional Natural Disaster Reduction Plan - Seismic Hazard 1989 Study, Part 5. Department of Scientific and Industrial Research

Van Dissen, RJ.; Berryman, KR.; Pettinga, JR.; Hill, N. (1992a) Paleoseismicity of the

Wellington-Hutt Valley Segment of the Wellington Fault, North Island, New Zealand. NZ. J. Geol. Geophys. 35:165-176.

Van Dissen, RJ.; Taber, JJ.; Stephenson, WR.; Stritharan, S.; Read, SAL.; McVerry, GH.; Dellow, GD.; Barker, PR. (1992b) Earthquake Ground Shaking Hazard Assessment for the Lower Hutt and Porirua Areas, New Zealand. Bull. N.Z. Natl. Soc. Earthquake Eng. 25(4):286-302.

Vidale, JE. And Helmberger, DV. (1988) Elastic Finite Difference Modelling of the 1971 San Fernando, California Earthquake. Bull. Seism. Soc. Am. 78(1): 122-141.

Wang, Z. (1996) Seismic Response of Alluvial Valleys. Proc. 11th World Conf. Earthquake Eng. Paper no. 730.

Weischet, W (1963) The Distribution of the Damage Caused by the Earthquake in Valdivia in Relation to the Form of the Terrane. Bull. Seism. Soc. Am. 53(5): 1259-1262.

Wirgin, A. (1995a) On the Nature of Ground Motion above and Beyond a Soft Basin Submitted to Seismic Waves. Proc. 5th Intl. Conf. Seismic Zonation, Nice, France. pp 1213-1220.

Wirgin, A. (1995b) Resonant Response of a Soft Semi-Circular Cylindrical Basin. Bull. Seism. Soc. Am. 85 (1): 285-299.

Wong, TL. And Trifunac, MD. (1974) Surface Motion of a Semi-Elliptical Alluvial Valley for Incident Plane SH Waves. Bull. Seism. Soc. Am. 64: 1389-1408.

Yamanaka, H.; Seo, K.; Samano, T. (1989) Effects of Sedimentary Layers on Surface-Wave Propagation. Bull. Seism. Soc. Am. 79(3): 631-644.

Yuan, Y.; Yang, B.; Huang, S. (1992) Damage Distribution and Estimation of Ground Motion in Shidian (China) Basin. Proc. Int. Symp. Effects of Surface Geology on Seismic Motion, 25-27 March, Odawara, Japan. vol 1, pp 281-286

Zahradnik, J. and Hron, F. (1987) Seiesmic Ground Motion of Sedimentary Valleys: Example La Molina, Lima, Peru. J. Geophys. 62: 31-37.

Zhang, B. and Papageorgiou, AS. (1995) Seismic Response of a Linear, 2-D Model of the Marina District. Proc. 3rd Int. Conf. Recent Adv. in Geotechnical Earthquake Eng. Soil Dyn. vol II: 567-570.

Zhou, T. and Dravinski, M. (1994) Resonance Prediction of Deep Sediment Valleys Through an Eigenvalue Method. Geophs. J. Int. 117: 749-762.